ELECTRICALLY INJECTED PHOTONIC-CRYSTAL NANOCAVITIES

Karl P. Welna

**A Thesis Submitted for the Degree of PhD
at the
University of St. Andrews**

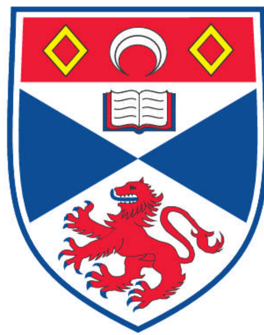

2011

**Full metadata for this item is available in
Research@StAndrews:FullText
at:
http://research-repository.st-andrews.ac.uk/**

**Please use this identifier to cite or link to this item:
http://hdl.handle.net/10023/2528**

This item is protected by original copyright

**This item is licensed under a
Creative Commons License**

Electrically Injected Photonic-Crystal Nanocavities

Karl P. Welna

Thesis submitted for the degree of Doctor of Philosophy

September 2011

University
of
St Andrews

Declarations

I, Karl P. Welna, hereby certify that this thesis, which is approximately 50000 words in length, has been written by me, that it is the record of work carried out by me and that it has not been submitted in any previous application for a higher degree.

I was admitted as a research student in September 2007 and as a candidate for the degree of Doctor of Philosophy in September 2007; the higher study for which this is a record was carried out in the University of St Andrews between 2007 and 2011.

(Karl P. Welna) September 2011

I hereby certify that the candidate has fulfilled the conditions of the Resolution and Regulations appropriate for the degree of Doctor of Philosophy in the University of St Andrews and that the candidate is qualified to submit this thesis in application for that degree.

(Thomas F. Krauss) September 2011

In submitting this thesis to the University of St Andrews I understand that I am giving permission for it to be made available for use in accordance with the regulations of the University Library for the time being in force, subject to any copyright vested in the work not being affected thereby. I also understand that the

title and the abstract will be published, and that a copy of the work may be made and supplied to any bona fide library or research worker, that my thesis will be electronically accessible for personal or research use unless exempt by award of an embargo as requested below, and that the library has the right to migrate my thesis into new electronic forms as required to ensure continued access to the thesis. I have obtained any third-party copyright permissions that may be required in order to allow such access and migration, or have requested the appropriate embargo below.

The following is an agreed request by candidate and supervisor regarding the electronic publication of this thesis:

Access to printed copy and electronic publication of thesis through the University of St Andrews.

(Karl P. Welna) (Thomas F. Krauss) September 2011

Acknowledgements

First of all I would like to thank my supervisor *Professor Thomas Krauss* for the opportunity to work in his research group, for the support of my ideas, the guidance of my work and his open-door policy; my second supervisor *Dr. Graham Turnbull* for discussions related to my subject and my work.

Dr. Andrea Di Falco and *Dr. Christopher Reardon* for discussions, advices on technological processes and experimental set-ups.

Dr. William Whelan-Curtin for sharing his technological expertise and for the constant flow of inspirational ideas.

Also, I would like to thank the members of the *microphotonics research group* for great support and a friendly atmosphere. Special thanks to *Dr. Thomas White* and *Dr. Daryl Beggs* for their help with general photonic-crystal problems and their modelling.

Very special thanks to *Mr. George Robb* and *Mr. Steven Balfour* for their magic hands with the cleanroom facilities and a pleasant working environment.

Dr. Maxime Hugues for advice on wafer properties and the wafer grow.

Mr. Simone L. Portalupi and colleagues for the *University of Pavia* for measurements on Silicon cavities and a very pleasant and inspiring working atmosphere.

Speckled Computing, EPSRC and *LECSIN* for funding of my work.

To my family, my father *Richard*, my mother *Hedwig* and my brother *Peter*.

To all my friends, especially *Dr. Marco Grande* and *Dr. Shu Chen,* for their support and their friendship.

Very special thanks to *Isabella H. Rey*.

Publications arising from this work

- M. Galli, D. Gerace, K. Welna, T. F. Krauss, L. O'Faolain, G. Guizzetti, L. C. Andreani; “Low-power continuous-wave generation of visible harmonics in silicon photonic crystal nanocavities”; Optics Express, Vol. 18, 26613; (2010) (Journal Publication)
- C. Reardon, A. Di Falco, K. Welna, T. F. Krauss; “Integrated polymer microprisms for free space optical beam deflecting”; Optics Express, Vol. 17, 3424; (2009) (Journal Publication)
- K. Welna, L. O’Faolain, S. L. Portalupi, M. Galli, L. C. Andreani and T. F. Krauss; “Dispersion Controlled Cavity: Gentle confinement with larger defect modifications”; UK Semiconductors, Sheffield, July 2010 (Conference Presentation)
- K. Welna, L. O’Faolain, S. L. Portalupi, M. Galli, L. C. Andreani and T. F. Krauss; “Dispersion Controlled Cavity: Gentle confinement with larger defect modifications”; EMRS, Strasbourg, June 2010 (Conference Presentation)
- K. Welna, C. Reardon, A. Di Falco and T. Krauss; “Fabrication of Electrically Pumped Photonic-crystal Laser for Ultra-low Threshold Applications”; SIOE ’09, Cardiff, April 2009 (Conference Presentation)
- K. Welna, L. O’Faolain, S. L. Portalupi, M. Galli, L. C. Andreani and T. F. Krauss; “Dispersion Controlled Cavity: Gentle confinement with larger defect modifications”; PECS IX, Granada, September 2010 (Conference Poster)
- K. Welna, C. Reardon, A. Di Falco and T. Krauss; “Optical Device Integration”; attended 7th Workshop in Speckled Computing, Edinburgh, December 2008
- Journal Publications in preparation:
    - “DA cavity with improved disorder stability”
    - “High Q-factor GaAs cavity on oxidised AlGaAs made with TiO_x hard-mask”

Abstract

Nano-emitters are the new generation of laser devices. A photonic-crystal cavity, which highly confines light in small volumes, in combination with quantum-dots can enhance the efficiency and lower the threshold of this device. The practical realisation of a reliable, electrically pumped photonic-crystal laser at room-temperature is, however, challenging.

In this project, a design for such a laser was established. Its properties are split up into electrical, optical and thermal tasks that are individually investigated via various device simulations. The resulting device performance showed that with our design the quantum-dots can be pumped in order to provide gain and to overcome the loss of the system. Threshold currents can be as low as 10's of μA and Q-factors in the range of 1000's.

Gallium arsenide wafers were grown according to our specifications and their diode behaviour confirmed. Photonic-crystal cavities were fabricated through a newly developed process based on a TiO_x hard-mask. Beside membraned cavities, also cavities on oxidised AlGaAs were fabricated with help to a unique hard-mask removal method. The cavities were measured with a self-made mirco-photoluminescence setup with the highest Q-factor of 4000 for the membrane cavity and a remarkable 2200 for the oxide cavity.

The fabrication steps, regarding the electrically pumped photonic-crystal laser, were developed and it was shown that this device can be fabricated.

During this project, a novel type of gentle confinement cavity was developed, based on the adaption of the dispersion curve (DA cavity) of a photonic-crystal waveguide. Q-factors of as high as 600.000 were measured for these cavities made in Silicon

Contents

Declarations i

Acknowledgements iii

Publications arsing from this work iv

Abstract v

1 INTRODUCTION AND MOTIVATION **1**

1.1 PHOTONIC-CRYSTAL LASERS – STATE OF THE ART 2

2 BACKGROUND INFORMATION ON ELECTRICALLY PUMPED EPCL **5**

2.1 INTRODUCTION 5

2.2 THEORY OF SEMICONDUCTORS, QUANTUM DOTS AND PHOTONIC-CRYSTALS 5

2.2.1 Carrier Injection: Semiconductor PIN Diode 7

2.2.2 Quantum Dots as Gain Material 8

2.2.3 Photonic-Crystal Cavity 13

2.3 REVIEW OF SELECTED DEVICES 20

2.3.1 Cavity-Enhanced Photonic-Crystal Light-Emitting Diode at 1300 nm 20

2.3.2 Ultralow-Threshold Electrically Pumped Quantum-Dot Photonic-Crystal Nanocavity Laser 23

3 DESIGN AND SIMULATIONS ON EPCL **27**

3.1 INTRODUCTION 27

3.2 ELECTRICAL PROPERTIES 28

3.2.1 Definition of the Electrical Model 28

3.2.2 Device Optimisation through FEM Model 36

3.3 OPTICAL PROPERTIES 43

3.3.1 Intrinsic Q-factors for different Types of Cavities 43

3.3.2 Loss and Gain Evaluation 51

3.4 THERMAL PROPERTIES 58

3.5 WAFER PARAMETERS 63

4 DISPERSION ADAPTED CAVITY **65**

4.1 INTRODUCTION 65

4.2 TYPES OF CAVITY MODIFICATIONS 65

4.3 METHODOLOGY OF CONFINEMENT 69

4.3.1 Numerical Part: Dispersion Curves 70
4.3.2 Analytical Part: Master-Equation 73
4.4 PARAMETER OPTIMISATION SCAN 75
4.5 EXPERIMENTAL Q-FACTORS OF DA CAVITIES IN SILICON 80
4.6 DA CAVITY IN GAAS 84
5 TESTING OF MATERIAL PROPERTIES 89
5.1 INTRODUCTION 89
5.2 ELECTRICAL PROPERTIES 89
5.2.1 Vn1315: Stripe-laser Electrical Device 89
5.2.2 Vn1807: ePCL Electrical Device 95
5.3 OPTICAL PROPERTIES 97
5.3.1 Fabrication of Stripe-laser Devices 98
5.3.2 Characterisation of Stripe-laser Devices 101
5.3.3 Electrical Pumping of Stripe-laser devices 107
6 PHOTONIC-CRYSTAL CAVITY AND FABRICATION OF EPCL 111
6.1 INTRODUCTION 111
6.2 PHOTONIC-CRYSTAL CAVITIES 111
6.2.1 Fabrication of Photonic-Crystal Cavities 111
6.2.2 Optical Characterisation of PhC Cavities 129
6.3 FABRICATION OF EPCL 142
7 CHAPTER 7 147
7.1 FUTURE WORK 150

APPENDIX A: FABRICATION DETAILS 153
APPENDIX B: FURTHER ANALYSIS ON THRESHOLD FORMULATION 159
BIBLIOGRAPHY 161

Chapter 1

Introduction and Motivation

Technology development follows a clear trend towards miniaturisation. As packing density increases, more functionality can be placed into the same footprint, leading to an overall performance improvement. The performance of a single device also improves simply due to the reduction of its size, so that electrons in a transistor travel shorter distances or emitters need fewer electrons to fill up energy states. Correspondingly, the operating speed also increases. Another aspect of this miniaturisation comes into play as energy resources become increasingly limited and efficiency attains more significance. Smaller devices consume less energy due to their reduced volume, and less energy results in less waste heat. Using less energy is an important aspect when devices such as nano-emitters are integrated on processors to speed up data exchange, used as small light sources for integrated photonics applications or for free-space optical communication of independent computing units.

The aim of this project is to design and to build an efficient nano-emitter ideally a laser. The device is based on a Photonic-Crystal cavity, as this offers the highest optical confinement in small volume of any type of cavity, and is therefore ideal for efficient lasers with low thresholds. In order to make these devices practical, direct carrier injection via electrical pumping as well as thermal management is needed.

In summary, we aim to design and to build a practical, electrically pumped Photonic-crystal laser that can operate continuous-wave at room-temperature.

1.1 Photonic-Crystal Lasers – State of the Art

Photonic-crystal lasers (PCL) were first demonstrated in Indium Phosphide via optical pumping [Painter99] as shown in Figure 1.1. The fabrication process was still in its earlier years and therefore less developed so that the Q-factor of the device was only 250. Therefore, a high gain material based on quantum-wells was needed to overcome the loss and to achieve lasing. This resulted in a high external threshold pump power of 6.75 mW at 143 K. Since then, the fabrication, the cavity designs and the gain material have rapidly developed but the general concept remained the same. As shown in Figure 1.1, the PhC provide the confinement in lateral direction where the vertical confinement is ruled by total internal reflection at the top- and bottom-surface.

From then on, optically pumped lasing was achieved for various cavity geometries such a circular PhC pattern [Errico07], rectangular PhC pattern [Altug06], [Ryu02] but mostly in hexagonal patterns [OBrien07], [Loncar04]. Q-factors increased due to improved fabrication and cavities design and can be as high as 20.000 [Nozaki07] for a similar system as in Figure 1.1.

In terms of threshold, this not only depends on the cavity but also on the gain material, as it will be shown later, so that with based on quantum-dots the effective threshold power was reduced to 42 nW [Nomura09]. This is an improvement of 5 orders of magnitude to the first PhC laser.

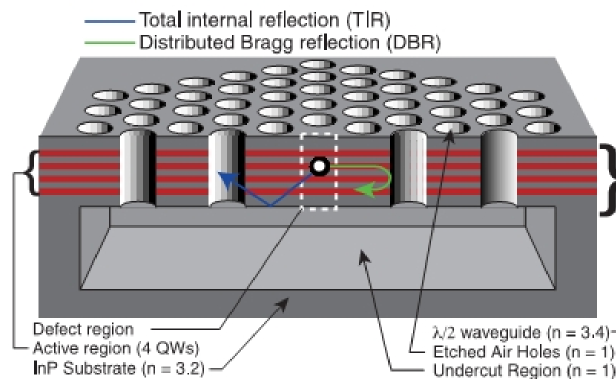

Figure 1.1 Cross-section through optically pumped PhC laser containing quantum wells. The optical confinement is achieved by Bragg-reflection in-plane and total-internal reflection out-of-plane. [Painter99][1]

In these systems, there is still an external optical pump needed so that electrical pumping is desirable. The first electrically pumped PhC laser [Park04] had a design shown in Figure 1.2. This particular design has a conductive post supporting the membrane. Beside the current flow over the post also the heat is better dissipated out of the membrane than conventional free-standing membrane. Despite the thermally conductive post, these devices can only be operated in pulsed mode because of the generated heat. The drawback of this system is a more difficult fabrication process and the need for a special optical mode avoiding the centre of the cavity. The thresholds of similar devices can be as low as 100 μA [Chakravarty07], [Seo07].

In section 2.3 "Review of Selected Devices" we review two electrically pumped devices that help us with the decision masking of our design.

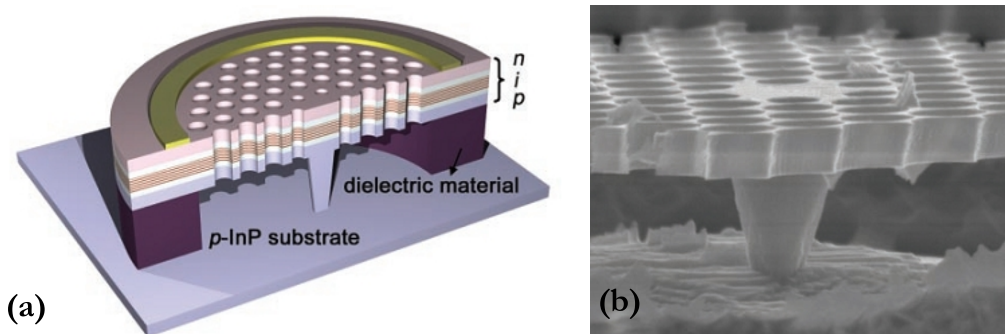

Figure 1.2 Free-standing PhC slab with conductive post below the cavity (a). The current flows from the top gold contact over the PhC pattern, through the cavity and over the post into the substrate. SEM side-image (b) of the structure. [Park04][2]

Chapter 2

Background Information on Electrically Injected PhC Cavity

2.1 Introduction

This chapter builds the foundation for the planned device by presenting theoretical aspects of its general working principle in the first part and a discussion of similar, published devices in the second part.

2.2 Theory of Semiconductors, Quantum Dots and Photonic-Crystals

When designing a LASER (Light Amplification by Stimulated Emission of Radiation), whether in a solid-state or in a semiconductor system, three basic principles must be adhered to: *pumping*, *gain* and *feedback*, as shown in Figure 2.1.

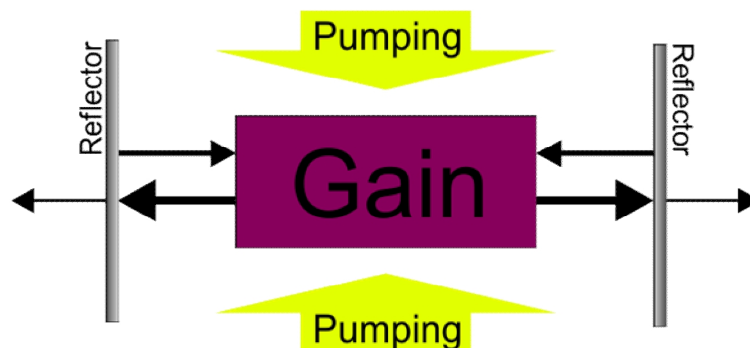

Figure 2.1 Schematic principle of a laser with the gain medium being pumped and the emission is partly back-reflected into the medium triggering stimulated emission (see text).

Pumping refers to a way of exciting the active medium – often by carriers – and leading to spontaneous emission of photons. These photons radiate in all directions, but when the active medium is placed in a resonator photons are back-reflected into the active medium, causing the excited medium to emit identical photons in terms of wavelength, phase and direction. This is called stimulated emission because the back-reflected photons trigger the stimulated emission of additional photons, which is governed by the radiation probabilities first derived by *A. Einstein* [Einstein17]. Here we do not want to go into the details of the so-often described laser process, but we rather focus on the key principles that are relevant for the device operation. Gain and lasing can only occur when the amount of generated photons exceeds the lost photons. In terms of gain and loss coefficients, lasing only occurs when the gain equals the loss of a system, know as the threshold condition:

$$g = \alpha_{loss} \tag{Eq.2.1}$$

where g and α_{loss} are the coefficients for gain and loss in units of [cm^{-1}] according to Beer–Lambert's law for absorption. The losses can be further specified as photon loss out of the cavity α_{cavity} and general absorption α_{abs} resulting in:

$$\alpha_{cavity} + \alpha_{abs} = g \tag{Eq.2.2}$$

In a macroscopic laser system, the photon loss-rate is typically determined by α_{cavity}. Also, in a macroscopic system, the active medium has the same optical mode overlap as the absorption medium, but in a microscopic system, the optical mode will have a different overlap between the active and the absorptive media. Therefore, it is useful to account for the different overlaps by introducing a confinement factor Γ that describes the overlap of the optical mode with the active and lossy media[1]:

$$\alpha_{cavity} + \Gamma_{abs}\alpha_{abs} = \Gamma_g g \tag{Eq.2.3}$$

From this equation, we see that threshold can be reached when the cavity-loss α_{cavity} is low, as well as the material absorption α_{cbs} or the mode overlap Γ_{abs} with the lossy

---

[1] In appendix B, this general case of Eq.2.3 is compared to the formulation for stripe-lasers.

material. On the other hand, threshold can also be reached when the gain g of the material is high, as well as the mode overlap Γ_g with the active material. Eq.2.3 will later be used to evaluate our design in terms of these parameters.

Reaching threshold as described by Eq.2.3 depends on the pumping method, the type of active material and the type of resonator, as described earlier. We now establish a theoretical foundation covering a *semiconductor* for carrier injection, *quantum dots* as the active material within a *photonic-crystal cavity*, and show their basic principles.

2.2.1 Carrier Injection: Semiconductor PIN Diode

The use of semiconductors is an elegant way of building devices for light emission, as the material can be designed to conduct, both *electrons* or their counterparts, the *holes,* whose recombination leads to the emission of photons in a semiconductor. The advantage of a semiconductor is that it can be designed to preferentially conduct either electrons or holes by doping with special impurities. In this way, separate electron- and hole-conducting parts can be created that transport the carriers into the active region, as shown in Figure 2.2.

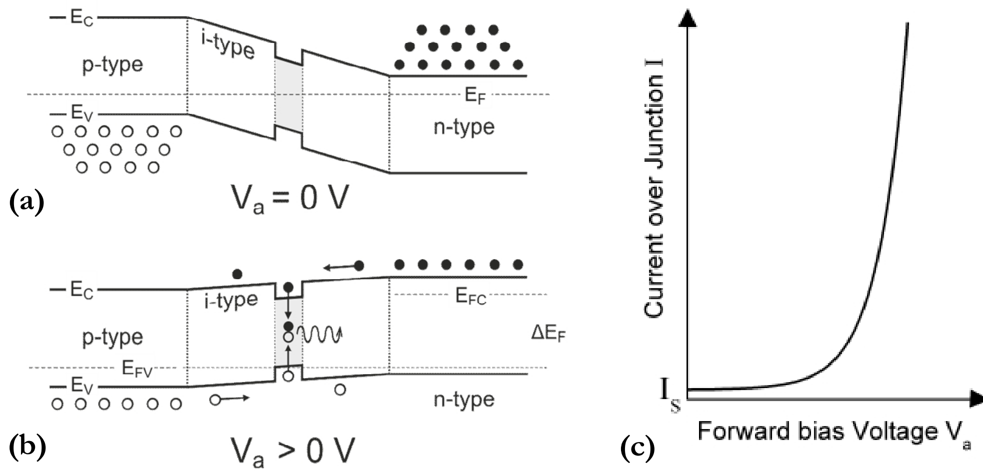

Figure 2.2 Energy diagram of p/i/n structure including am active region (grey) made out of lower energy semiconductor. Carrier flow (electrons: filled circles; holes: open circles) is initiated by an applied voltage V_a that leads to electron-hole recombination in the active region and creates photons. Without biasing, the Fermi-level E_F is constant and splits into individual Fermi-levels E_{FC} for the conduction-band and E_{FV} for the valence-band when biased. A representative current-voltage behaviour of this structure is shown in (c) with the saturation current I_S.

Here, the Fermi-level E_F is close to the conduction band E_C in the n-type material, indicating electron occupation, and vice versa with the holes in the p-type material. When an external voltage is applied – forward biasing – the current flows over the device and increases exponentially according to the *Shockley diode equation*:

$$I_{(V)} = I_S \cdot (\exp(V_a / n \cdot V_T) - 1) \quad \text{(Eq.2.4)}$$

where I_s is the reverse saturation current, V_a the applied voltage, n the ideality factor and V_T the thermal voltage of about $0.025\ V$. The exponential form originates from the exponential carrier distribution at the band-edge and an exponential decay of the carriers when V_a is increased. The ideality factor describes the deviation from the ideal diode and is an indicator for good fabrication, where values close to 1 are desirable.

The p/i/n structure after Figure 2.2 is already an advanced structure because it contains two different types of semiconductors with two different band-gap energies. This so-called double hetero-structure (DH) creates a potential well where the narrow band-gap material (active region, grey region in Figure 2.2) is confined by a wide band-gap material, which helps with the confinement of the carriers and the radiative recombination. In the next section, we discuss the gain material.

2.2.2 Quantum Dots as Gain Material

Gain in semiconductors can be achieved by *population inversion* of the active material, which means that the probability of an electron to occupy the conduction band has to be higher than the probability of an electron to occupy the valence band. In a diode, the population inversion comes naturally when the current over the junction increases [Hall62], [Holonyak87].

More interesting, on the other hand, is the type of material used for gain because not only the chemical structure but also the physical structure has a big influence on its behaviour. *Quantum structures* refer to this kind of physical structure, because by simply increasing their degree of confinement different electronic and optical properties are achieved. Here the confinement refers to bound electron-hole states

know as excitons and confinement can be achieved in different ways, where common methods employ e.g. a higher band-gap material surrounding the structures or even strain.

…tiny lasers need tiny structures …

This phrase is a simple expression of the need for the best quantum structures for nano-lasers that are *Quantum-Dots (QDs)* with a 3-dimensional confinement.

Ideal QDs offer superior properties over other quantum structures and have the ability to create the perfect laser due to the following properties:

- Maximum material gain
- Lowest transparency current density
- Reduced out-diffusion of carriers
- Improved temperature stability

We now comment on these properties starting with the feature that determines the material gain. The maximum material gain g_{max} in a semiconductor at the transition wavelength λ is given by [Ustinov07]:

$$g_{(\lambda)\max} = \frac{e^2\lambda}{2n\varepsilon_0 c^2 m_0^2}\left|M_{T(\lambda)}\right|^2 \rho_{r(\lambda)} \qquad \text{(Eq.2.8)}$$

where, e is the elementary charge, n the refractive index, ε_0 the vacuum permittivity, c the speed of light, m_0 the electron mass, $|M_{T(\lambda)}|^2$ the transition matrix element and $\rho_{r(\lambda)}$ the reduced density-of-states (DOS) for this transition. This equation is derived from *Fermi's Golden Rule* and its magnitude mainly depends on the matrix element and on the DOS. The matrix element describes the strength of interaction of two electron states – initial and final state – acting on the photon field, which can also be described via the lifetime of the transition. The main contributing factor to g_{max} that is altered by moving form a conventional hetero-structure to a quantum-structure is the density of states (DOS). The DOS describes the number of available states per unit energy and space. Calculating

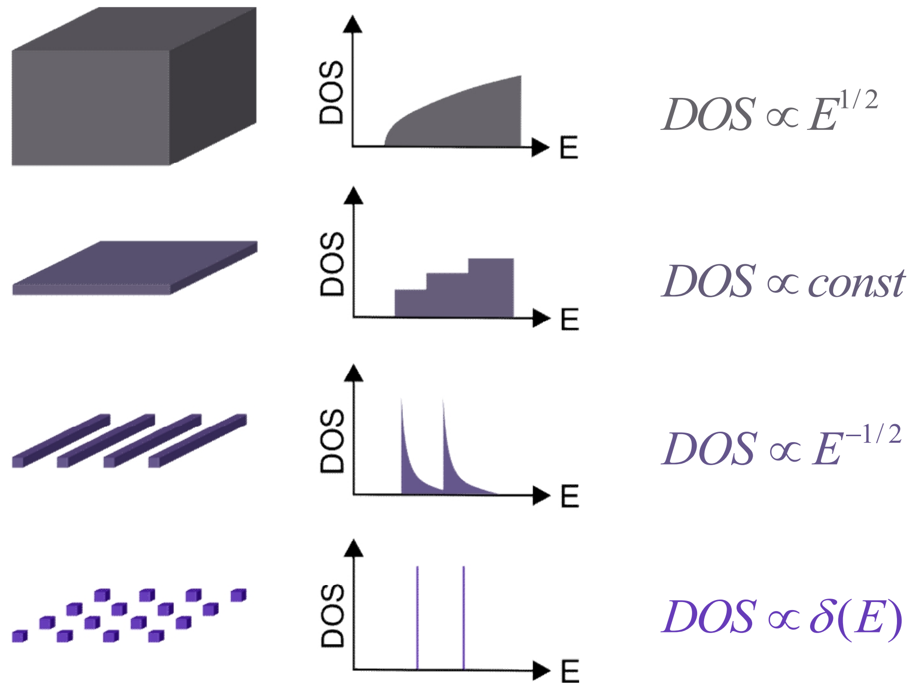

Figure 2.3 Density of states for four structures starting from top: bulk, quantum-well, quantum-wire and quantum-dot. In the case of the bulk material, the DOS follows the square-root of the energy; the quantum-well shows constant plateaus; the DOS of the quantum-wire follows the inverse square-root of the energy and the quantum-dots are distinct peak in the DOS.

the DOS involves accounting for the dispersion-relation of the bands of the crystal structure and, most importantly, for the dimensionality of the electronic system. Four different dimensionalities can be distinguished, with their DOS shown in Figure 2.3. The DOS of a bulk semiconductor follows the square-root of E due to parabolic bands. In this system, the confinement in one dimension leads to an infinite sheet that is called a "quantum-well". Here, distinct plateaus in the DOS diagram arise, where each plateau corresponds to a state within the quantum-well, similarly to a potential box. Further reduction in dimensionality leads to the quantum wire with confined states in two dimensions. The DOS diagram begins to reveal the advantage of increased confinement and peak-like functions emerge, having a high DOS at the edge and declining for higher energies until the next level is reached. A total separation of the peaks can be reached with QDs, where the confinement is in all three dimensions and delta-peaks appear in the DOS diagram.

This system is now identical to a single atom and this is why QDs are often called artificial atoms. In terms of gain, this is the most desirable configuration because there is only one allowed state, so everything has to couple to it and no other states are allowed. The height of the peak depends on the number of identical QDs, therefore this confinement method acts like a concentrator where the contribution of each QD to the gain adds up. Due to this concentration, the maximum achievable material gain with QDs can be as high as 10^4 cm^{-1}, compared to bulk material with about 10^3 cm^{-1}.

The transparency condition in an active medium refers to the case where the pump level is high enough to fill up all excited states, so that the medium becomes lossless. This is an important feature in respect to the device performance because the threshold current density is always higher than the transparency current density calculated by [Ustinov07]:

$$J_{tr} = \frac{eN_{QD}}{\tau_r} \quad \text{(Eq.2.8)}$$

where N_{QD} is the surface density of the QDs and τ_r the radiative lifetime. It is now clear that for a given radiative lifetime, J_{tr} is proportional to the amount of QDs that needs to be pumped and can be as low as 5-10 A/cm^2. Keeping the threshold low not only helps with the power consumption of the device but also with the generated heat inside the device.

The 3D confinement of the carriers inside the QDs logically reduces the diffusion out of the QDs. Diffusions of carriers has to be minimised because it results in a reduced efficiency, mainly because the carriers diffuse out of the QDs and to exposed surfaces, where they can recombine non-radiatively. The number of carriers lost to surface recombination is particularly high in photonic-crystal devices where a high number of surfaces are exposed due to the nature of etching the photonic-crystal. Therefore, we chose QDs as the gain medium, where the carriers are laterally confined by the dots and the effect of surface recombination is much reduced [Moore06]. Heating should be avoided in lasers because it detunes the cavity resonance as well as increasing the non-radiative recombination, thus reducing the gain.

The properties described so far refer to an ideal QD system, but are different in a real one. QDs are usually grown by a hetero-epitaxial growth process with a material of slightly different lattice constant than the substrate, referred to as Stranski-Krastanov [Stranski38] growth method as illustrated in Figure 2.4 (a). In the growth reactor, a wetting layer with a slightly smaller lattice constant in grown on top of the substrate and, after stress due to lattice mismatch, leads to the growth of distinct but also random islands: the QDs (Figure 2.4 a). This is a relatively easy and effective way to produce a high number of QDs. The problem with this method is the randomness in size of the QDs. The energy-width of each QD is homogeneously broadened due to a finite lifetime of the carriers resulting in a Lorentzian lineshape (Figure 2.4 b), and the centre position is mainly determined by the dot size. In a real system, where the dot-size distribution is random, the assembly of all QDs results in a Gaussian distribution depending on the size-percentage distribution of the QDs. Typical values for the homogenous linewidth in wavelength are 5-10 nm and 30-60 nm for the inhomogeneous linewidth [Ustinov03].

Nevertheless, with this method QD lasers have been fabricated with high material gain, ultra-low threshold densities, and large wavelength flexibility due to a various number of tuning possibilities during growth.

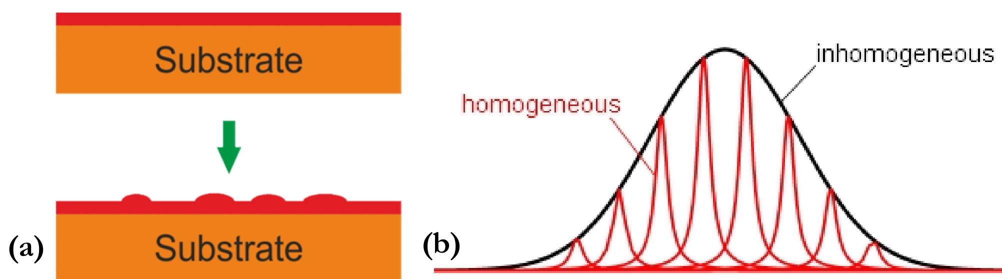

Figure 2.4 Stranski-Krastanow growth (a) of QDs on a substrate with slightly larger lattice constant than the wetting layer (red layer). Due to strain and lattice relaxation, islands form on the wetting layer in a self-assembled way. The variation of QD size results in inhomogeneous broadening of single homogenously broadened QDs (b).

2.2.3 Photonic-Crystal Cavity

The propagation of light in a generic, dielectric medium is ruled by the set of *Maxwell's equations* in a charge-less vacuum:

$$\nabla \cdot E = 0 \tag{Eq.2.9}$$

$$\nabla \cdot B = 0 \tag{Eq.2.10}$$

$$\nabla \times E = -\frac{\partial B}{\partial t} \tag{Eq.2.11}$$

$$\nabla \times B = \mu_0 \varepsilon_0 \frac{\partial E}{\partial t} \tag{Eq.2.12}$$

These forms were already known by Gauss, Faraday and Ampere, but Maxwell modified and combined them in order to describe classical electromagnetism. Here, E and B are the vector electric and magnetic fields, and μ_0 and ε_0 the vacuum permittivity and vacuum permeability, respectively. The first two equations imply that there are no point sources but always closed loops of the fields. The other equations show that it is possible to create an electric field by a modulation of the magnetic field and vice versa. Combining all four equations leads to the fundamental *electromagnetic wave-equation* that describes the propagation of any electromagnetic radiation:

$$\nabla^2 E = \mu_0 \varepsilon_0 \frac{\partial^2 E}{\partial t^2} \tag{Eq.2.13}$$

This equation describes the case for the electric field but is also valid for the magnetic field; it implies that the field replicates through its own second derivative, which only allows sinusoidal solutions, meaning that the radiation propagates as a

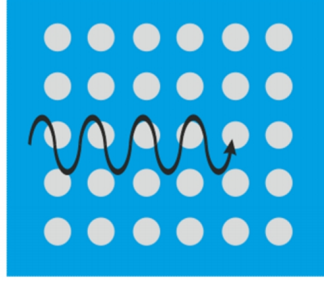

Figure 2.5 Schematic wave propagation within a periodic modulated medium, with two different dielectric constants (blue and grey).

wave. Additionally, with the knowledge of Eq.2.11 and Eq.2.12 the wave propagates because the electric field creates the magnetic field and the magnetic field creates the electric field, continuously. Unlike sound-waves, electromagnetic-waves do not require a medium, because of the continuous generation of the fields and can therefore also travel in vacuum.

We have now introduced the wave-equation describing the general propagation of light, but what makes a photonic-crystal? A photonic-crystal (PhC) is a medium with periodic dielectric constant modulation (Figure 2.5). In periodic modulated structures, waves propagate as a *Bloch-Wave* with eigenstate function H calculated after:

$$H(r+R)=e^{ikR}H(r) \tag{Eq.2.14}$$

Here, the eigenstate function H at a vector r repeats itself in a translational symmetric structure with the lattice vector R, where the term e^{ikR} represents a plane wave. The physical meaning of R is that there exists a primitive cell that replicates itself in every periodic structure. In the plane wave term, k is the wavevector and it is useful to perform calculations in k-space where r and R are the position and lattice vectors, respectively. Solving Eq.2.14 determines the eigenstates of a periodic structure is performed e.g. by plane wave expansion method, where the periodic structure is Fourier transformed into a sum of sines and cosines, hence plane waves. The dielectric constant as well as the field distributions are first transformed, then fitted into the combination of Eq.13 and Eq.14, and solved for unknown parameters. Each eigenvector (wavevector) and eigenstate (frequency) can be calculated

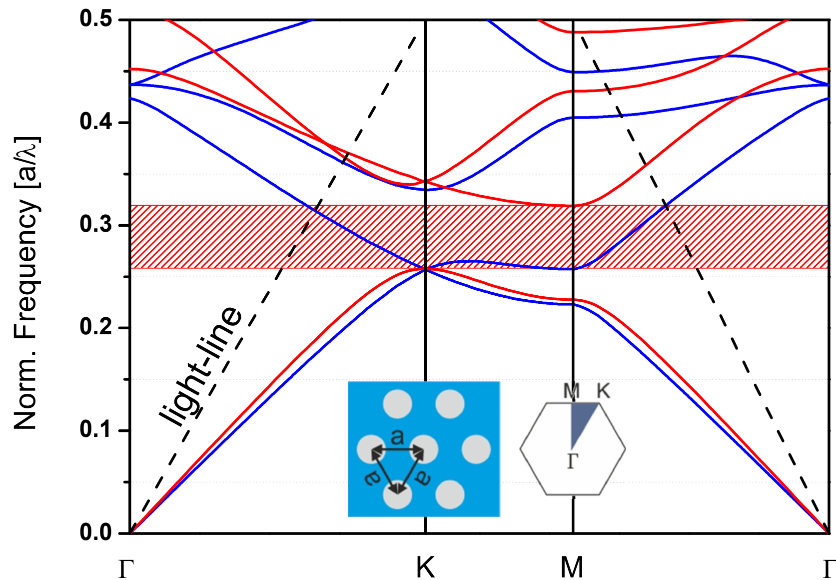

Figure 2.6 Band-diagram of a two-dimensional plane ($\sqrt{\varepsilon_1}$ = n_1 = 2.8) with hexagonal array of air holes (n = 1, r/a = 0.29), as shown in the left inset. The directions of wavevector are shown in the right inset with specific points corresponding to the graph. The red lines show the bands with the electric field in-plane (TE modes) and the blue lines show the bands with the magnetic field in-plane (TM modes). In this structure, there is only a band-gap for TE mode. The light-lines are indicated as dashed lines.

by e.g. MIT Photonic-Bands package (MPB) and plotted in a band-diagram, as shown in Figure 2.6. The band-diagram, also know as dispersion diagram, shows the frequency of modes for each wavevector corresponding to the specific points in the inset. Because the structure is periodic, only a certain region in k-space – known as first Brillouin zone – needs to be plotted, resulting in folding of the higher bands. The light-line (dashed line in Figure 2.6) is important in real three-dimensional structures – slabs – where modes below the light-line are guided and radiate above. The steepness of the light-line depends on the cladding material according to $\omega/ck = 1/n$ and is steeper for low index claddings. In a purely two-dimensional simulation the modes are separated in having either the electric field (transverse electric, TE) or magnetic field (transverse magnetic, TM) in-plane. A band-gap represents a frequency range with no allowed states – DOS = 0 – so that no TE modes are visible inside. The band-gap condition refers to the Bragg condition being fulfilled in all directions, i.e. light is, in principle, perfectly reflected; this is particularly

interesting for laser applications, as the band-gap regime provides a perfect feedback mechanism.

2.2.3.1 Ln-Type and Pure Line-Defects

Within the gap there are no allowed states in any direction of dielectric constant modulation, so that when a defect is introduced, the mode is, in principle, perfectly localised by the defect. Defects can be made in different ways, such as reducing or increasing the size of holes, or even removing holes. In the former case, modes are then shifted from the top or the bottom of the gap depending on degree of modification. These defects are referred to as donor or acceptor defects, analogous to dopants in semiconductors. Here, we concentrate on the case where holes are completely removed. Starting by removing one hole (L1 cavity) from the perfect PhC, a confined defect mode appears within the gap (Figure 2.7).

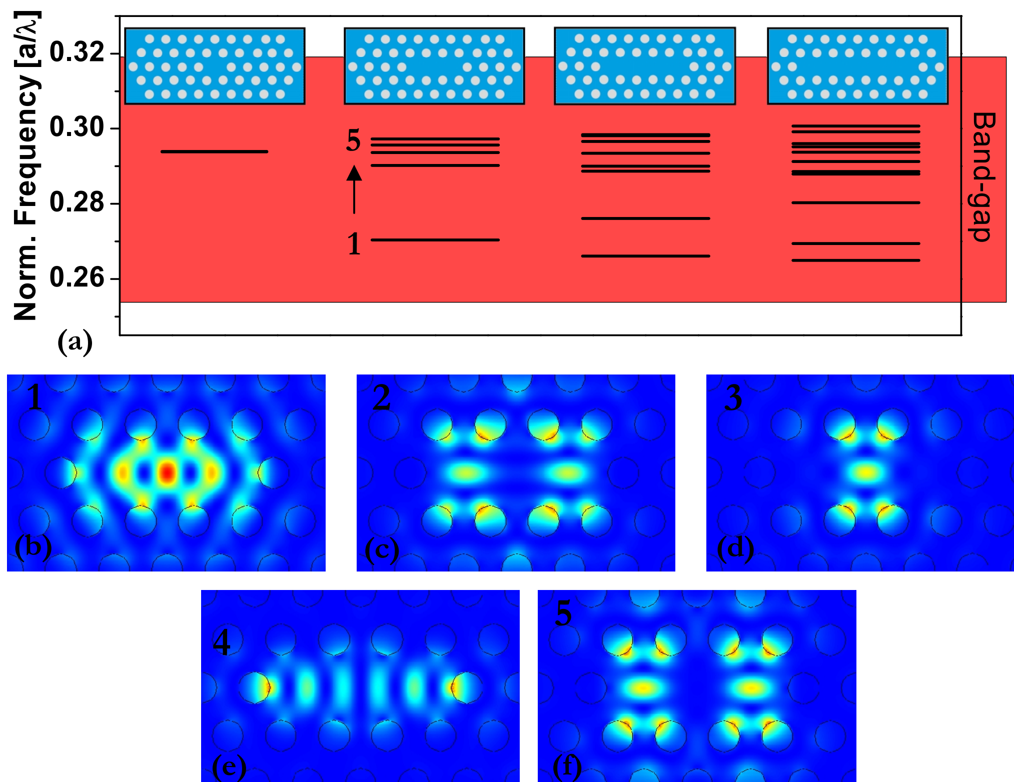

Figure 2.7 Overview of confined defect modes within the band-gap for one, three, five and seven missing holes (a). Squared electric field distribution for the modes of the L3 cavity with the fundamental mode in (b) and higher order modes in (c-f).

Because this L1 cavity is symmetric around the origin, the mode is degenerate in nature. Degenerate modes are special modes with two different field distributions at the same frequency. When three holes (L3) are removed, more modes appear within the gap because the cavity is larger and can accommodate more modes and so on for the L5 and the L7 cavity. The lowest frequency mode of such a cavity (Figure 2.7 b), i.e. the fundamental mode and, tends to be the mode with the highest Q-factor.

The removal of a complete row of holes corresponds to the case of a W1 waveguide, whereas two removed rows correspond to a W2 waveguide and so on. For calculations on this W1 waveguide mode, we only have to consider the wavevectors along the waveguide (arrow in Figure 2.8 b) because the structure is periodic only in this direction. Two modes appear in the gap the lower frequency mode being even (Figure 2.8 b) and the higher frequency being odd (Figure 2.8 c) with respect to their out of plane magnetic field distribution. Both bands cross at some point, but do not couple due symmetry mismatch, at least in the 2D model system. In comparison to the modes of the cavities in Figure 2.7 (a), we see that the fundamental mode frequency converges when increasing the number of missing holes. For a very high number of missing holes this frequency corresponds to the

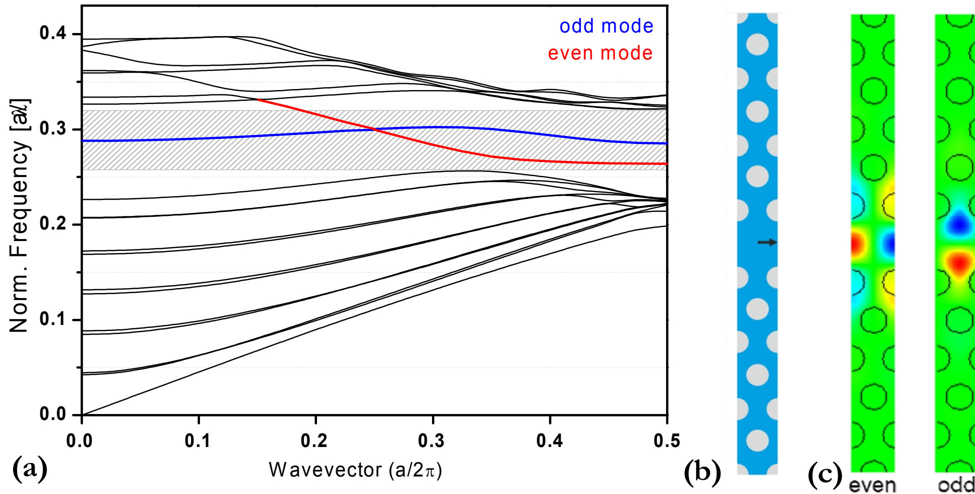

Figure 2.8 Band-diagram of W1 waveguide (a) along the line-defect corresponding to (b). The band-gap is marked as the grey box with two defect modes (even and odd), distinguished by their mirror symmetry of the out-of plane magnetic field in lateral direction (c).

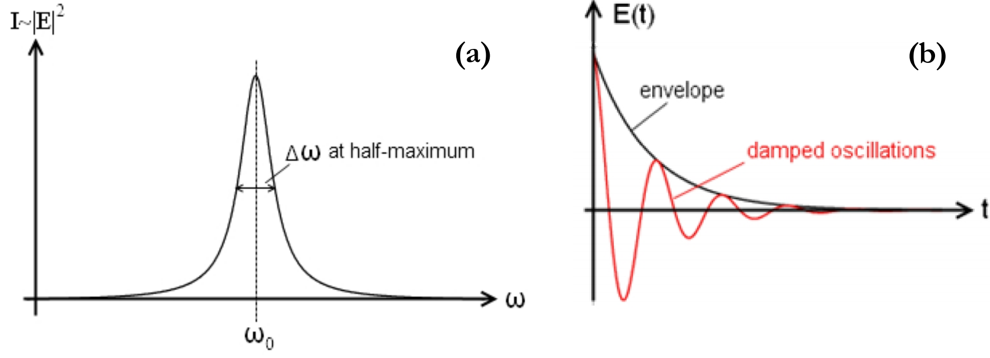

Figure 2.9 Lorenzian cavity peak with the centre frequency and the frequency-width at half-maximum (a). Field-decay in time in form of a damped harmonic oscillation with an exponential envelope (b).

frequency of the W1 even mode at the band-edge (Figure 2.8 c). Because the group velocity is given by the slope of the dispersion curve at this point is very low and the DOS is proportional to the group velocity, the DOS at the band-edge is much higher than elsewhere.

2.2.3.2 Q-factor of a Cavity

So far, we have considered only the centre frequencies of the cavity resonances. These resonance lines are further broadenend by their lifetime, as illustrated in Figure 2.9 (a). The shape of the intensity peak is a Lorentzian with height I_0, peak centre ω_0 and width of the peak at half maximum of $\Delta\omega$. In order to describe $\Delta\omega$, we start with the field decay in a cavity that is a damped sinusoidal harmonic oscillation after Figure 2.9 (b) and is written as:

$$E_{(t)} = E_{(0)} e^{-t/\tau} \sin(\omega_0) t = E_{(0)} e^{-t/\tau + i\omega_0 t} \qquad \text{(Eq.2.15)}$$

where E_0 is the maximum field amplitude, τ a decay constant and ω_0 the centre frequency. The exponential term gives the decay and the sinusoidal function gives the real part of the harmonic oscillation. Because we are interested in the intensity distribution in frequency-domain, we have to Fourier-transform the modulus squared of Eq.2.15 resulting in:

$$\left|E_{(\omega)}\right|^2 = \frac{\left|E_{(0)}\right|^2}{(\omega_0 - \omega)^2 + (1/\tau)^2} \tag{Eq.2.16}$$

This expression is know as Cauchy–Lorentz distribution and gives the intensity distribution in frequency, as shown in Figure 2.9 (a). Let us now define a new unitless figure-of-merit, because τ has a unit of time. We first take the value of $|E(\omega)|^2$ at half-maximum,

$$\frac{\left|E_{(0)}\right|^2}{(\omega_0 - (\omega_0 + \Delta\omega/2))^2 + (1/\tau)^2} = \frac{\left|E_{(0)}\right|^2}{2(1/\tau)^2} \tag{Eq.2.17}$$

where we have used the frequency at the half-width on the left-hand side ($\omega = \omega_0 + \Delta\omega/2$) and halved the value of the maximum frequency ($\omega = \omega_0$) on the right-hand side. After a little algebra, we obtain:

$$\frac{1}{\tau} = \frac{\Delta\omega}{2} \tag{Eq.2.18}$$

and see that $\Delta\omega$ corresponds to the inverse of the field decay τ inside the cavity. After normalisation by ω_0 we get:

$$\frac{\tau\omega_0}{2} = \frac{\omega_0}{\Delta\omega} \tag{Eq.2.19}$$

The right-hand side gives now the ratio of the centre frequency to the full-width at half-maximum and can be taken as a unitless figure-of-merit:

$$\boxed{\frac{\tau\omega_0}{2} = Q = \frac{\omega_0}{\Delta\omega}} \tag{Eq.2.20}$$

where Q is the *Quality-factor* of the cavity and describes the field-decay inside the cavity, as well as the width of the peak in respect to the centre frequency.
The Q-factor is alternatively defined as:

$$Q = 2\pi \frac{Energy\ Stored}{Energy\ dissipated\ per\ cycle} \tag{Eq.2.21}$$

As a final remark, we calculate the total Q-factor of a structure with different rates of loss in e.g. different directions. Considering different time decays τ, the dominant one is the shortest decay time. Therefore we write:

$$\frac{1}{\tau_{tot}} = \frac{1}{\tau_{||}} + \frac{1}{\tau_{\perp}} \qquad \text{(Eq.2.22)}$$

where the total time-decay consists of decay in-plane (||) and out-of plane ($\perp$). Since the Q-factor is proportional to the time-decay we can use the following:

$$\frac{1}{Q_{tot}} = \frac{1}{Q_{||}} + \frac{1}{Q_{\perp}} \qquad \text{(Eq.2.23)}$$

Now, different Q-factors of a structure can be combined in this way to calculate the total Q-factor.

2.3 Review of Selected Devices

Our aim is to achieve lasing via electrical injection, so we will now review two devices where electrical injection into a GaAs PhC device has been achieved. We show the devices design and their characterisation, but mainly focus on the requirements for lasing.

2.3.1 Cavity-Enhanced Photonic-Crystal Light-Emitting Diode at 1300 nm

This device aims for an electrically driven single photon source with high extraction efficiency and employs a PhC cavity as well as QDs [Francardi09]. The structure of this LED is shown in Figure 2.10 (a). The p/i/n slab is 370 nm thick, contains one layer of low density QDs (5-7x10^{8} cm^{-2}) and is placed on top of a 1.5 µm thick $Al_{0.7}Ga_{0.3}As$ sacrificial layer. The doping concentrations of the p/n layers are not given.

The fabrication starts by the patterning of metal markers for successive lithographic step and wet-etching of the round mesa region to access the n-layer. The n-contact

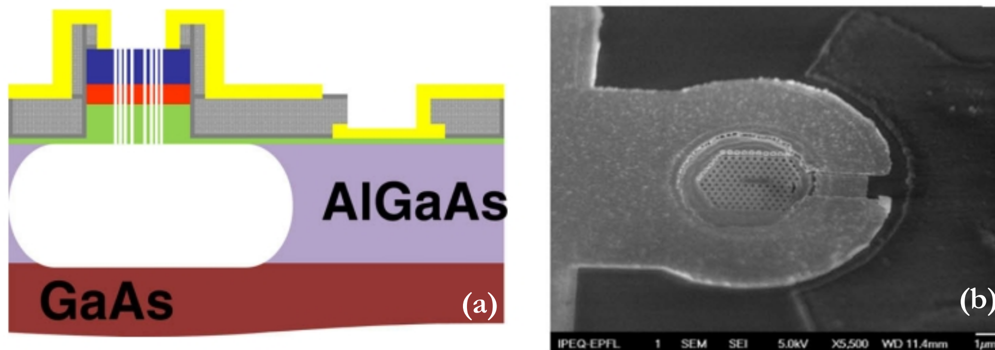

Figure 2.10 Sketch of the device in (a): p-doped layer (blue); active region containing QDs (red); n-doped layer (green); Si_3N_4 insulation (grey) and metal-contacts (yellow). SEM image in (b): round p-contact enclosing the PhC cavity with n-contact on the right. [Francardi09][3]

consists of Ni/Ge/Au/Ni/Au evaporated onto the n-layer, followed by a thermal annealing step. In the next step, an insulating Silicon Nitride layer s deposited on the sample and selectively dry-etched to re-open the mesa and n-contact regions. A tilted three step evaporation is then needed to cover the slope of the mesa with a Cr/Au metal contact. In order to create the PhC cavity, a 150 nm thick SiO_2 layer is deposited on the sample, followed by electron-beam resist. The PhC pattern is then written into the resist, developed and transferred into the SiO_2 layer via dry-etch. In a second dry-etch step, the pattern in the SiO_2 mask is transferred into the GaAs slab. Finally, to release the membrane, the AlGaAs layer is selectively wet-etched in hydrofluoric acid that also removes the remaining SiO_2 mask.
Characterisation of the device is performed at low temperatures of down to 5 K. The cavity peak of the L3 cavity is shown in Figure 2.11 with a Q-factor of about 4000. A shift between the photo- and electroluminescence is visible, due to heating of the device and condensation of gas on the sample because two different cryostats were used here. The IV curve clearly shows diode behaviour and the estimated resistance is about 330 Ω.

This device has obtained good results such as a high Q-factor and low resistance. The carrier injection scheme shows that carrier injection into the PhC is possible with a vertical stack of the p/i/n layers and a wet-etch to access the n-layer. Neither doping concentrations nor individual layer thicknesses are given, but their values

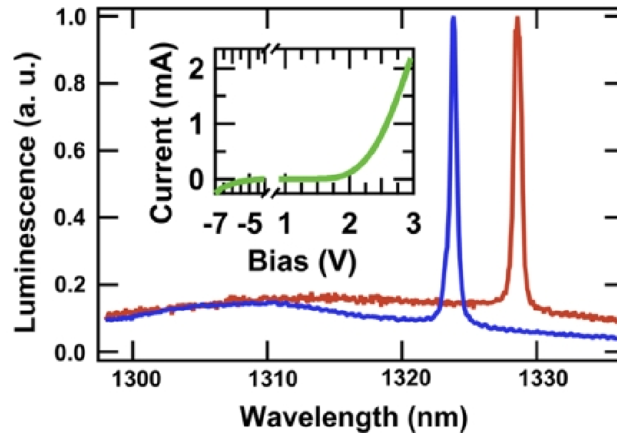

Figure 2.11 Photoluminescence (blue) and electroluminescence (red) spectra of a PhC L3 nanocavity (lattice constant = 331 nm, mesa diameter = 10 μm). In the inset the I–V curve of the same device is shown. [Francardi09][3]

seem to have been chosen correctly given that the resistance is low while the Q-factor is high.

No lasing was observed, most probably due to (1) the low number of QDs (single layer only) and (2) low carrier density inside the PhC cavity. Higher dot density and more layers are probably needed to provide more gain and to reach threshold. Operation at room-temperature (RT) would additionally increase the threshold current because the gain spectrum would broaden and most importantly, carriers would thermally escape [Mao11] from the QDs, therefore reducing the efficiency. To counteract the reduction in efficiency, the carrier injection might have to become more efficient by either optimising the doping concentration or by improving the contact design. This is important because the carriers tend to recombine close to the p-layer, due to its lower conductivity compared to the n-layer. Additionally, the low heat dissipation out of the membrane due to the low thermal conductivity of air could make RT operation difficult.

Overall, this device provides a good demonstration of electrical injection. Moreover, it shows a good starting point for further optimisation in order to achieve lasing.

2.3.2 Ultralow-Threshold Electrically Pumped Quantum-Dot Photonic-Crystal Nanocavity Laser

This device is different in terms of carrier injection because it employs laterally doped regions, as shown in Figure 2.12 [Ellis11]. Here, the current is mainly flowing over the L3 PhC cavity due to the tapered doped regions. Further current restriction is achieved through a horizontal trench. Concerning the material properties: the GaAs slab is 220 nm thin, contains 3 layers of high density QDs ($3x10^{10}$ cm^{-2}) and lies on a 1 µm thick $Al_{0.95}Ga_{0.05}As$ sacrificial layer. At first, the doped regions need to be created, starting with the n-doping. Therefore, a Silicon Nitride mask is deposited on the sample and the doped regions are dry-etched to expose the GaAs slab. Silicon-ion implantation is then performed and the remaining mask removed with another dry-etch. The same procedure is carried out for the n-doped region, followed by dopand activation at 850 °C in a rapid thermal annealer. Prior to annealing, a 40 nm silicon nitride cap layer is again deposited on the sample in order to prevent the out-diffusion of arsenic. After the removal of the cap layer, a lateral p/i/n structure is obtained. The PhC definition is performed by an electron-beam written resist and the successive dry-etch to transfer the patter from the resist into the GaAs slab. At this step, the trenches are included as well. The AlGaAs layer

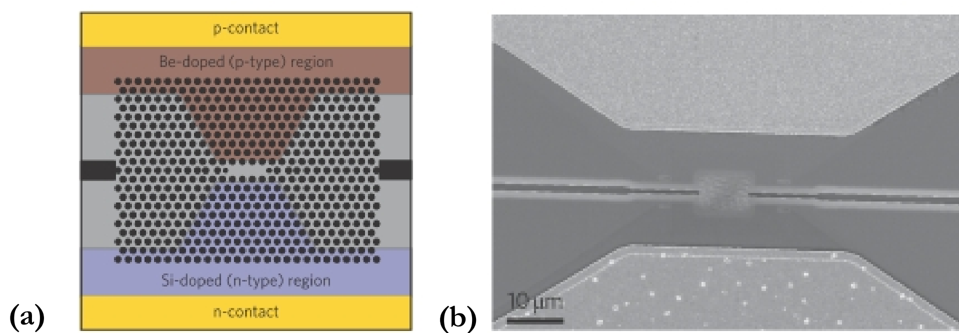

Figure 2.12 Schematic of the electrically pumped photonic-crystal laser (a). The p-type doping region is indicated in red, and the n-type region in blue. The width of the intrinsic region is narrow around the cavity to allow for direct current flow into the active region of the laser. A trench is added to the sides of the cavity to reduce leakage current. SEM image (b) of the fully fabricated laser. The p-side of the device appears on the top of the image, and the n-side on the bottom. [Ellis11][4]

is then wet-oxidised at 465 °C before the n-contact and p-contact are lithographically defined. The n-contact and p-contact composition is Au/Ge/Ni/Au and Au/Zn/Au, respectively. An annealing step for the contacts is performed at 415 °C, before completing the device by dissolving the sacrificial layer in potassium hydroxide solution and releasing the membrane.
In the final device, the n- and p-concentrations are 6.0×10^{17} cm^{-3} and 2.5×10^{19} cm^{-3}, respectively, and allow current flow with diode behaviour (Figure 2.13 a). The current-voltage behaviour is acquired at 50 K with an estimated device resistance of 3500 Ω. Lasing is identified in the light-current curves (Figure 2.13 b), but only at temperatures of 150 K or lower. Higher temperatures do not allow lasing. With decreasing temperature the threshold current drops from 287 nA at 150 K to 181 nA at 50 K. The Q-factor is about 1.100 with a resonance wavelength at 1174 nm.

Overall, ultra-low threshold lasing has been achieved with this device due to efficient carrier injection and low temperature operation. Due to locally doped regions, the current flow is efficiently directed through the PhC cavity within the full slab. It is possible to estimate the threshold current density if we assume a cross-section of the current flow: width x height = 2.7 μm x 0.22 μm = 0.59 μm^2 = 5.9×10^{-9} cm^2.

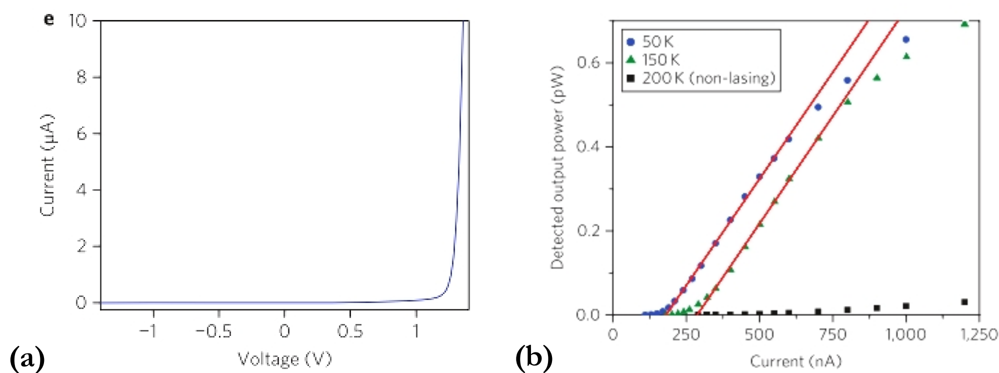

Figure 2.13 Current–voltage characteristics of the laser taken at 50 K in the dark (a). Experimental output power (detected on the spectrometer) as a function of the current through the laser (b) at 50 K (blue points), 150 K (green points) and 200 K (non-lasing; black points). Red lines are linear fits to the output power of the lasers, which are used to determine the thresholds. We estimate from the collected output power that the total radiated power of the laser above threshold is on the order of a few nanowatts. [Ellis11][4]

The effective cross-section is obtained by multiplying the PhC material filling factor 0.67 with the cross-section, resulting in $4.0 \times 10^{-9} cm^2$. The current densities at threshold are then $287 nA/4.0 \times 10^{-9} cm^2$ ~ $24 A/cm^2$ per QD layer at 150 K and $181 nA/4.0 \times 10^{-9} cm^2$ ~ $15 A/cm^2$ per QD layer at 50 K. These values are very good if one considers that only a few hundreds nanoamperes are used to pump these lasers. The threshold current densities are also of the order of magnitude for common stripe laser [Ustinov03]. At room-temperature, on the other hand, lasing is more difficult to achieve. Beside the thermal escape of carriers out of the QDs, non-radiative recombination strongly dominates [Marko05] and can lead to a 10-100 fold increase in threshold current density. Because of this, a higher Q-factor is needed to keep the threshold as low, and to reduce heating of the device. In particular, the high doping of the p-region of $2.5 \times 10^{19} cm^{-3}$ seems very high so that the overlap with the optical mode needs to be minimised in order to further increase the Q-factor. Another important aspect is the low temperature operation together with the high temperature annealing, as this combination does not only induce a blue shift of the QD emission spectrum but also a narrowing and an increase of the photoluminescence [Shi04]. These features are linked to the gain of the material so that it might be that the gain at low temperatures is higher than at RT, and lasing at RT would be even more difficult to achieve. In terms of thermal properties, the membrane configuration might not be suitable for RT continuous-wave operation, similar to the previous device [Francardi09]. Here, the low temperature is again beneficial, as it can be seen from Figure 2.13 (b), where the curve at 50 K reaches higher output power than the curve at 150 K. This is due to thermal rollover and confirms poor heat dissipation of the membrane, where only low temperature lasing is observed. This device presents a highly efficient way of injecting carriers into the PhC cavity, but only low temperature lasing is achieved because of poor device design and the many beneficial factors of low temperature operation. Various factors need to be optimised in order to obtain the more difficult RT lasing.

We have seen that QDs are perfect for the use as a gain medium in nano-lasers, because they provide high material gain and a low transparency current density. In combination with a PhC cavity, they make efficient nano-emitters.

The two devices we have reviewed show QD emission in a PhC cavity due to carrier injection. Although these devices differ in design and performance, we state key points that we have to consider when designing our device:

- high number of QD layers: > 3 layer
- Q-factor in the range of 1000's, depending on the gain
- efficient carrier injection, ten's of A/cm^2 per QD layer necessary
- resistance can be in the range of 1000 Ω's
- heat sinking is needed when current densities are high

The first device used 1 layer of low density QDs with a Q-factor of 4000. No lasing was achieved there. In the second device, on the other hand, the Q-factor was lower with about 1000, but lasing was achieved due to 3 layers of QDs. We can conclude from this that the number of QD layer seems more important than the Q-factor of the cavity. The Q-factor helps to keep the threshold current density low as well as efficient carrier injection into the cavity. Lasing should be possible, if we can achieve ten's of A/cm^2 per QD inside the cavity. In terms of heating, high current densities in combination with high resistance leads to heating of the device. Heat sinking is preferred when operating at RT to avoid any disturbance of the device operation.

In the next chapter, we present our design for an electrically pumped PhC laser at RT and analyse its performance by various calculations and simulations

Chapter 3

Design and Simulations of ePCL

3.1 Introduction

As seen before, a number of different photonic-crystal lasers (PCL) have already been demonstrated, yet they never fully fulfil all three criteria for a practical device: *electrical* injection, *optical* feedback and *thermal* efficiency (Figure 3.1). Here, we attempt combine all three properties for the ultimate laser to operate cw at RT. Finding a balance between these properties is a difficult task, because they clearly influence each other. The ultimate solution for finding the optimum parameters requires a calculation involving both carriers and photons and considering electrical, optical, thermal properties for the different structures. Such a calculation can be implemented using either a finite-element-method (FEM) or finite-difference time-domain (FDTD). Attempts of partial implementation of laser dynamics were already presented in [Mock10], [Nozaki05], [Grine07]. Modelling of a complete electrically

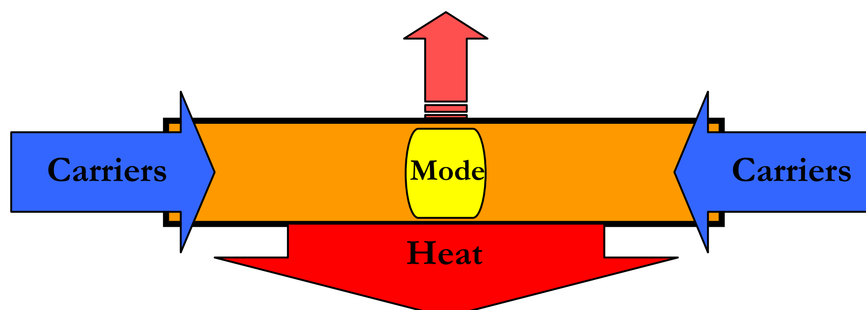

Figure 3.1 Schematic principle of practical laser combing all three properties: electrical injection via carriers, optical mode generation in a resonator and heat dissipation out of the medium.

pumped PCL, within one method, would be beneficial in terms of its operating behaviour, however, this is a complex and time consuming task and would be difficult to achieve considering the complexity of its fabrication as well. We, on the other hand, split up the device in electrical, optical and thermal properties and simulate each of them with an appropriate method as it will be shown in the following.

We follow a different route that is to learn from published devices and then extending them in order to achieve the goal of managing all three properties, which is an efficient way to approaching the complexity of this task. Published devices provide information about optical properties like Q-factors and gain necessary for lasing. Extending this with the knowledge and calculation of electrical, optical and thermal properties should lead to a suitable solution.

In the following sections we will show how we determined parameters for the wafer growth in separate sections: electrical, optical and thermal. For each section, certain parameters are defined that have to be optimised, considering some overlap with other sections.

3.2 Electrical Properties

3.2.1 Definition of the Electrical Model

The main aim of optimising the electrical properties is focussed on *efficient carrier injection* into the active region. In other words, as many carriers as possible should reach the active region in order to achieve the transparency/threshold condition and also to keep the threshold current low. From the practical point of view, however, the more carriers are injected, the higher is the heat produced inside the device due to resistive Joule-heating. Therefore, we have to optimise the following parameters:

- *Device resistance:* Should be minimised, to keep the applied voltage low for a certain amount of current and to reduce heating of the device.
- *Current density:* Should be maximised in the region of the optical mode, in order to reduce the leakage current and threshold. This will also keep the heating of the device at a possible minimum.

First of all, a device geometry must be chosen; different geometries are distinguished according to the direction of the current flow that is either *vertical* or *lateral*. The former is used in stripe-waveguide devices such as commercial laser-diodes where low resistance is achieved by current flow across highly doped layers and large areas (micrometres x millimetres) and over short distances (micrometres). The drawback of this configuration is the weak optical confinement in the vertical direction as conductive cladding layers are needed that have high refractive indices around a value of 3. If a microcavity, and in particular a PhC cavity, would be used in this type of geometry, the Q-factor would be very low because of the lack of vertical confinement. Carrier injection purely in the lateral direction maximises the available refractive index difference, as no cladding layers are needed. This geometry was first demonstrated for a III-V PhC device by *Long et al.* [Long09] and low-temperature lasing was obtained by *Ellis et al.* [Ellis11]. With no doubt, lateral injection is highly efficient, as the doping of the layers can be relatively high and the layer dimensions large. The specific design realised in [Ellis 11], however, requires implantation facilities, so this type of device cannot be fully fabricated at St Andrews. Lateral injection in general is a neat solution, however, but the pn-junction should be in the vertical direction so that it can be grown epitaxially. This is the appraoch we will pursue so that the carriers are transported laterally and radiative recombination occurs when electrons and holes recombine over the vertical pin-junction, as shown in Figure 3.2. The carriers are injected through corresponding metal-contacts and transported via the p- and n-doped GaAs layer into

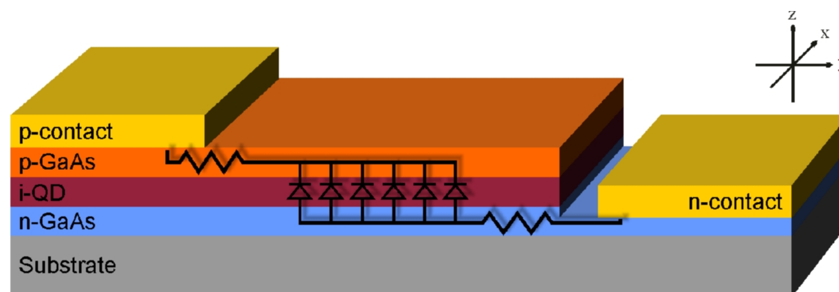

Figure 3.2 Cross-section through the vertical pin-junction with lateral carrier transport. Holes/electron are travelling over the p-GaAs/n-GaAs layer, experiencing a series resistance and recombining in the intrinsic layer (diode) containing the QDs.

the region of interest. The order of the layers was chosen to have the p-GaAs layer on top due to its lower conductivity and implying that recombination takes place close to the p-contact. With the p-GaAs on top, the n-GaAs has to be exposed by an etching step, as will be explained in Chapter 5 "Testing of Material Properties".

Since we are interested in the total resistance of the device, the representative circuit of this structure should contain all of the contributing resistances, so should be fully written as:

$$R_{tot} = R_{p\text{-}contact} + R_{p\text{-}GaAs} + R/_{D} + R_{n\text{-}GaAs} + R_{n\text{-}contact} \quad \text{(Eq.3.1)}$$

where $R_{p/n\text{-}contact}$ are the resistance at the metal-contacts – more precisely, at the metal-semiconductor interfaces - $R_{p/n\text{-}GaAs}$ are the resistances in the transport-layers and R_D is the diode junction resistance. The i-layer in a pin-device is undoped and hence has a high resistance, but injecting carriers into it decreases the resistance until it vanishes for voltages above the threshold voltage of the diode. The contact-resistance, on the other hand, can be significant in certain devices and cannot be neglected. Their origin is the existence of a barrier – the Schottky barrier – between the metal and the semiconductor which carriers need to overcome. Techniques such as diffusion of metal-ions into the semiconductor and high doping helps to lower the barrier and to make it thin enough to allow tunneling so that low resistance contacts can be achieved. When considering devices with small geometries, $R_{contact}$ becomes larger, as it scales inversely with the contact area A[1] according to:

$$R_{contact} = \frac{r_{contact}}{A} \quad \text{(Eq.3.2)}$$

Here, $r_{contact}$ is the specific contact resistance and depends on the contact composition. Resistance lowering techniques have yielded values as low as 10^{-7}-10^{-6} Ωcm^2 [Verlangieri91]. Therefore, contacts can be an issue for microdevices as well as the resistance $R_{p/n\text{-}GaAs}$ of the transport layers. Writing down the equation for $R_{p/n\text{-}GaAs}$:

---

[1] In most lateral devices the current flows only over a fraction of the contact area, so that an effective area is more appropriate in real devices.

$$R_{p/n-GaAs} = \rho_{mat} \cdot \Delta_{geo} = \frac{1}{n \cdot e \cdot \mu} \cdot \frac{L}{W \cdot H} \qquad \text{(Eq.3.3)}$$

we can distinguish the main contributing factors in the material properties with the material resistivity ρ_{mat} and the geometrical properties Δ_{geo}. The material part contains the doping concentration n, the elementary charge e and the mobility μ whereas the geometric part is made up of the cross-section (width W x height H) of the carrier flow over a length L. In a semiconductor, the type of carrier is determined by the type of doping impurity (dopands) as materials doped with acceptors (i.e. Beryllium) conduct holes (p-type) and with donors (i.e. Silicon) conduct electrons (n-type). Therefore, the resistivity of the p/n-GaAs layer is calculated by the doping concentration $n_{p/n}$ and the hole/electron mobility $\mu_{p/n}$, assuming all dopants are activated and carriers are not flowing in the high-electric field regime. With a fixed doping concentration the mobility is fixed as well, resulting in a constant resistivity that can be influenced by the layer geometry according to Δ_{geo}. It is obvious that the resistance $R_{p/n-GaAs}$ of a layer increases with the distance L the carriers have to travel. The cross-section of the layer also influences the resistance, a smaller cross-sections leads to an increase of the device resistance. This is a critical aspect of micro-devices, where the cross-sections are in the range of tens of nanometres and the current flow is constraint. An estimation of the total device resistance can be made by assuming geometrical values, but a more accurate picture is obtained by simulating the device with a Finite-Element-Solver (FEM) like COMSOL. The analytical model presented here will serve as guidance for the following numerical section and helps with the understanding of the origin concerning the resistance for the individual terms.

Using FEM, we can investigate in more detail which parameters affect the device resistance and visualise the current density in the cavity region. Therefore, a FEM model was developed in COMSOL based on the *conductive media* model for direct-currents. Firstly, a layered structure with the p/i/n-layers is created, followed by the etched region to the n-layer and the metal-contacts (Figure 3.3), and each parameter can be changed in order to investigate its influence on device resistance and current distribution. We have chosen to use 100 nm thickness for the p- and n-GaAs and

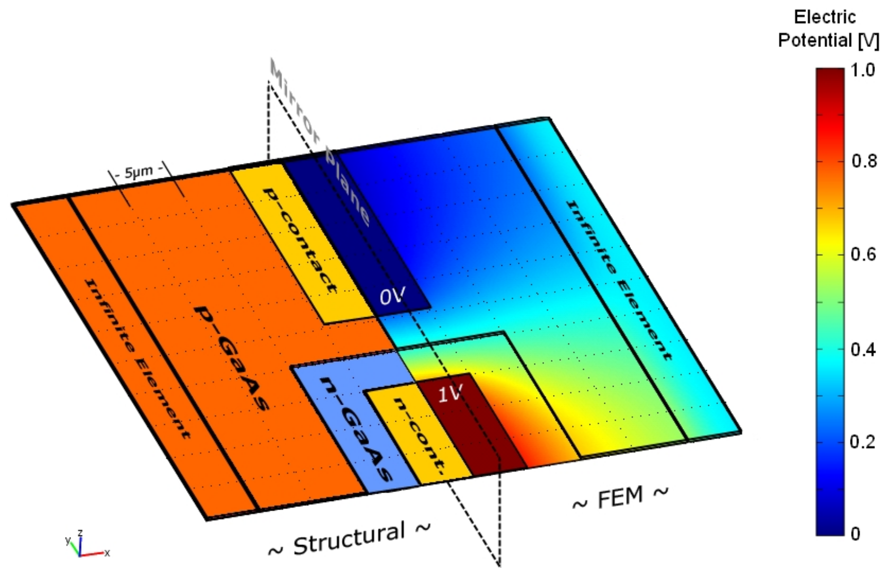

Figure 3.3 3D structural overview and voltage distribution of FEM simulation. The cross-section at the mirror-plane corresponds to Figure 3.2. Due to the mirror-symmetry condition, only the right part needs to be simulated and includes infinite elements (see text). The electric potential distribution is plotted for an applied voltage of 1 V at the n-contact and 0 V at the p-contact. The colour scaling is for illustration purposes only, with blue for low voltages fading into red for high voltages.

200 nm for the i-GaAs containing the imaginary QDs, because we want to limit the total slab thickness to around 400 nm. This means that the p- and n-GaAs have to be around 100 nm if we account 200 nm for the i-GaAs – about 30 nm of GaAs barriers. Simulation of a 400 nm thick structure that expands over tens of micrometres is a heavy computational task and we had to apply further techniques to reduce the computational demand and obtain convergence:

- Introduce a mirror-symmetry at x = 0 plane to half the domain size
- Introduce infinite elements at boundaries reduce further the domain size by stretching the infinite element section to infinity. This means that convergence can be reached with a smaller domain.
- Special meshing is used to obtain enough points in the vertical direction and a higher number of points in the region of interest – between the contacts – than in the outer regions. This is a particular strength of FEM vs. uniform-grid solver such as most FDTD methods.

- The most suitable FEM solver was selected and parameters were fine-tuned to increase computational efficiency.

With these adaptations, it was possible to obtain a simulation within minutes on a quad-core – 8 threads – workstation consuming about 8GB of RAM. A convergence study for the domain size and number of grid points was performed resulting in a maximum tolerance of 5%.

3.2.1.1 Implementation of Diode Behaviour

Since this model does not consider the hole/electron-concentration nor the carrier lifetime, but only the conductivity of a layer, we now have to implement a diode behaviour using the ideal diode formulation:

$$J_{(V)} = J_S \cdot (\exp(V / n \cdot V_T) - 1) \quad \text{(Eq.3.4)}$$

Here, the current density J depends on the voltage V in an exponential way, with J_S being the saturation current density, n is the ideality factor and $V_T = kT/q$ the thermal voltage of about 0.025 V. We implemented this diode behaviour into the i-layer by modifying its conductivity, which is generally written as:

$$\sigma = {J_{(V)}}/{E} \quad \text{(Eq.3.5)}$$

with $E = V/d$ the electric field over a distance d – thickness of the i-layer. Substituting Eq.3.4 into Eq.3.5 gives the conductivity depending on the variable E_z across the i-layer:

$$\sigma_{(E_z)} = \frac{J_S}{E_z} \cdot (\exp(E_z \cdot d / n \cdot V_T) - 1) \quad \text{(Eq.3.6)}$$

Eq.3.6 is then used as the conductivity of the i-layer with fixed conductivities for the p-/n-layer while sweeping the applied voltage V_a on the contacts. Simulated example IV curves of the structure pictured in Figure 3.2 with $J_S = 1.8x10^{-15}\ A/m^2$ [Schubert07], $n = 1$ and $V_T = 0.025V$ for different sets of layer p-/n-layer conductivities are shown in Figure 3.4.

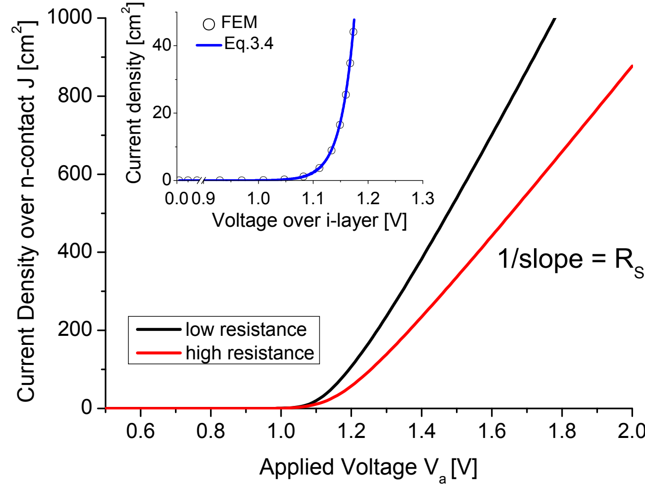

Figure 3.4 Simulated IV curves by sweeping V_a and monitoring the current density at the n-contact. Two different sets for the p-/n-layer conductivities result in different slopes of the IV curves (black and red). Inset shows the current density through the i-layer vs. the voltage drop over the i-layer for the FEM simulation (circles) and the calculated curve according to Eq.3.4.

Verification of the implementation of the diode behaviour after Eq.3.4 is done by plotting the current density through the i-layer as a function of the voltage drop across the i-layer. The simulated FEM points correspond well to Eq.3.4 (Figure 3.4 inset). Also plotting the current density at the contacts against the sweeping voltage at the n-contact while grounding the p-contact results in a diode behaviour. The resistance of the device can now be extracted from the slope at high voltages above the diode threshold. This is the way we will be obtaining the total resistance of a simulated device. The current density distribution, on the other hand, can be visualised by using cross-sections through the device.

It is important to implement the diode behaviour because not only does the current density distribution scale with current density, but also the shape of the distribution changes depending on the maximum value of the current density. This was first formulated by *Joyce et al.* [Joyce70] for a pn-junction and later analytically derived for a stripe-device[Rattier02] resulting in:

$$J_{(y)} = J_{(0)} \cdot \exp\left(-y \cdot \sqrt{\frac{J_{(0)} \cdot [(\rho_p / t_p) + ((\rho_n / t_n))]}{2V_{act}}} \right) \qquad \text{(Eq.3.7)}$$

This equation is valid for a 2D slice of our structure, shown in Figure 3.5 (a), where the current density J varies over the distance y in an exponential manner. The essence of Eq.3.7 is the change of the steepness of the curve because $J_{(0)}$ – the current density at the edge of the p-contact – is included in the exponent. Further contributing factors are the layer resistivity $\rho_{p/n}$, the layer thickness $t_{p/n}$ and the diode activation energy $V_{act} \sim 0.025\ V$. A comparison between Eq.3.7 and our FEM for different $J_{(0)}$ is shown in Figure 3.5 (b). As analytically predicted, the simulated curves decay exponentially and change their steepness for different $J_{(0)}$. Overall the agreement is very good, although there is a noticeable difference between the analytical and the FEM result, with higher deviations for low value of $J_{(0)}$. Possible explanations might be that the implementation of the diode behaviour is not exactly valid for the case of the lateral transport or that the FEM simulations are considering features that the analytical model cannot account for. Nevertheless, we will continue to use our model also because the total device resistance should not change and the maximum deviation between a FEM and the corresponding analytical curve is an acceptable 15%. In order to complete our model, we include the contact resistance at each contact-interface

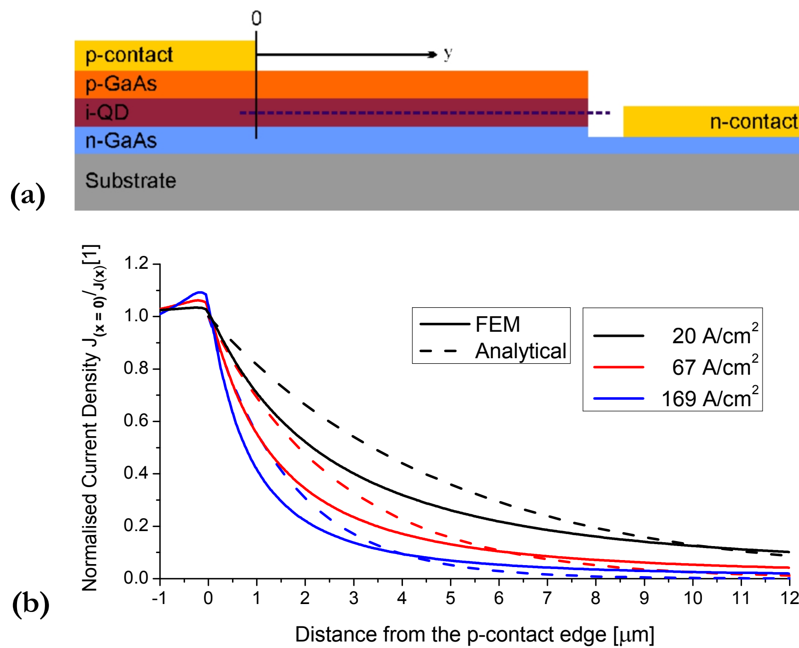

Figure 3.5 Change of current density distribution (dashed line in (a)) depending on the value for the current density at the p-contact edge (b). Higher values of current density lead to a steeper fall-off for the analytical solution and the case obtained with FEM. Parameters for the curve are: $\rho_p = 0.1\ \Omega cm$, $\rho_n = 0.007\ \Omega cm$ and $t_{p/n} = 100\ nm$.

since the contact-resistance plays an important role as well according to Eq.3.1. In the next section, the chosen parameters are scanned and the total device resistance is investigated.

3.2.2 Device Optimisation through FEM Model

3.2.2.1 Layers without PhC

Beside the device *geometry* we also investigate the effect when different *doping densities* – or layer conductivities – are used since this will partly determine the parameters for the wafer growth. The *contact-resistance* is the last parameter we change in the simulation, because due to fabrication and the relatively low doping of the GaAs-layers, a resistive barrier might form that may lead to an increase in the total device resistance.

In the vertical direction, the layer structure consists of a 100 nm thick p-/n-layer where the doping densities result in layer conductivities, a 200 nm thick i-layer with diode behaviour, and 100 nm thick high conductivity Gold contacts. Furthermore, we imitate the n-layer wet-etch by removing 320 nm from the top, resulting in a 80 nm thin n-layer.

In the first simulations the distance of the contact from the wet-etched edge is varied, as shown in Figure 3.6 (a). The corresponding result is that the total device resistance increases for larger distances in both the p-contact variation (Figure 3.6 b) and the n-contact variation (Figure 3.6 c). While varying the distance of the corresponding contact, the other contact is kept 5 µmaway from the edge. In Figure 3.6 (c) the slope of the curve is higher than in (b), which is most likely due to the thinner n-layer in the wet-etched region and the fact that the current can spread over the i-layer lowering the resistance. This means that we have to try to remove as little as possible of the n-layer during the real etch in order to keep the resistance low. The maximum resistance is around 1 kΩ with a low doping of 1×10^{17} cm^{-3} for both layers and decreases for increasing doping density down to around 200 Ω for 5×10^{17} cm^{-3}. From this point of view it is desirable to use the highest doping possible, but high doping concentrations lead to an increased amount of free-carrier absorption. This issue will be discussed and evaluated in chapter 3.2 “Optical Properties”.

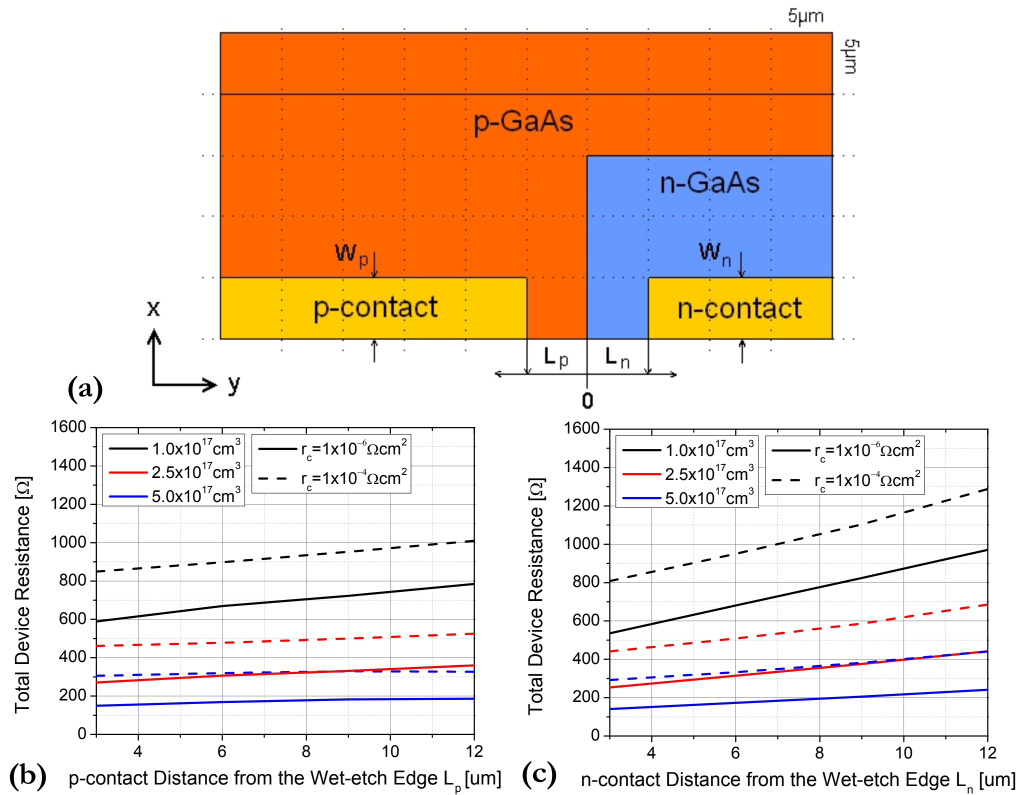

Figure 3.6 Parameter-scan for total device resistance. Top-view (a) of half-geometry with indicated parameters for contact shifts ($L_{p/n}$) from the '0' wet-etch edge and the contact widths ($W_{p/n}$). Simulated total device resistance for different values of L_p (b) and L_n (c) using three different doping densities (equal in p/n-layer) and two different specific contact resistances.

The third parameter we have varied was the contact resistance that we included in both contacts. Extremely low specific resistances of about $1\text{x}10^{-6}$ Ωcm^2 [Verlangieri91] were developed with special metal compositions and an annealing step. With this value we obtained the lowest total device resistances, shown as solid lines in Figure 3.6 (b) and (c). Moreover, a further reduction in specific contact resistance did not lead to a significant decrease in resistance, which means that in our case the value of $1\text{x}10^{-6}$ Ωcm^2 can be considered as a non-resistive contact. On the other hand, past measurements have shown that the specific contact resistance can be orders of magnitude higher in reality than the predicted value, probably due to higher evaporation pressure and a different annealing technique. Therefore, we have performed simulations with a specific contact resistance of $1\text{x}10^{-4}$ Ωcm^2, shown as dotted lines in Figure 3.6 (b) and (c). Comparison of both sets show that

the total device resistance overall increases by about 200 Ω. In summary, we can say that acceptable resistances of a few hundreds Ohms can be achieved for realistic values of the doping densities, contact resistances and contact separations.

3.2.2.2 Layers with PhC

Having determined the relevant contributions to the device resistance, we can now turn to the effect of including the PhC holes. Considering the requirement for high current densities in the PhC region, it is useful to restrict the current flow to the PhC region only. This can be achieved by adding a trench through the structure in the horizontal direction, as shown in Figure 3.7. The trench forces the current to flow across the narrow PhC region, which increases series resistance but reduces wasteful current leakage. With the trench included, we investigate the effect of the PhC on the resistance and the current density distribution within the PhC. We can expect an increase of resistance, because the cross-section of the current flow is reduced due to the presence of the holes; the cross-section is not only reduced by the physical hole-dimensions but also by the depletion layer that forms around the holes and at the slab surfaces due to Fermi-level pinning at the surface-states [Yu99]. As a result, the hole-radius seen by the carriers, increases and the conductive

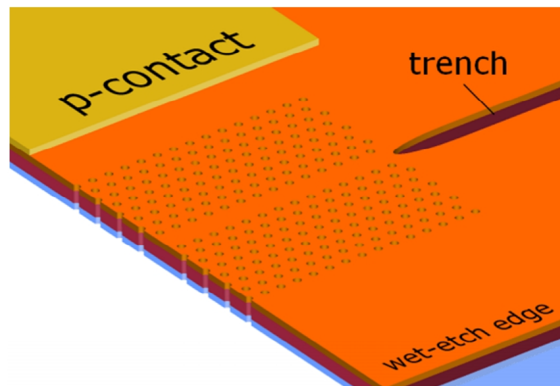

Figure 3.7 Perspective view of the FEM model geometry including PhC holes and the horizontal trench. A line-defect is introduced into the PhC to represent the optical cavity. The PhC has a lattice period of 280 nm and 60 nm hole-radius (r/a = 0.21) and covers an area of 4 µm x 4 µm. Only the right half of the PhC cavity is used, with the left edge as the mirror plane.

layer thickness at the semiconductor-air interfaces decreases by an amount calculated according to [Berrier07]:

$$\delta = \sqrt{2\varepsilon_r \varepsilon_0 \Phi_S / N_{A/D} e} \qquad \text{(Eq.3.8)}$$

where ε_r and ε_0 are the relative and the vacuum permittivity, Φ_S the surface-potential of the semiconductor, $N_{A/D}$ the acceptor or donor concentrations and e the elementary charge. Using $\varepsilon_r = 12.9$ for GaAs and an estimation for the surface-potential of $\Phi_S = 0.025V*ln(N_{A/D}/ni)$, we can estimate the depletion layer for three different doping levels, as shown in Table 3.1.

Table 3.1 Depletion Layer Width

Doping Concentration	**Depletion Layer Width**
1.0×10^{17} cm^{-3}	100 nm
2.5×10^{17} cm^{-3}	60 nm
5.0×10^{17} cm^{-3}	40 nm

These values are already in the range of the physical hole-radius and will heavily affect the device performance. An increase in the doping concentration decreases the width, but also increases the optical free-carrier absorption, as will be shown in chapter 3.2.2 "Loss and Gain Evaluation". In our case, the only way to decrease or diminish the depletion layer width is to reduce the surface state density by surface passivation resulting in a decreased surface potential. Common passivation methods employ dips in e.g. ammonium sulphide solutions where sulphide ions replace the native oxide with its high surface state- and defect-density [Baca05]. Therefore, we will not consider the depletion region in the next simulations, as we assume that the passivation technique has significantly reduced its width to a fraction of the values in Table 3.1 as demonstrated in [Sandroff89] and [Bessolov97]. Increasing the hole-radius leads to a reduction of the effective cross-section for the current flow and therefore to an increase in resistance, until the channel is completely cut and no further current flow is possible. Using FEM with different sizes of PhC holes this behaviour was replicated, as shown in Figure 3.8 a result that is very similar to that

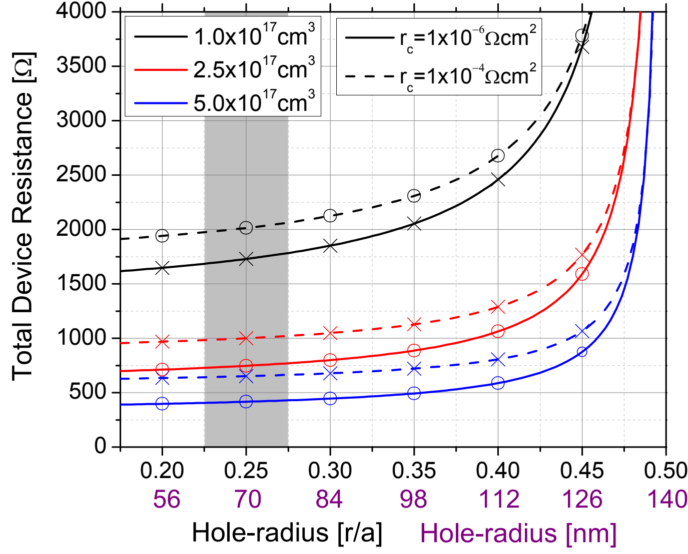

Figure 3.8 Device resistance for different hole-radii of a PhC after Figure 3.7, with 30 columns and 18 rows of holes and a period of 280 nm. The p- and n-contact positions from the wet-etch edge are 10 µm and 3 µm, respectively. The points are acquired by FEM and a hyperbolic function is used as a fit for guidance to the eye. The hole-radius is given by the r/a ratio and the value in nanometres. The grey region shows the desired working region for the hole-radius as required for the optical properties.

achieved in the Silicon system studied by colleagues in the group [Cardile11].

The simulation included, beside the PhC, also the horizontal trench so that the resistance is slightly higher than in Figure 3.6, but the current flow is also more concentrated. The characteristic of these curves is the cut-off with large hole-radius, where the resistance shoots up and the curves for both specific contact-resistances overlap because the PhC becomes the limiting factor. The fit of the curves was performed on the basic assumption that the resistance R is proportional to the distance d_{holes} between the edges of two neighbouring holes:

$$R \sim \frac{1}{d_{holes}} = A_1 + A_2\left(\frac{1}{a-2r}\right) = A_1 + A_2\left(\frac{1}{a(1-2\Delta_{r/a})}\right) \qquad \text{(Eq.3.9)}$$

where a is the period, r the hole-radius and $\Delta_{r/a}$ the hole-radius/period ratio. Two fitting parameters, A_1 and A_2 are added and the FEM points are fitted with this equation. The fitting parameters contain other resistances such as the contact-resistance and transport-layer resistance for the regions without holes, considering

geometrical values. We aim to work with as small as possible holes, but due to the difficulty of fabricating small holes, we expect be around r/a = 0.25, that is about 1000 Ω for 2.5x10^{17} cm^{-3} doping and a specific contact-resistance of 1x10^{-4} Ωcm^{2}. We now see the importance of the surface passivation, because adding e.g. 60 nm from Table 3.1 to the hole-radius moves the resistance into the steep region with strongly increasing resistance.

The resistance of the device is only one aspect related to efficient current injection into the active region. Next, we will investigate what current densities we can expect, because this is the important parameter for properly pumping the QDs. In order to determine the current density, we use the doping concentration of 2.5x10^{17} cm^{-3}, the specific contact-resistance of 1x10^{-4} Ωcm^{2} and the hole-radius of r/a = 0.25 PhC. The half-width of the contacts is kept at $W_p = W_n = 5$ µm, the n-contact position from the wet-etch edge is 3 µm while the p-contact position is varied. The resulting current-density distributions of the cross-sections at the centre of the i-layer are shown in Figure 3.9. Comparing all four cases (a-d) we can identify two distinct features. The first feature is the broadening of the distribution when comparing the cases at low voltage (a, c) with their corresponding p-contact distances at higher voltages (b, d), where the spread is wider for lower voltages. This behaviour is due to the diode characteristics shown in Figure 3.5 (b). As a result, it is more favourable to keep the voltage as low as possible, certainly considering the minimum voltage $V = E_\lambda/e$ for the emission of a photon with energy E_λ. The second point is about the position of the p-contact, as it is more favourable to be as close as possible to the cavity. The reason for this is the much lower conductivity of the p-layer in respect to the n-layer, so that the current flows as much in the n-layer as possible before redirecting to the p-contact. While these functional dependences are reasonably plausible and expected, the modelling allows us to estimate the current density in the PhC region, which is the key parameter required for achieving a given amount of gain. In order to

reach the transparency condition and later the threshold condition, we have to reach a certain current density. We assume a typical value of 6 A/cm^{2} per QD layer [Sellin01], [Li07] for the transparency current density, which is the lowest threshold current density we can obtain in a lossless resonator. Using this estimate, it becomes clear that

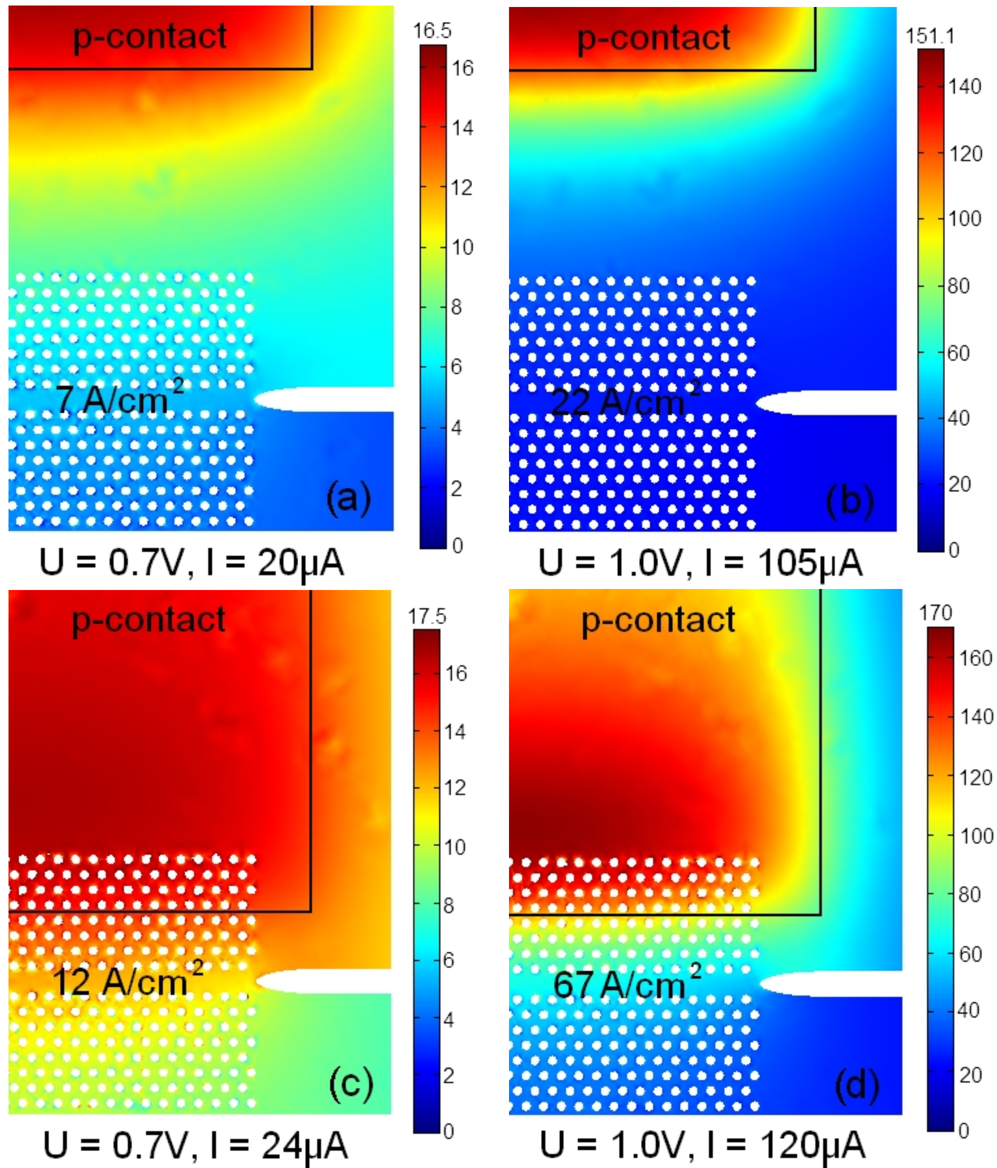

Figure 3.9 Current density distributions at the i-layer for 5 μm p-contact distance to the centre of the PhC (a, b) and 1 μm distance (c, d). At lower applied voltage of U = 0.7V (a, c) the spread is wider than for U = 1.0 V (b, d). The current density in [Acm^{-2}] at the centre is given as well as the total current (I [μA]) flowing through the contacts.

with the p-contact close to the cavity, the threshold can be reached earlier than with the p-contact further away. Going a step further, we can say that when using the above value of 6 A/cm^2 per QD layer, the device in Figure 3.9 (c) will be at transparency – with 2 layers of QDs – with a transparency current of 24 μA. This, of course, does not include leakage of loss of carriers due to non-radiative recombination processes. From then on, the actual threshold current depends on the Q-factor of the cavity and is higher than the transparency current density. A

transparency current of 24 µA would clearly be acceptable, but can certainly be reduced further by optimising the device dimensions

3.3 Optical Properties

Photonic-crystal cavities are well suited as resonators for nano-emitters because of their ability to achieve high Q-factors in small volumes. The Q-factor is an important element in achieving the lasing threshold according to:

$$\alpha_{pass} + \Gamma_{abs}\alpha_{abs} = \Gamma_g g_g \qquad \text{(Eq.3.10)}$$

where the left hand side contains all losses, such as the passive cavity and absorption losses, whereas the right hand side contains the gain. Rewriting the left hand side in terms of Q-factors [Mock10] is useful because we are interested in the Q-factor that we obtain from simulations:

$$\frac{2\pi n_{eff}}{\lambda Q_{pass}} + \frac{2\pi n_{eff}}{\lambda Q_{abs}} = \Gamma_g g_g \qquad \text{(Eq.3.11)}$$

The first addend includes the passive Q-factor that is due to the PhC cavity whereas the second addend contains additional absorption losses. In the first part of this sub-section we investigate the passive Q-factor Q_{pass} for different types of cavities and in the second part we deal with the absorptions losses Q_{abs} and the gain needed for lasing.

3.3.1 Intrinsic Q-factors for different Types of Cavities

Different cavity designs have been demonstrated incorporating *point-* or *line-defects* with experimental Q-factors of several 100.000's [Akahane03], [Song05] and even millions [Kuramochi06]. The main difference between these cavities, in respect to the achievable Q-factor, concerns *gentle confinement*. The expression gentle confinement refers to a confinement of the mode without interfering with it, which appears contradictory at first glance. In general, the PhC cavity can be seen as a potential well with a centre region surrounded by high energy barriers. A Ln-type line-defect cavity, i.e. the removal of a single hole, leads to the creation of a

confined state or mode, as explained in the section 2.1.3 “Photonic-Crystal Cavity”. This mode is only guided inside the defect but cannot penetrate deeply into the surrounding PhC and therefore decays exponentially. The combination of the guided part in the centre – which follows a sinusoidal function – and the exponentially decaying part, results in a Gaussian-like electric-field distribution. This can be seen as the analogue to the solution of the Helmholtz-equation for a waveguide. In the case of a L3 cavity – 3 holes removed – the remaining holes in the lateral direction interact with the mode, which causes a deviation from the Gaussian profile (Figure 3.10). This deviation from the ideal Gaussian distribution introduces leaky k-vector, or Fourier, components inside the radiation light-cone. Typically, the Q-factor is low if many such components are present within the light-cone. A possible way to improve the Q-factor is by fine-tuning or removing those holes that are in contact with the mode. Fine-tuning has the advantage of maintaining the mode volume and free-spectral range, while the removal of holes leads to higher Q-factors, but also to a larger mode volume and smaller free-spectral range. A fully localised mode within a line-defect can be created by modifying the line-defect, for instance by using a hetero-structure with at least two different lattice periods, as shown in Figure 3.10. This so-called hetero-structure (HS) cavity is a perfect example of a potential-well where the guiding part – with lower energy/larger period – is surrounded by higher energy/lower period barriers. Here, the field becomes

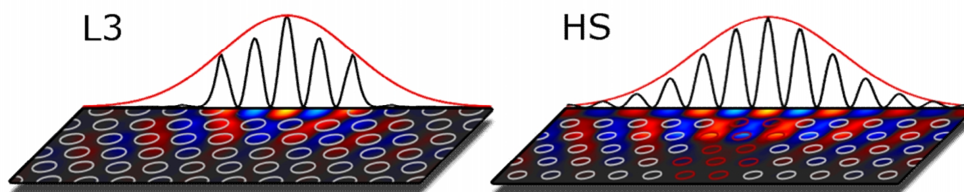

Figure 3.10 Electric-field profile of Ln-type L3 and hetero-structure (HS) type line-defect cavity. In the case of the L3 cavity, the remaining holes in the centre row disturb the electric-field profile (black curve) from a Gaussian distribution (red curve). The electric-field profile of the HS cavity is closer to a Gaussian because the centre row of holes is removed. Red and grey holes in HS represent the guiding and the mirror regions, respectively.

closer to a Gaussian distribution, therefore reducing the components within the light-cone.

Gentle confinement is even more important in the case where the light-cone expands, i.e. when using an *oxide layer* as a cladding material instead of air, as shown in Figure 3.11. The cladding improves the thermal properties of the device but also decreases the Q-factor because the critical angle for total internal refraction is reduced. The aim is now to find a cavity that can provide a Q-factor in the range of several 10.000's or more as a membrane and on oxide.

In the electrical section we used FEM to perform the simulations, but here a tool such as RSoft FullWAVE, which is specialised on optical problems, is more appropriate. FullWAVE is a finite-difference time-domain (FDTD) based software for the simulation of arbitrary structures at user defined conditions. On our 32 CPU cluster we can calculate different properties of 3D cavities, such as resonance wavelength, electric-field distributions and even Q-factors. For the optical simulations we chose 400 nm as the slab thickness and 3.4 as the slab refractive index in agreement with the electrical simulations. Figure 3.12 shows an example of a L5 cavity with 5 holes removed and a total of 61 rows of holes in x-direction and 21 rows in y-direction. These values have been evaluated in order to have the in-plane Q-factor above 10^7 and to ensure that the in-plane Q-factor does not limit the total Q-factor. Due to symmetry conditions on the mode, only an eighth of the whole computational domain needs to be used in the simulation of the membrane

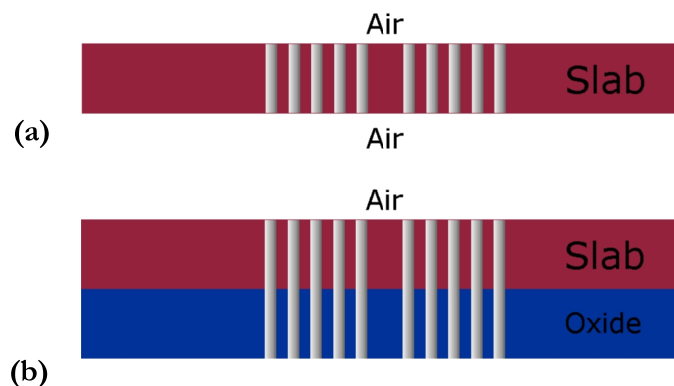

Figure 3.11 Membrane PhC cavity in (a) and perforated oxide PhC cavity in (b). The high index slab is perforated with PhC air-holes and fully surrounded by air in (a) and lying on oxide in (b).

configuration (a quarter for the oxide design), which allows a considerable reduction of the computational task. The grid-size in-plane is 16 points in one period and 10 nm resolution out-of plane. The in-plane resolution seems coarse at first glance but FullWAVE implements an algorithm that interpolates edge values of the refractive index in order to speed-up convergence and improve accuracy.

3.3.1.1 Fine-tuned Ln-Type Line-defect Cavities

Initially, the period was changed to tune the resonance wavelength in the region around 1200 nm while keeping the hole-radius over period ratio at a standard value of about r/a = 0.29. A period of 280 nm resulted in a resonance at 1220 nm for the fundamental mode, and therefore we kept a = 280 nm for the following simulations. We then apply the technique of fine-tuning of certain holes, which strongly affects the Q-factor, in order to optimise membraned Ln-type line-defect cavities cavities; the results are shown in Figure 3.13. The nearest holes in x-direction are at first reduced by a factor 0.16 – relative to r/a = 0.29 for all other holes – and then shifted outwards relative to the period. When comparing all cavities, it seems that there is no gradual increase in Q-factor when increasing the length i.e, going from L5 to L11 cavity, yet there is a jump between L7 and L9. This shows that the Q-factor

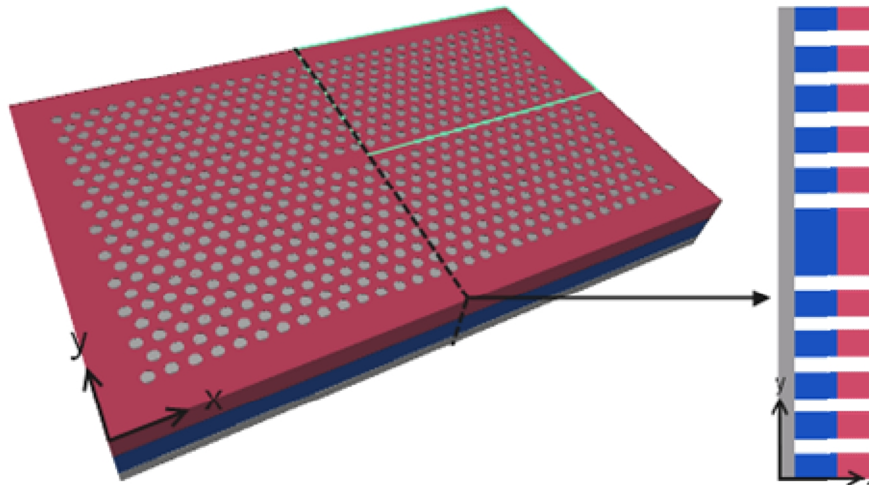

Figure 3.12 Example of L5 PhC cavity used for the FDTD simulations. This is the oxide design with an oxide layer (blue) below the 400 nm thin slab with air-hole perforations. Due to symmetry conditions only the outlined (green line) domain is simulated. The cross-section along the y-direction is pictures on the right-hand side.

reacts sensitively on the removal of holes due to the interaction of the field with the holes. In all four types, the Q-factor increases when increasing the hole-shift, until it peaks and then declines again. The peak Q-factor and the corresponding hole-shift increase when going from the L5 to the L11 cavity, so a different hole-shift must be used for each type of cavity. The value of the hole-shift is also higher than the reported value of 0.17*Period for Silicon-On-Insulator (SOI) cavities [Akahane03]. This can attributed to the increased thickness of our GaAs with respect to the 220 nm in SOI cavities. In brief summary, we can theoretically obtain Q-factors of several 100.000's for an air-surrounded membrane.

Next, the oxide cavities are fine-tuned in a similar way and the Q-factor behaviour depending on the oxide thickness is investigated. In terms of thermal and mechanical properties, it is preferable for the oxide layer to be as thin as possible, because the thermal resistance will be lower and the fabrication easier. On the other hand, a too thin oxide might cause a leakage of the optical mode into the substrate, thus lowering the Q-factor. For the next simulations, it is therefore assumed that the holes are completely etched through the oxide (n=1.6), as in Figure 3.14 (inset). All

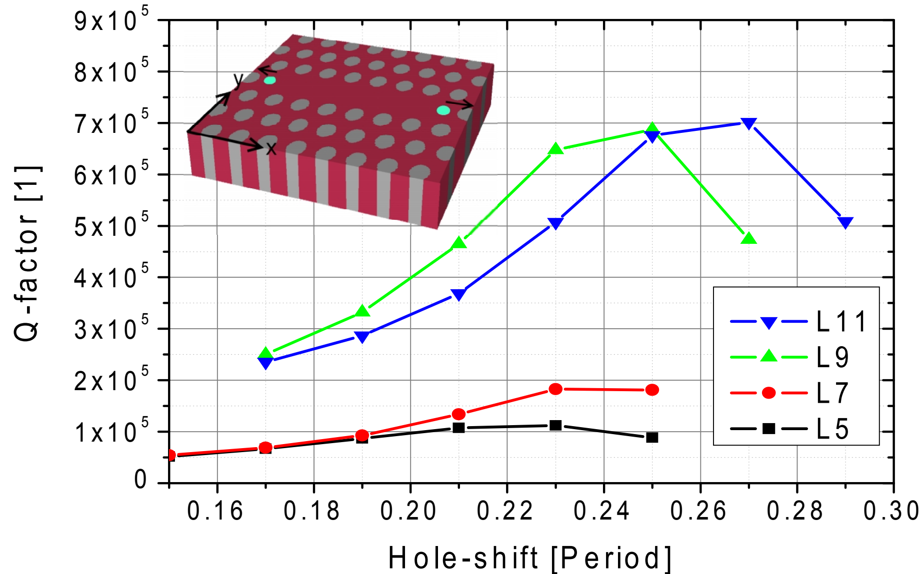

Figure 3.13 Fine-tuning of various Ln-type line-defect cavities made in a 400 nm thick GaAs slab (red) with r/a=0.29 air-holes (grey). The inset shows a L5 cavity as an example. The effect of the shifted holes (green) on the Q-factor is significant for all investigated cavities. Note that the shifted holes are also reduced in radius by a factor 0.16.

cavities show a rapid increase in Q-factor when the oxide-thickness is increased and the Q-factors seem to saturate above a thickness of about 1 µm. The Q-factor at 0.8 µm is slightly higher than at 1 µm, probably due to an interference effect at a certain oxide height, but we will not investigate this effect further. A good compromise is an oxide-thickness of about 0.5 µm because here the Q-factor drops only by 10%-20% with respect to the Q-factor at 1 µm.
Having determined the optimum oxide thickness, the effect of the hole-radius needs to be investigated because it is advantageous to use narrow holes in terms of electrical and thermal properties. The radius was reduced from r/a = 0.29 (81 nm) to r/a =0.25 (70 nm) and r/a = 0.23 (64 nm), with results shown in Figure 3.15. The Q-factor increases with decreasing hole-radius for L5 and L7 but decreases, though not dramatically, for L9 and L11 cavities.

In the case of these Ln-type line-defect cavities, we can conclude that Q-factors up to 100.000 on a 500 nm thick oxide layer can be achieved, even with reduced hole-radius of up to r/a = 0.23.

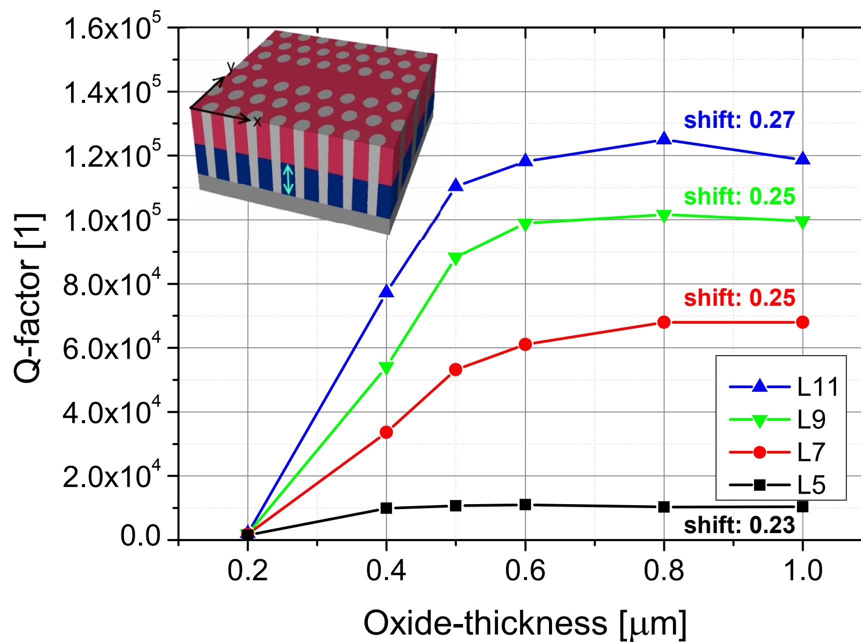

Figure 3.14 Q-factor behaviour on the oxide-thickness. The oxide is marked as a blue layer (n=1.6) in the inset. The GaAs slab is 400 nm thick and r/a = 0.29 for all air-holes except for the two fine-tuned holes (r/a = 0.29*(1-0.16)) where an individual hole-shift is applied.

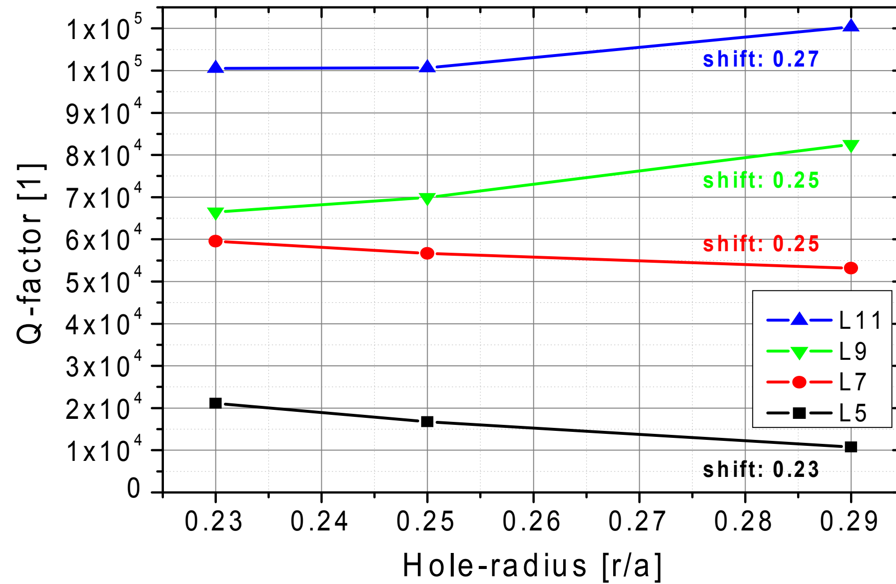

Figure 3.15 Q-factor vs. the hole-radius for Ln-type line-defect cavities cavities on 500 nm thick oxide. The period is 280 nm and the fine-tuned hole-parameters are indicated next to the curves.

3.3.1.2 Line-defect Hetero-structure Cavities

In terms of confinement, the line-defect cavities differ from the Ln-type cavities by the introduction of a modification along the removed row of holes, as already shown with some examples in chapter 4 "Dispersion Adapted Cavity". Here, however, we only investigate the properties of the hetero-structure cavity consisting of two different periods, as shown in the inset of Figure 3.16. Again, the mode is created in the central guiding region with period a_1 and decays in the mirrors with period a_2, where a_1 mainly determines the resonant wavelength of this single mode cavity. Therefore, in first simulations we determined a_1 to be 270 nm for a resonant wavelength around 1200 nm, when r/a = 0.25. Next, a_2 needs to be optimised because a too high value does not completely cut-off the mode in the mirror region and a too low value might disturb the mode profile, leading to increased leakage. In order to cut-down on the number of simulations, we already used a 500 nm thick oxide. As a result of the optimisation, a value of 264 nm for a_2 was found to give the highest Q-factor within the 2 nm scanning grid used (Figure 3.16). Values that are 2 nm lower or higher than 264 nm result in lower Q-factor and also higher values having a more dramatic effect on the Q-factor. These simulations were performed with a

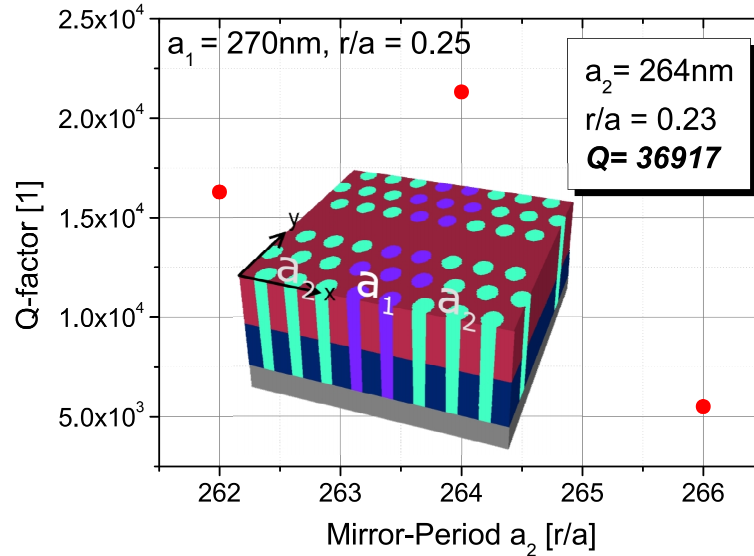

Figure 3.16 Q-factor optimisation of a hetero-structure cavity with two periods: a_1 and a_2. Inset shows the cavity as a line-defect with modification via the change of period. Scanning a_2 in 2 nm steps gives the maximum Q-factor at 264 nm with a_1 = 270 nm for r/a = 0.25. Keeping a_1 and a_2 constant and reducing r/a to 0.23 result in a Q-factor of 36917.

hole-radius of r/a = 0.25 and a reduction to r/a = 0.23, where the optimum value for a_2, leads to a maximum Q-factor of about 37.000. On a percentage basis, this is a stronger increase than for the previous Ln-type cavities and a main characteristic of a line-defect cavity [Song05], [Kuramochi06]. A Q-factor of 37.000 is a reasonable value and can be increased by reducing the hole-radius even further or using more than two periods. We do not want to introduce further periods, however, because of fabrication tolerances. Already with two periods, the difference between both periods is only 6nm and a third period will roughly halve this value, getting closer to fabrication limitation because our GaAs process is less mature than that in Silicon.

We have studied different types of cavities and their properties are summarised in Table 3.2. All Q-factors are above 10.000 and increase with the number of removed holes. A similar trend also applies to the mode volume. The distance to the next higher-order mode is labelled here as the free-spectral range FSR and is inversely proportional to the volume. This is where the advantage of the HS lies, while the Q-

Table 3.2 Properties overview of cavities with 500 nm thick bottom oxide and r/a = 0.25

Cavity	Q-factor	Volume	FSR
L5	16800	1.4 $(\lambda/n)^3$	23 nm
L7	56700	1.9 $(\lambda/n)^3$	12 nm
L9	70000	2.1 $(\lambda/n)^3$	7 nm
L11	100700	2.8 $(\lambda/n)^3$	5 nm
HS	21300	1.9 $(\lambda/n)^3$	>100 nm

Adapted Cavity" we will present a newly developed type of cavity and compare it to these properties. For the next section, we use an optimised L7 cavity on oxide with a Q-factor of about 57.000. This cavity as it is a good representative, because it has a high Q-factor and the mode profile is similar to those of the others cavities.

3.3.2 Loss and Gain Evaluation

The theoretical Q-factor is the upper limit that will not be reached, due to various types of losses such as scattering and absorption of QDs, doping of transport layers, mode interaction with the metal-contact, and the fabrication process. Recalling Eq.3.11, we can expand Q_{pass} and Q_{abs} to reveal further contributing factors:

$$\frac{2\pi n_{eff}}{\lambda}\left(\frac{1}{Q_{theo}}+\frac{1}{Q_{fab}}+\frac{1}{Q_{contact}}+\frac{1}{Q_{doping}}\right)=\Gamma_g g_g \qquad \text{(Eq.3.12)}$$

where Q_{theo} is the theoretical Q-factor of the cavity, Q_{fab} is the Q-factor due to the fabrication of the cavity, $Q_{contact}$ is the Q-factor due to absorption in presence of the metal-contact, and Q_{doping} is the Q-factor due to absorption in presence of the doped transport layers. Since high values of several 10.000's were calculated for Q_{theo} ,we are now interested in $Q_{contact}$ and Q_{doping}. Their Q-factors will – for some configurations – be lower than Q_{theo} , but a reasonable way to determine their limit is by equating them with the fabrication Q-factor:

$$\frac{1}{Q_{fab}}=\frac{1}{Q_{contact}}+\frac{1}{Q_{doping}}\geq\frac{1}{10.000}. \qquad \text{(Eq.3.13)}$$

This is true under the assumption that the fabrication Q-factor will be much lower than the theoretical Q-factor. This depends on the fabrication process but we do not expect the fabrication Q-factor to exceed 10.000. Because of this reason, we set as our goal for the next simulations that $Q_{contact}$ and Q_{doping} do not drop below 10.000 for the following metal-contact configuration and the doping concentration of the transport layers.

3.3.2.1 $Q_{contact}$ for different Metal-contact Configurations

Gold as metal-contact has a real part refractive index below 1 and suits well on top of the cavity but strong optical absorption – high imaginary part – introduces high absorption loss, as in all metals. Therefore, we now have to investigate how close we can bring the metal-contact to the cavity before the Q-factor drops below 10.000. This is important because a short contact-cavity distance is preferable in terms of electrical properties.

It is the mode profile that is important because loss only occurs when the optical mode overlaps with the metal. Even if a 2D plot of the mode profile does not show

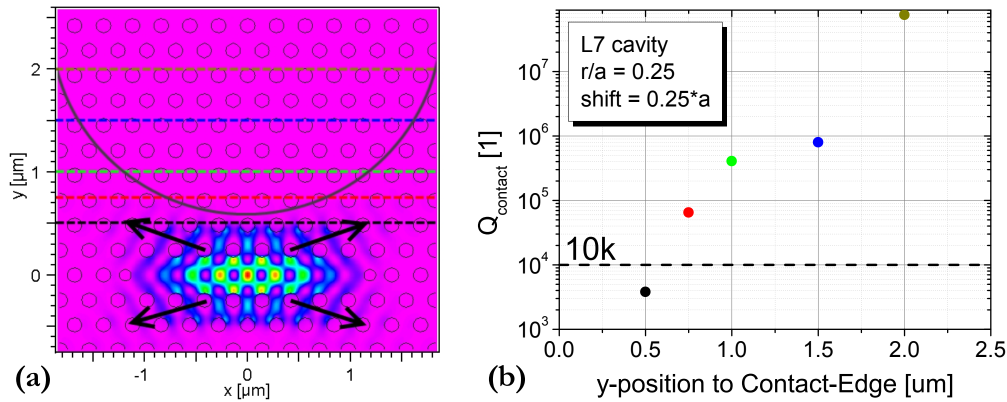

Figure 3.17 Study of the $Q_{contact}$ behaviour (b) depending on different metal-contact positions relative to the optical mode in (a). Electric energy-density distribution of a L7 cavity with indication of 5 Au-contact positions (a) with corresponding colour-coding for the extracted $Q_{contact}$ in (b). The dashed line in (b) indicates the Q_{fab} limit of 10.000. Note to (a): Four arrows show the direction of the mode where it strongly expands and the half-circle shows an example of a different type of contact shape which is not simulated here.

the full picture because this is again a 3D problem, we plot the electric energy-density distribution and show metal-contact position relative to the mode (Figure 3.17 a).

In order to simulate the influence of the metal-contact, a 100 nm thin Au-contact with a real refractive index of n_{real} = 0.38 and imaginary index of n_{imag} = 7.8 at 1.26 µm wavelength was chosen, because this is the main contributing material in contact for GaAs devices. $Q_{contact}$ is extracted by simulating the cavity with metal-contact in reference to the Q_{pass} of 57.000 using $1/Q_{contact} = 1/Q_{sim} – 1/Q_{pass}$. If the contact is sufficiently far away (> 1 µm) from the mode the Q-factor is orders of magnitude higher than Q_{pass} and the 10.000 limit (Figure 3.17 b). When, however, the contact visibly (< 1 µm) overlaps with the mode the Q-factor rapidly drops, exposing the strong absorptive nature of the metal-contact. From this point of view, it is clear that even the smallest overlap has to be avoided in order to maintain a high Q-factor, but it also shows that we can go as close as 0.75 µm to the centre of the mode enabling high current densities, as shown in the electrical section. Moreover, the Q-factor may also be maintained by curving the contact, thus avoiding the wings of the mode that strongly expand in about 30° directions (arrows in Figure 3.17 a). Similar contact configurations can be tested during fabrication.

3.3.2.2 Q_{doping} for different Doping Concentrations

After the determination of $Q_{contact}$ we now investigate the loss induced by free-carrier absorption of the doped transport layers. Recalling Eq.3.10, we can expect Q_{doping} to be low for high material absorption α_{abs} and high confinement factors Γ_{abs} of the doped layers. In Figure 3.18, a cross-section along the y-direction shows the electric energy-density distribution and the positions of the 100 nm thin transport layers within the 400 nm slab-thickness. The overlap of this particular slice shows that the main part of the field is located within the i-GaAs layer but there is also an overlap with the lossy transport layers. Simulations were performed with allocated material absorption coefficients $\alpha_{p/n}$ for the transport layer, using the doping concentrations from the electrical part that are 1.0x10^{17} cm^{-3}, 2.5x10^{17} cm^{-3} and 5.0x10^{17} cm^{-3}. The corresponding n-GaAs absorption coefficients were sourced from [Spitzer59]. For p-GaAs, however, no data covering the right wavelength and doping concentration was found, but a relationship between p-GaAs and n-GaAs

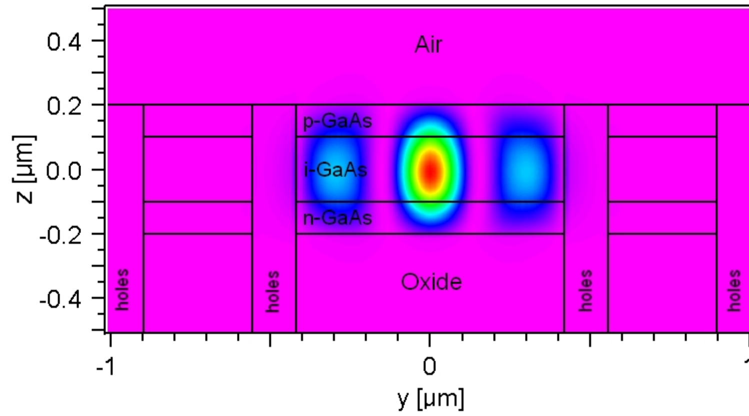

Figure 3.18 Slice through the slab showing the electric energy-density distribution and the layer structure with the 200 nm thick i-GaAs sandwiched between the 100 nm p-GaAs and the 100 nm n-GaAs layer. The slab is sitting on oxide and air-holes are perforated through all layers.

absorption coefficients of about a factor 4 was discovered and used in the following simulations. Q_{doping} for the three different doping sets was extracted in the same way as for the contacts, with the results shown in Table 3.3. The extracted Q-factor for the doping layers shows that the Q-factor is lower for the n-GaAs, due to lower absorption. Further, the combined Q-factor decreases with increased doping of a set, but is even with the highest doping higher then the limit of 10.000. This is due to the fact that the transport layers are sufficiently far away from the high field components, because of the 200 nm thick i-GaAs layer.

In summary, we can say that the losses introduced by the metal-contact are more critical that the losses due to the transport layer, but they stay above the Q-factor limit of 10.000 for certain metal-contact configurations.

Table 3.3 Overview of calculated Q_{doping} for different doping sets

Set	Individual Doping	Individual Absorption	Individual Q_{doping}	Combined Q_{doping}
low	p: 1.0×10^{17} cm^{-3}	2.8 cm^{-1}	370.000	300.000
	n: 1.0×10^{17} cm^{-3}	0.7 cm^{-1}	1.500.000	
med	p: 2.5×10^{17} cm^{-3}	6.0 cm^{-1}	170.000	140.000
	n: 2.5×10^{17} cm^{-3}	1.5 cm^{-1}	690.000	
high	p: 5.0×10^{17} cm^{-3}	12.0 cm^{-1}	86.000	69.000
	n: 5.0×10^{17} cm^{-3}	3.0 cm^{-1}	350.000	

3.3.2.3 Necessary Material Gain for Lasing

We have evaluated possible sources of loss and have shown that a high Q-factor can be maintained, and we will now investigate how high the material gain has to be in order to reach the threshold for different Q-factors according to:

$$\frac{2\pi n_{eff}}{\lambda}\frac{1}{Q_{total}\Gamma_g} = g_g \qquad \text{(Eq.3.14)}$$

where the material gain is inversely proportional to the Q_{total} and the gain confinement factor Γ_g. In order to do this we have to estimate the confinement factor Γ_g from FDTD simulations for each QD layer out of the maximum number of 5 layers, as shown in Figure 3.19. Within the 200 nm i-GaAs layer we placed a maximum number of 5 layers of QDs separated by i-GaAs barriers with a typical thickness of 30nm. We used a QD layer thickness of 4 nm, which corresponds to an average InAs QD height of 4 nm at some monolayers. FDTD simulations give a confinement factor for the 1st layer, the 2nd layer and the 3rd layer of 0.0153, 0.013, 0.0127, respectively. The confinement factor decreases when moving away from the centre, as expected due to lower field components. This factor, however, is the confinement factor for the whole layer as it would be the case for a quantum well, so that we also have to take the dot coverage into account. QDs can be of different shapes such as pyramids or half-circles so that their volume can be calculated easily.

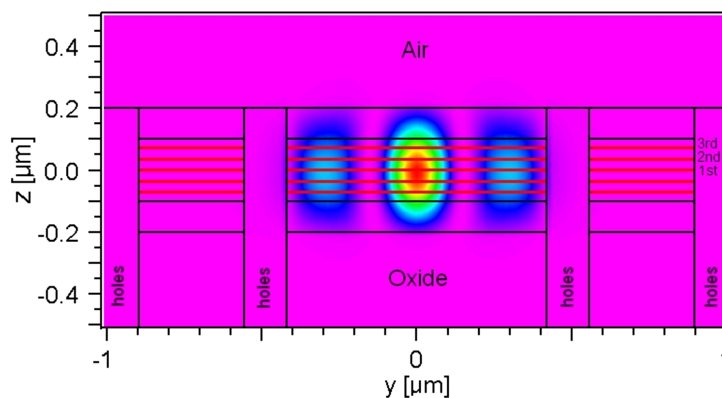

Figure 3.19 Slice through the slab showing the electric energy-density distribution and the positions of the maximum number of 5 layers of QDs (4 nm thin) separated by 30 nm i-GaAs barriers. The position of the QD layer is indicated by 1st, 2nd and 3rd row.

In reality, however, their shape is flat and rounded so that an expression for the dot coverage ε is usually given as [Rostami11]:

$$\varepsilon \approx N_{QD} \cdot A_{QD} \tag{Eq.3.15}$$

where N_{QD} is the dot density and A_{QD} is the base area of a single QD. Using 22 nm[1] as base length, for a square base, of a QD and 4.0×10^{10} cm^{-2} as the dot density we obtain ε = 0.194. After multiplication of ε with the confinement factor we obtain the total confinement factor of 3.0×10^{-3}, 2.5×10^{-3}, 2.4×10^{-3}. Now, we can use Eq.11 to estimate the material gain per QD layer we need to reach threshold for different Q-factors (Figure 3.20). Although this estimation depends on a high number of parameters that may vary in reality, it shows the need of stacking multiple QD and having a high-Q cavity. Assuming a realistic material gain for InAs QDs of several 1000's cm^{-1} at RT means that it is necessary to have at least 3 layers of QDs for a Q-factor of 5000. It is even better to use 5 layers of QDs in case the Q-factor for the fabrication is lower than 5000. We can compare the values from Figure 3.20 with the review of the PhC laser from section 2.2.2 "Ultralow-Threshold Electrically Pumped Quantum-Dot Photonic-Crystal Nanocavity Laser". There, lasing was achieved with 3 layers of QDs and a Q- factor of 1100. It is difficult to estimate

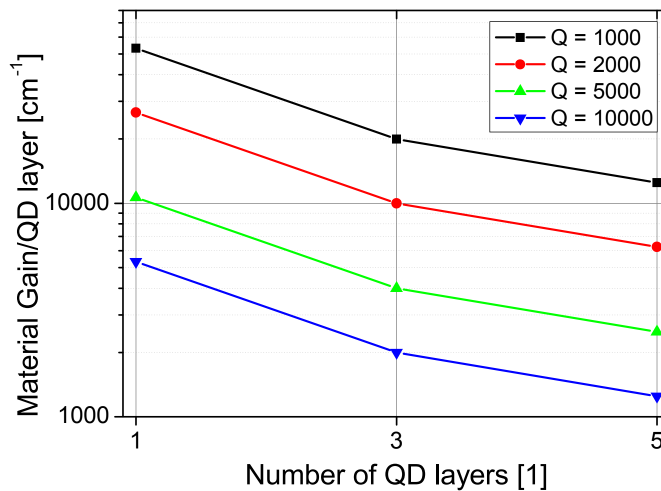

Figure 3.20 Material gain estimation after using Eq.14 for 1, 3 and 5 layers of QDs. The Q-factor needed for reaching the threshold is varied as a parameter.

[1] Numbers regarding the QD's are provided by our collaborators responsible for the wafer growth.

the size of their QDs, but we can calculate their vertical confinement factor, for the 220 nm thin slab, which is about a factor 2 higher than for a 400 nm thick slab. From this estimation, the material gain, needed for lasing, is 10.000 cm^{-1} for a Q-factor of 1000. This material gain is slightly higher than real values of the material gain, but it is in the region of our estimation. We can also check our values for the material gain by comparing them to the modal gain of typical stripe waveguide lasers. The modal gain is simply the multiplication of the material gain and the confinement factor of each QD layer. The corresponding modal gain for reaching the threshold, at a given Q-factor, is shown in Figure 3.22. The modal gain follows a similar trend as the material gain, so that a lower value for the modal gain per QD layer is needed when multiple layer are used or the Q-factor is high. In typical InAs QD lasers the modal gain[1] is in the order of 2-9 cm^{-1} per QD layer [Ledenstov00], [Smowton04]. From this point of view, 3 or 5 layers of QDs are needed to reach lasing for Q-factors higher than 5000.

We can conclude that lasing is possible when the current densities are sufficient to reach the stated material gain.

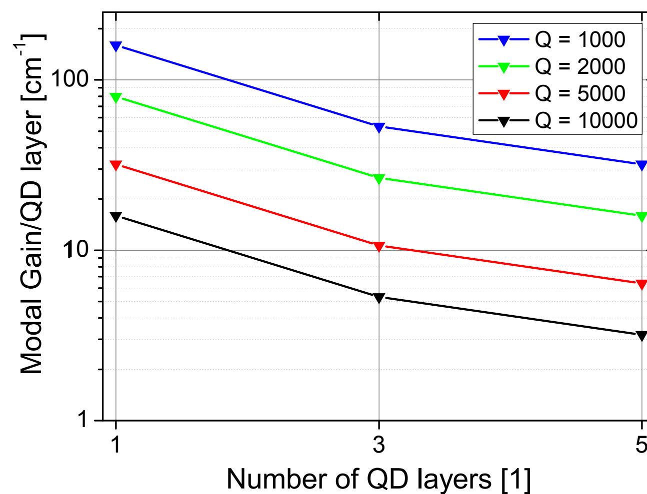

Figure 3.21 Modal gain per QD layer, in the case of a structure with 1, 3 or 5 layers, needed to reach the threshold for a given Q-factor of QDs.

[1] Please note that only the comparison of the material gain is fundamental. The modal gain can differ for device in the literature, and for our structure because of the difference in vertical mode confinement.

3.4 Thermal Properties

When designing real devices, their thermal behaviour must be taken into account especially for the type of nanoscale device operating at RT considered here. An increase in temperature for semiconductor gain materials results in a reduction of the overall efficiency; not only can the carriers escape from the QDs and their distribution thus broadens, but the non-radiative recombination also increases [Marko05b].[1] As a result, is well-known that the threshold current density J_{th} increases exponentially with the temperature T:

$$J_{th} \propto \exp(T) \quad \text{(Eq.3.16)}$$

In the worst case, high temperatures may inhibit lasing and have to be investigated.

The general heat conduction equation is typically expressed as follows:

$$Q = \nabla \cdot (-k\nabla T) \quad \text{(Eq.3.17)}$$

where Q [W/m^3] is the power density of the heat source, k the thermal conductivity of the material and T the local temperature. In electronic systems the heat source is typically provided by *Joule-heating*. Joule- or resistive-heating occurs when a current is passing through a resistive material and induces heat according to following relationship:

$$Q = J \cdot E = \frac{J^2}{\sigma} \quad \text{(Eq.3.18)}$$

Here, Q is the product of the current density J times the electric field E. Using Eq.3.5, we obtain that Q is equal to J^2 over the conductivity σ. Therefore, in order to keep the produced heat low, the current density has to be low and the conductivity has to be high.

We now investigate the temperature distribution using the 3D electro-thermal module in COMSOL. This simply calculates Q by sloving the electric conductions module first and followed by the temperature distribution according to Eq.3.17. In

[1] In addition, free-carrier absorption increases with temperature and the mobility of the semiconductor layer decreases with temperature.

addition to the already defined electrical material properties, we use typical values for the thermal conductivity of our material. Due to the low current densities, we do not expect the temperatures to increase strongly; therefore, we keep the electrical and the thermal conductivity temperature-independent. As far as the boundary conditions are concerned, we use thermal insulation on the mirror-symmetry plane and the top-surfaces, while the bottom-surface is connected to air and the other domains are kept at RT (293.15 K), as shown in Figure 3.22. We do not use air inside the holes or air on top of the structure because of restriction of computational resources. Furthermore, neither convection nor radiation is used because the conductivity of GaAs is high and conduction dominantes [Lu08]. To gain understanding of the heat distribution at the centre of the device, we plot the resistive heating (Figure 3.23 a) of the device presented in Figure 3.9 (d) – assuming a threshold current density of 67A/cm^2 at the centre of the cavity. Comparing the heat distribution with the current density distribution from Figure 3.9 (d), we find an unsurprising correlation of the two distributions. The heat distribution corresponds to the case with a current density of 67A/cm^1 and the resulting temperature distribution is shown in Figure 3.23 (b). The temperature is evenly distributed around the cavity region, with the highest value of 293.75 K recorded at the centre

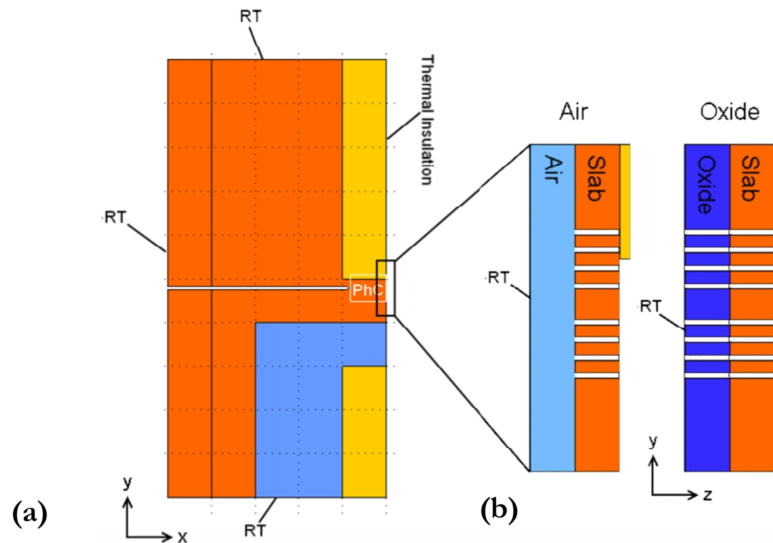

Figure 3.22 Thermal simulation with the thermal boundaries shown in top-view (a) and the cross-section along the PhC (b). At the mirror-plane and the top-surfaces, thermal insulation was chosen while the other boundaries are kept at RT. The cross-section shows the two cases of air and oxide under the slab.

of the cavity, as indicated by the green spot. The temperature increases only by about 1.5 K, which is very low and no problems associated with laser operation should occur in this case. In reality, however, the threshold current density increases because of non-radiative recombination, so that we have to increase the current density. Additionally, if we intend to use the device also above threshold we have to further increase the current density.

Using the reference point from Figure 3.23 (b), we plot the temperature over the current density in Figure 3.24. The modelled behaviour is of an exponential nature, as predicted by Eq.3.16. At a threshold current density of 67 A/cm², the temperature increases by only 1.5 K, but shoots up to 64 K at five times the value of 67 A/cm² (335 A/cm²). We chose a factor of five as a representative for additional non-recombination carrier loss and an operation beyond the threshold. High current densities can therefore cause problems with the device performance so that heat sinking is advisable. A low index material has to be used because of the optical confinement, so that oxides are the first choice of material for heat sinking in our device. Transformation of high-Al content AlGaAs into aluminium oxide (AlOx) is

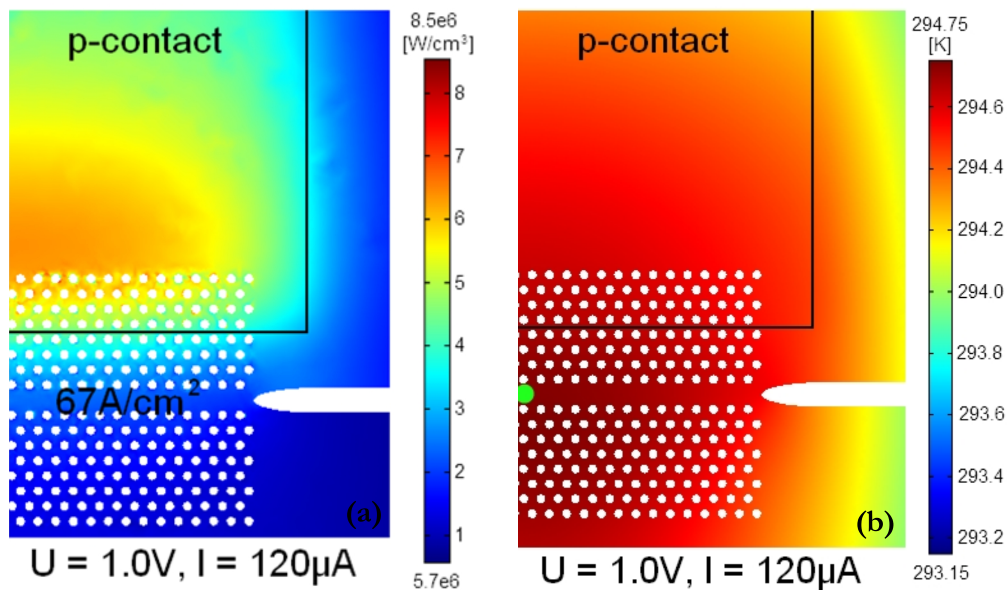

Figure 3.23 The heat distribution due to resistive heating is shown in (a) and the resulting temperature distribution for the air case in (b). The current density at the centre of the cavity is 67 A/cm² corresponding to the electrical simulations. The green spot in (b) is used as a reference point for further analysis.

an elegant way to provide such thermal as well as mechanical support of the slab. The transformation of AlGaAs into Oxide can be performed by wet-oxidation that creates Aluminium Oxide (AlOx) with a thermal conductivity of about 0.7 W/m.K [LeDu06], in contrast to the thermal conductivity of air with 0.025 W/m.K. We extended the thermal model by adding a 500 nm thick oxide layer below the slab. The oxide layer is perforated with air-holes, according to the optical simulations, and the bottom kept at RT. The temperatures of the membrane configuration are higher than for the oxide, because the slab is almost thermally insulated in vertical direction. The only to spread the heat is in lateral direction along the GaAs slab, which can be efficient. Using the oxide, on the other hand, adds a 28 times more efficient heat sink below the slab. This highly improves the heat removal out of the slab and causes the temperatures to fall. As mentioned before, heat spreading also occurs in lateral direction so that we now investigate the temperature inside the cavity depending on the hole-radius (Figure 3.25). In contrast to the electrical simulations (Figure 3.8), the curves are less steep because the heat source is outside the PhC cavity and therefore the heat flow, into the cavity, gets blocked when the hole-radius increases. When using a low current density of a few 10's of A/cm^2 (black squares), the increase in temperature is only in the range of a few Kelvin. In this case, no heat sinking through the oxide is necessary. Due to the exponential behaviour of the temperature with the current density, however, the temperature increases with the current density (red squares). In membrane configuration, the device experiences temperatures differences of more than 60 K, yet the oxide helps to keep the temperatures only around 20 K above RT. Therefore, the AlOx layer under the cavities keeps the temperatures low, even for high current density, and therefore it helps maintain lasing operation and improves the efficiency. Moreover, the AlOx also helps with reliability of the device due to the additional mechanical support.

We have now investigated the electrical, optical and thermal properties and we conclude the investigation by presenting the design wafer in the following section.

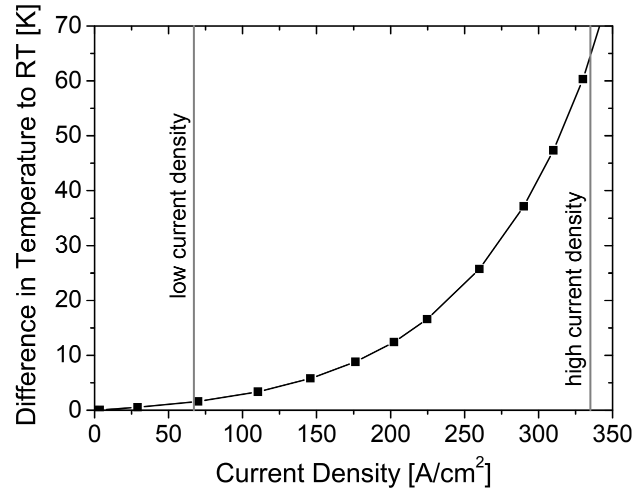

Figure 3.24 Temperature difference to RT vs. current density at the reference point. The marker "low current density" indicates the value of 67 A/cm² and the "high current density" marker indicates 5 times the value of the "low current density".

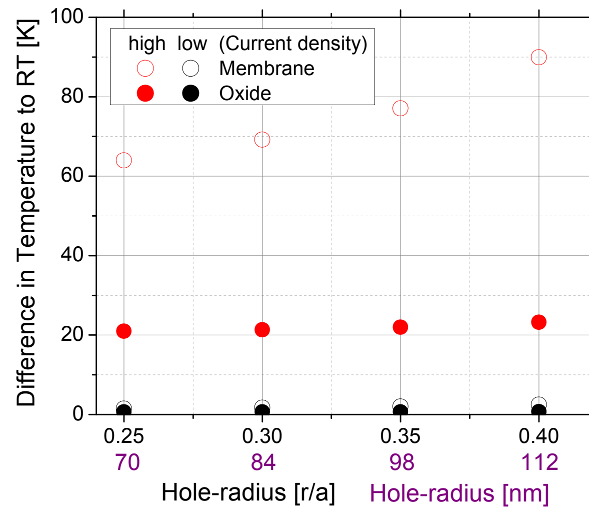

Figure 3.25 Temperature behaviour for membrane (open squares) and oxide (filled squares) cavity at low (67 A/cm², black squares) and high (335 A/cm², red squares) current densities. The oxide is 500 nm thick and perforated with air-holes. In addition, the hole-radius is varied.

3.5 Wafer Parameters

The wafers were grown by Molecular-Beam-Epitaxy (MBE) at the University of Sheffield according to our specifications.

The first wafer (Vn1315, Table 3.4) contains 3 layers of InAs QDs[1] sandwiched between 120 nm thick p- and n-doped layers resulting in a total slab thickness of 310 nm. The doping concentrations are in both cases 5x10^{17} cm^{-3} and do not introduce high amount of optical loss. Three layers of QDs are thought to be the lower limit for lasing, according to the gain evaluation in section 3.2.2 “Loss and Gain Evaluation”. Efficient pumping, assured through the highly doped layers, is necessary in order to obtain the highest gain possible. The slab is supported by a 450 nm thick AlGaAs layer with 94% of Aluminium. From the optical simulations, a 500 nm thick oxide layer did not affect the Q-factor of the PhC cavity to a great extent. The high amount of Al results in rapid oxidation even at RT, which needs precautions.

Table 3.4 Wafer Parameters: Vn1315

Layer	Thickness	Repeat	Doping
GaAs	120 nm	1	p – 5x10^{17} cm^{-3}
GaAs	20 nm	1	u.d.
InAs - QD	2.7 MLs	1	u.d.
GaAs	15 nm	1	u.d.
InAs - QD	2.7 MLs	1	u.d.
GaAs	15 nm	1	u.d.
InAs - QD	2.7 MLs	1	u.d.
GaAs	20 nm	1	u.d.
GaAs	120 nm	1	n – 5x10^{17} cm^{-3}
AlGaAs (Al = 94%)	450 nm	1	u.d.
GaAs buffer	300 nm	1	u.d.
GaAs Substrate	350 μm	1	u.d.

[1] Please note that the height of the barriers and the number of monolayers for each QD layer are chosen by the grow specialists according to their standards for high-quality QDs wafers.

Table 3.5 Wafer Parameters: Vn1807

Layer	Thickness	Repeat	Doping
GaAs	120 nm	1	p – 2.5×10^{17} cm^{-3}
GaAs	7.5 nm	5	u.d.
GaAs	9nm	5	u.d.
InGaAs (In = 15%)	1 nm	5	u.d.
InAs - QD	2.6 MLs	5	u.d.
InGaAs (In = 15%)	1 nm	5	u.d.
GaAs	17.5 nm	5	u.d.
GaAs	120 nm	1	n – 2.5×10^{17} cm^{-3}
AlGaAs (Al = 85%)	500 nm	1	u.d.
GaAs buffer	300 nm	1	u.d.
GaAs Substrate	350 μm	1	u.d.

The second wafer (Vn1807, Table 3.5) was designed to provide more gain and to further reduce possible optical absorption losses. A reduction in doping density to 2.5×10^{17} cm^{-3} was introduced to minimise possible absorption losses with a still acceptable device resistance of around 1000 Ω, according to the electrical simulations. The gain in this wafer was significantly improved, not only by using 5 layers instead of 3, but also with the use of a dot-in-a-well (DWELL) structure. A DWELL structure derives its name from the use of a capping layer around the QDs. This layer helps with the tuneability of the emission wavelength, with the capture of carriers and the increase in dot density. Therefore, higher gain is achieved in DWELL structures due to higher dot densities. The Al content of the AlGaAs was reduced here, because of higher stability at RT and a smoother AlGaAs top-surface that improves the QD quality.

Before turning to the electrical and optical characterisation of these wafers in 5 "Testing of Material Properties", we first present a newly developed PhC cavity design that is adapted to the dispersion characteristics of the PhC waveguide.

Chapter 4

Dispersion Adapted Cavity

4.1 Introduction

Usually, line-defects cavities are made by using arbitrary defects through which the mode is created and it then decays into the mirror region. Here, however, we show a different technique where the line-defect is created by forming the PhC, based on a Gaussian mode distribution. At first, we show typical line-defect cavities followed by the methodology of our cavity design. The following cavities are based and made in Silicon where the fabrication process is more mature than in GaAs and higher Q-factors can be achieved.

4.2 Types of Cavity Modifications

In section 3.2.1 "Intrinsic Q-factor for Different Types of Cavities" we have introduced the hetero-structure as an example of the line-defect cavities. In this section, we show different line-defect designs all based on the idea to have low-energy centre region surrounded by high-energy mirrors. Furthermore, the closer the resulting mode is to a Gaussian, the lower is the light leakage and the higher the Q-factor.

While discussing and simulating the HS cavity in earlier sections, we only used two different periods but an improvement in Q-factor is expected when multiple periods are employed. *Tanaka et al.* designed a multi hetero-structure cavity adapted to the Gaussian field profile by a similar method we later describe. The basic idea behind this method is to create a potential well which adapts to the field, which has a Gaussian profile. *Tanaka et al.* achieved this theoretically by changing the lattice constant, which is one way to achieve the desired confinement profile. Here, the

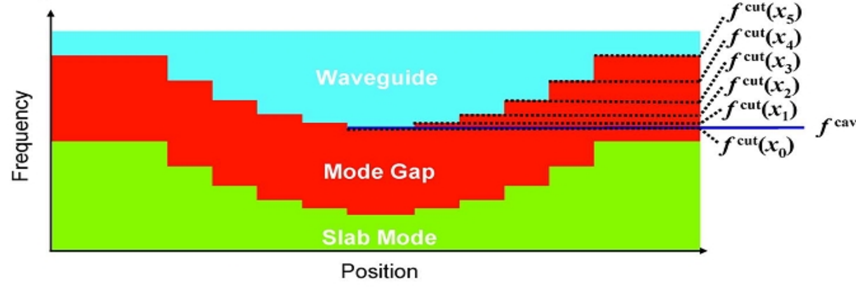

Figure 4.1 Potential well consisting of multiple sections with decreasing lattice constant and increasing cut-off frequency. [Tanaka08][5]

lattice constant, for each section, is chosen to have a higher cut-off frequency at the outer region than in the centre (Figure 4.1). This can be seen analogously to an energetic potential well, where the energy of a field is not sufficient to overcome the potential and is therefore confined in the centre. As a rule of thumb, we can say that in the centre the cavity mode has to sense more material than in the outer region. Having more material means a higher effective index, which derives from the dispersion relation ($n_{eff} = ck/\omega$). A higher effective index n_{eff} corresponds to a lower frequency ω. With this method, they demonstrated a theoretical Q-factor of about 1.000.000.000 [Tanaka08] and an impressive experimental Q-factor 1.000.000 for a glass-embedded cavity [Song11]. The values for the periods used for the multi hetero-structure cavity are shown in Table 4.1. The difference between two neighbour periods is small so that higher requirements on the fabrication are needed in order to obtain reproducible cavities. Moreover, these lattice shifts are for a

Table 4.1 Overview over calculated lattice constants from [Tanaka08]

Section	Lattice constant [nm]
1	420
2	419.2
3	417.1
4	413.4
5	409.1
6	403

W0.66 waveguide, because of easier calculation as stated in the publication. A further reason for choosing the W0.66 waveguide might be that for a W1 waveguide the difference in lattice constants is considerably smaller. This is due to the nature of the dispersion curve, which for a W0.66 has a much longer flat region near the band-edge as explained in the next sections. Nevertheless, this method has shown in a beautiful way how it is possible to acquire an almost perfect gentle confinement for a Gaussian mode.

Another way for creating a mode confinement is by changing the hole-radius for the whole section or just the first row of holes. It is sufficient to change only the first row of holes because they are near the high amplitudes of the field and interact stronger than the subsequent rows. Using the effective index rule, the centre needs to have smaller holes than the outer region. *Kwon et al.* [Kwon08] has shown this kind of confinement theoretically. The cavity consists of a centred tapered region which leads to the outer region (mirror region) as shown in Figure 4.2. A Q-factor of 30.000.000 for S5 and 20.000.000 for S3 were achieved theoretically. For the linear taper, the increment in radius is 4 nm/2.4 nm for the S3/S5 design, respectively.
A further ultra-high Q-factor cavity, where holes are shifted outwards, was designed and fabricated by Kuramochi et al. [Kuramochi06] shown in Figure 4.3. Using this

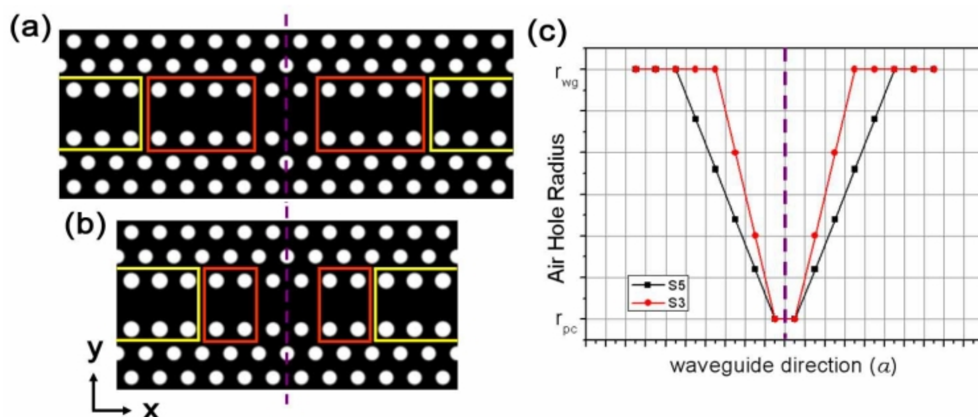

Figure 4.2 Cavity designs with tapered region (red boxes) and outer region (yellow boxes). Two different taper lengths S5 (a) and S3 (a) (4 holes and 2 holes respectively) are shown. Distribution of radii (c) in the tapered region with r_{pc} = 100 nm and r_{wg} = 112 nm. [Kwon08][6]

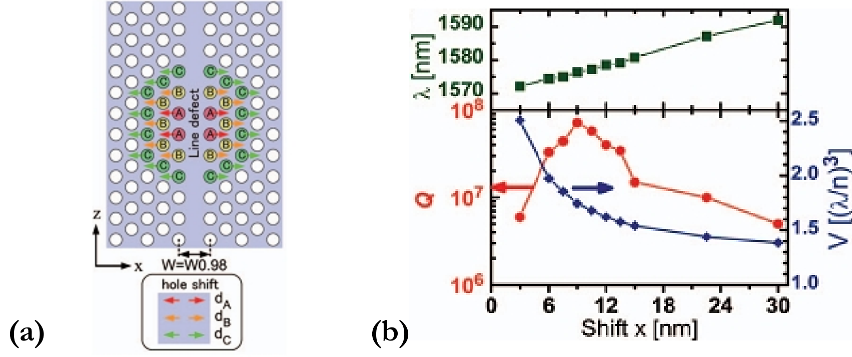

Figure 4.3 Top-view of cavity (a) created by shifting holes outwards in a W0.98 waveguide, where shift $d_A = x$, $d_B = 2x/3$ and $d_C = x/3$. Calculated Q-factors (b) values peaking at about 9 nm with decreasing mode volume. [Kuramochi06][7]

method, a record Q-factor values of 2.000.000 were experimentally demonstrated [Takahashi07]. Shifting the holes in an arbitrary way will create a cavity and scanning through the parameters will eventually reveal the maximum Q-factor. For example, the shifts for maximum Q-factor are 9 nm, 6 nm and 3 nm. These shifts require high precision electron-beam writing and fabrication i.e. a 5 nm position-error of the electron-beam will have a big influence on the cavity when using small hole-shifts. In addition to the hole-shifts, the waveguide width needs to be decreased, increasing the cut-off frequency and creating an additional barrier. The maximum theoretical Q-factor for this cavity is about 70.000.000 with an experimental value of about 2.000.000, the difference being caused by fabrication imperfections, as explained earlier. On the other hand, the Q-factor of the double hetero-structure cavity drops from 24.000.000 to 1.000.000 as well. Lower experimental values also result from fabrication imperfections like sidewall angle, variation in radii and material absorption [Asano06].

The presented ultra-high Q-factor cavities achieve mode confinements in a photonic-crystal waveguides by using different types of hole modifications – with the typical achievable Q-factor in the range of several ten's millions and experimentally of a 1-2 millions, and the main difference being the required accuracy and the reproducibility.

Our basic idea is to use hole-shifts for a non-arbitrary mode confinement, where we apply individual hole-shifts to adapt the dispersion curve for a Gaussian mode

envelope with the goal of achieving similar Q-factors as above, but with higher fault-tolerance.

4.3 Methodology of Confinement

In this section, the way for calculating the individual hole-shifts will be presented. Both, analytical and numerical methods are applied to obtain the shifts in contrast to [Tanaka08], where mostly analytical methods were used. Therefore, the combination of both methods allows us to be flexible in the sense of the type of waveguide and hole-modifications we want to apply.

Showing the final design of the cavity (Figure 4.4) at the beginning makes it easier to follow the steps needed to determine the cavity parameters. As we discussed in the previous section, shifting the holes outwards lowers the cut-off frequency and shifting them inwards increases it, creating a potential well. The individual hole-shifts are obtained by solving the master-equation (Eq.4.6), with a Gaussian field profile as a boundary condition.

In brief outline, we start with simulating of the dispersion curves – numerical part - using the MPB frequency-domain Eigensolver [MPB] that are then fitted and processed in the analytical part as shown in the flow chart in Figure 4.5. The dual

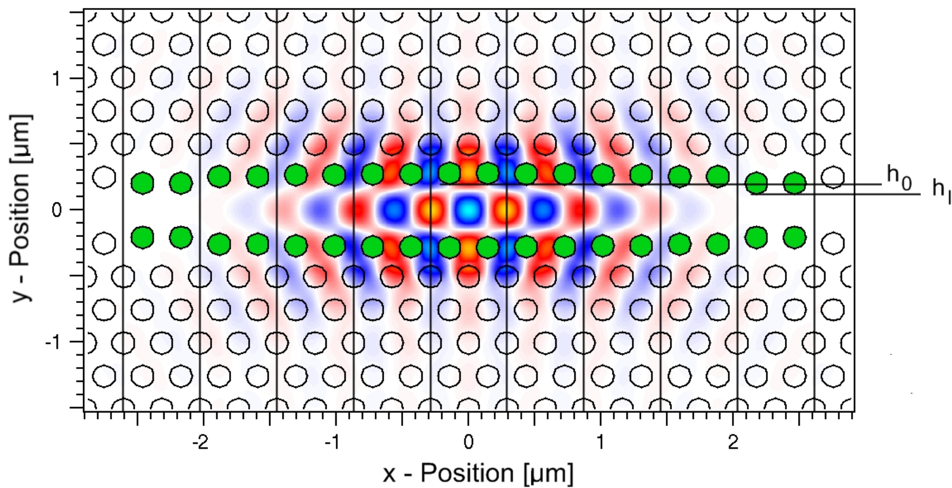

Figure 4.4 Top-view of a DA cavity with confined fundamental mode (E_z field). Hole-shifts starting from h_0 in the first section to h_l in the last section (5 section used here). The waveguide continues as a W1 after the last section.

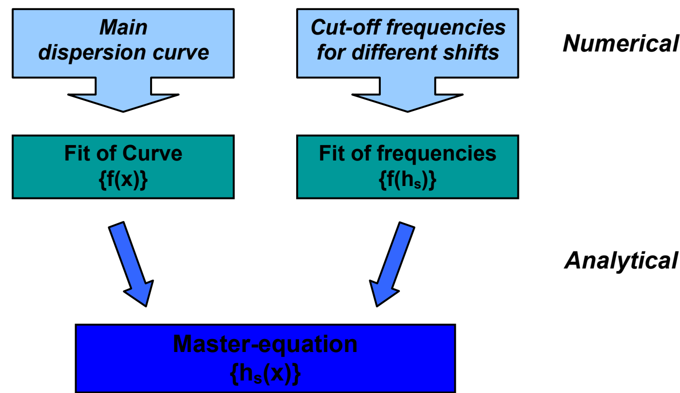

Figure 4.5 Dual-method using numerical simulations which are fed into the analytical part to result into the master-equation that is then used obtain the hole-shifts.

method (*numerical* and *analytical*) allows us to use every possible type of cavity modifications for our cavity, because we numerically investigate the frequency behaviour of the modification and then use it create a cavity. Since controlling the hole-position is more accurate in the e-beam lithography process than controlling the hole-size, shifting holes was chosen as the preferred method for achieving the desired dispersion relation.

4.3.1 Numerical Part: Dispersion Curves

Basically, knowing the dispersion curve allows us to set the frequency for each section depending on the value of the frequency at a certain k-point. One assumption, namely the invariance of the shape of the curve within all sections, is needed. This is perfectly true in the case of the multi hetero-structure because the changing the period only shifts curves due to scalability of the band-diagram. In our case, shifting the first row of holes slightly affects the shape of the band of interest, but, we neglect this.

The dispersion calculations were performed with MPB in three-dimensions for a supercell shown in Figure 4.6 (a). Removing the central holes at $y = 0$ results in a W1 photonic-crystal waveguide, which is the starting point for the calculations. At the band-edge, i.e. for $k = 0.5\ (2\pi/a)$, the W1 even mode has the lowest frequency with

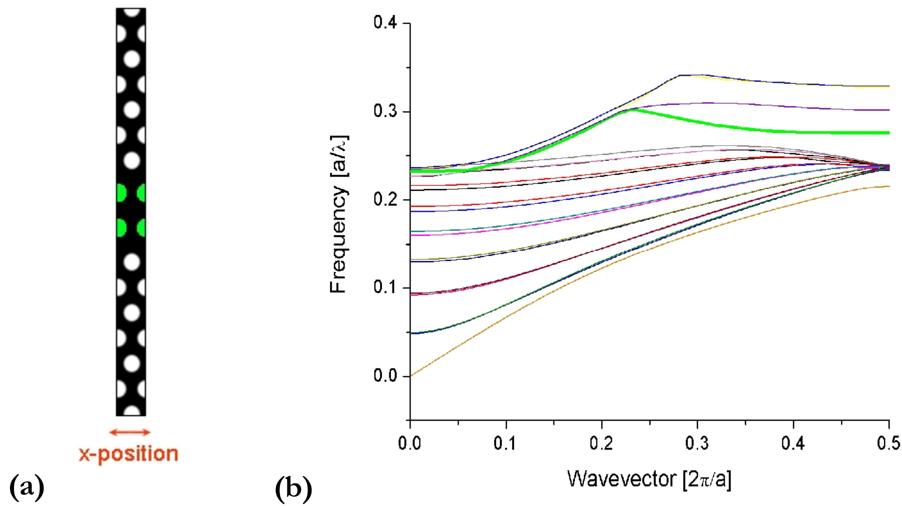

Figure 4.6 MPB band structure simulation using a supercell shown in (a) where the first row of holes (green) is shifted inwards or outwards. A typical band diagram shows the dielectric bands and the even band of interest, highlighted in green.

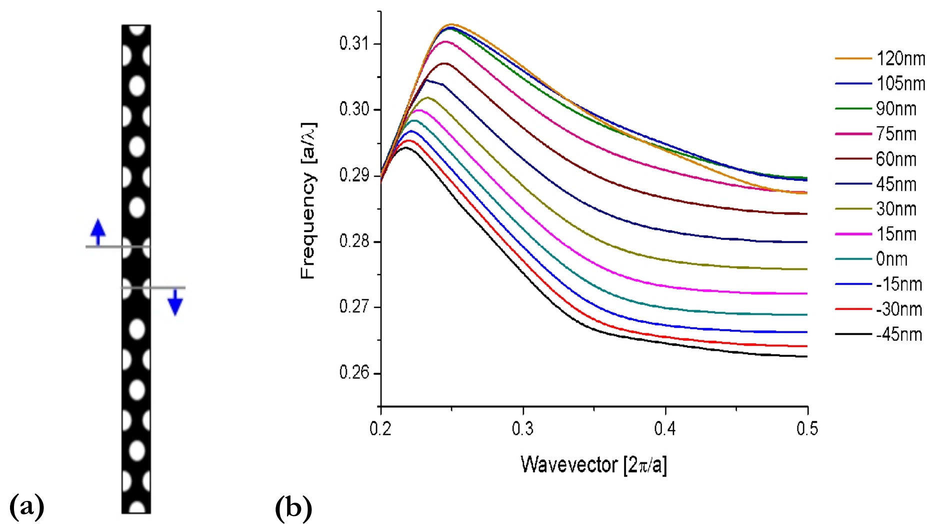

Figure 4.7 Dispersion curves (b) of defect-mode of interest at different first row hole-shifts (a). The positions of holes in (a) is corresponding to 120 nm and the direction of the arrows indicate the decrease of the value.

the highest density-of-states and therefore, the frequency of a cavity mode will lie close to the band-edge. Moving towards lower k values, the frequency slightly increases and bends up strongly after passing the anti-crossing point at around k ≈ 0.35. The anti-crossing point is determined by the interplay between the band-gap guided (higher k) and the index-guided (lower k) regions.

The main idea behind the confinement method is the creation of a potential well by piecewise adapting to the dispersion curve such that the resulting confined state has a Gaussian distribution. In the next step, the first row of holes is shifted and the dispersion curves are calculated (Figure 4.7).[1] Increasing the shift leads to a blue-shift of the mode. This means that by using sections with larger shifts a potential barrier for the mode can be created. Beside the shift, a deformation of the curve-shape occurs at extreme shifts (i.e. -45 nm, 75 nm-120 nm), due to coupling with lower or higher modes. Therefore, only modes between the extremes can be used, but this is sufficient considering the large span of frequencies. Comparing the curves, we see that the curves are similar in shape and the argument of invariance of curves is almost true. Now, a low-frequency dispersion curve needs to be picked that can be adapted to build the well – preferably higher than s = -45 nm – where in the analytical part this curve will be fitted. Plotting the frequencies from Figure 4.7 (at k = 0.5 (2π/a)) vs. the hole shift results in the second curve (Figure 4.8) we need. Here, the coupling with other close modes after Figure 4.6 (b) can be seen as saturation and occurs for large, positive shifts. This frequency-shift relationship enables us to use the correct hole-shift for each section, which will be analytically shown in the next section.

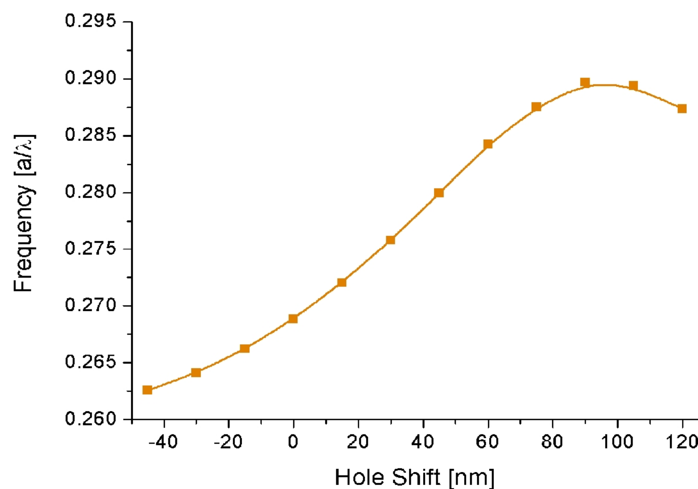

Figure 4.8 Frequency vs. hole-shift at k = 0.5 (2π/a) taken from Figure 4.7.

[1] Note that the reason for shifting was explained in earlier sections.

4.3.2 Analytical Part: Master-Equation

As shown in Figure 4.5, the fit of the main dispersion curve provides

1. $f(x)$, with x as the x-position of the cavity
2. $f(h_s)$, with h_s as hole-shift.

Combining both expressions, in the form of $f(x) = f(h_s)$, results in the master-equation $h_s(x)$.

Fit of Dispersion Curve

Five polynomial terms are needed to fit the curve accurately. Due to symmetry, these terms are all even powers of k. Furthermore, it is not necessary to fit the entire curve, because we estimated that the saturation in Figure 4.8 at higher frequencies is caused by mode-coupling and will not be used. Therefore, fitting the curve in the range of frequencies corresponding to the hole-shift -45 nm to 75 nm is sufficient. The dispersion curve can be expressed in a polynomial form as follows:

$$f_{(k)} = f_{k=0.5} + a(k-0.5)^2 + b(k-0.5)^4 + c(k-0.5)^6 + d(k-0.5)^8 \quad \text{(Eq.4.1)}$$

where $f_{k=0.5}$ is the frequency at the band-edge and *a,b,c,d* are the fitting parameters. At this stage the variable is the wavevector *k* in k-space, which is an inverse of the position *x* in real space. So far we have only used the real part of the wavevector *k*, which can also be expressed as a complex wavevector $k = 0.2 + iq$ or $iq = k - 0.5$ [Tanaka08] with *q* being the imaginary part of the wavevector. Substituting the complex wavevector into Eq.4.1 gives the imaginary dispersion relation at k =0.5:

$$f_{(q)} = f_{k=0.5} + aq^2 + bq^4 + cq^6 + dq^8 \quad \text{(Eq.4.2)}$$

Setting the cavity modes to be of Gaussian profile in form of $exp(-Bx^2)$, where *B* represents a constant, we take the condition for *q* assuming the exponential field decay $exp(-qx)$ inside the mode-gap region. As a result, *q* can be expressed in terms of *x* through $q = Bx$. After substitution into Eq.4.2, the frequency of the mode is expressed in terms of real space rather than k-space

$$f_{(x)} = f_{k=0.5} + a(Bx)^2 + b(Bx)^4 + c(Bx)^6 + d(Bx)^8 \qquad \text{(Eq.4.3)}$$

where the B parameter can be seen as the strength of the cavity mode confinement. At this point, the equation can be used to create the potential well, but if we consider shifting discrete holes, an expression depending on the hole-number in x-direction would be more suitable. Looking back at Figure 4.4, the number of shifted holes (in green) in each section, which are divided by vertical lines, is two. As we can choose how many holes should be in one section it turns out that two is a good compromise, where one hole does not have a big impact and a section with three holes might be too large in respect to the relatively small mode profile. Expressing the position through a discrete number, we can use $x_n = a_{PhC}(2n + 0.5)$, with n as the section-number and a_{PhC} as the lattice constant starting with $n = 1$ with the first section after the central section. After these calculations, the first part of the master-equation can be written as

$$\begin{aligned} f_{(n)} = f_{k=0.5} &+ a(a_{PhC}B(2n+0.5))^2 + b(a_{PhC}B(2n+0.5))^4 \\ &+ c(a_{PhC}B(2n+0.5))^6 + d(a_{PhC}B(2n+0.5))^8 \end{aligned} \qquad \text{(Eq.4.4)}$$

Now, the frequency of the mode – assuming a Gaussian profile – can be calculated for each section individually. The desired shape of the potential well is then determines the hole shift in each section.

Fit of Cut-Off Frequencies

Fitting the frequency vs. hole-shift relationship between the extremes, requires a quadratic polynomial equation. Keeping it as simple as possible avoids creating an unnecessary high number of solutions for the future master-equation.

$$f_{(h_S)} = f_{h_S 0} + \alpha h_S + \beta {h_S}^2 \qquad \text{(Eq.4.5)}$$

This equation gives the second part of the master-equation with the frequency following the hole-shift h_s and an offset f_{hs0} with zero hole-shift.

Master-equation

Finally, Eq.4.4 gives the frequency of the mode for each section and Eq.4.5 the frequency for the applied hole-shift. Combining Eq.1.4 with Eq.1.5 in form of:

$$f_{h_S 0} + \alpha h_S + \beta h_S^{\ 2} = f_{k=0.5} + a(a_{PhC}B(2n+0.5))^2 + b(a_{PhC}B(2n+0.5))^4 + c(a_{PhC}B(2n+0.5))^6 + d(a_{PhC}B(2n+0.5))^8 \quad \text{(Eq.4.6)}$$

results in two solutions for h_S. In this form, the hole-shift can be calculated for each section individually, only depending on fitting- and design-parameters. It is clear that the lower the number of polynomial terms on the left hand side, the lower the number of solutions that needs to be calculates. On the other hand, it is not important how many terms are used to fit the dispersion curve, because *Mathematica* is used as a mathematical tool to deal with these equations, and is easily able to cope with this level of complexity. One should try to fit the curve accurately by using a sufficient number of terms while trying to keep the equation as short as possible to avoid mistakes.

The last section has shown a methodical way of calculating the hole-shift required for creating a Gaussian mode envelope in a photonic-crystal cavity. In the next section, 3D Finite-Difference Time-Domain (FDTD) simulations are performed on the base of different parameter-optimisations to investigate the predicted properties, as well as the Q-factor, the mode volume and the resonant-wavelength.

4.4 Parameter Optimisation Scan

As shown in Figure 4.4, there are several parameters that influence the behaviour of the cavity and that must be analysed, especially because they are required as input-conditions for the hole-shift calculations as well. These parameters are:

- hole-radius, r or r/a
- number of sections, N_{Sec}
- first hole-shift, h_0
- last hole-shift, h_l

A 4-dimensional optimisation process of all possible parameter combinations would require a large amount of simulations and is not absolutely necessary. Therefore, a scan of each parameter, while keeping the others constant, was performed and analysed.

Since this cavity has the ability to use relatively big hole-shifts in the range of 10's of nanometers rather than individual nanometers, larger values for the initial condition are used. Moreover, this will limit the range of values to a reasonable number and reduces the number of simulations. As mentioned in the master-equation section, two solutions for the hole-shifts are possible. But, only one solution approaches the last hole-shift continuously, whereas the other solution goes beyond the value of the last hole-shift and then returns back to it. We therefore ignore the last solution.

Hole-radius

Unlike the other parameters shown above, the hole-radius is already set in the dispersion curve simulations. There are several known effects of the hole radius on the band diagram, such as narrowing and blue-shifting of the band-gap. The blue-shift of the resonant wavelength can be seen in Figure 4.9, top panel.

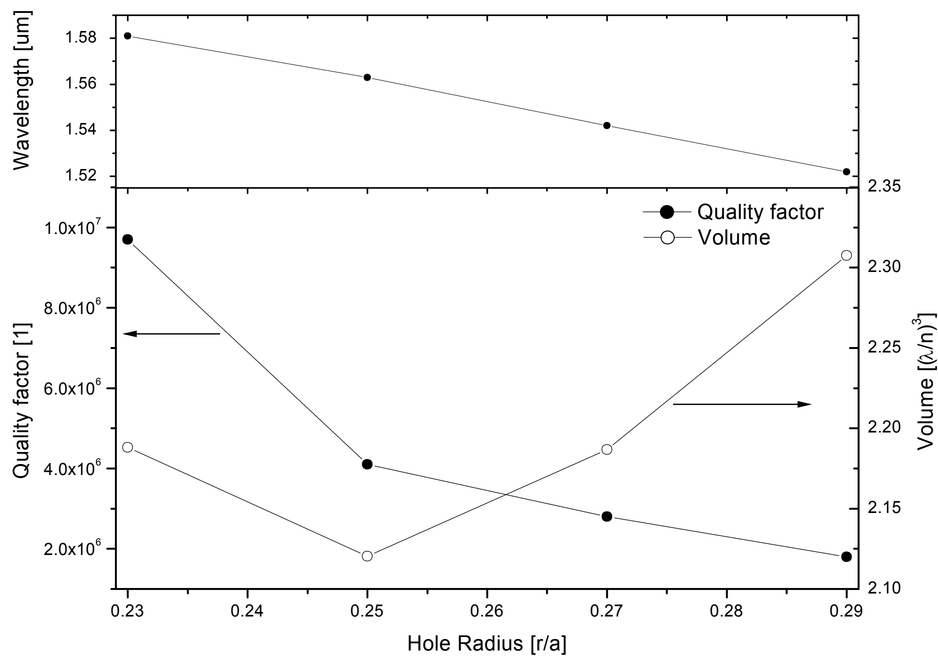

Figure 4.9 Hole-radius scan with fixed parameters: a = 400nm, h_0 = 40 nm, h_l = 60 nm, N_{Sec} = 7

The mode-volume decreases with decreasing hole-radius until about r ~ 0.25, where it begins to increase again. An explanation is the shrinkage of the band-gap in certain direction, so that the mode expands and its volume increase after the initial decrease. An opposite trend to the mode volume behaviour is seen in the Q-factor, which increases non-linearly with decreasing hole-radius[1]. This effect was also reported in other waveguide-cavities, but no explanation was given. It is not clear where this relationship comes from, because the band-gap is decreasing. A reasonable explanation can be found by remembering that high Q-factors in cavities are achieved by minimising the mode-overlap with the surfaces of the holes. In that sense, smaller holes interact less with the mode due to their smaller dimensions and a decreased surface-area that might result in a high Q-factor. Small holes have advantages against bigger holes so that r/a = 0.25 is used for the next scans.

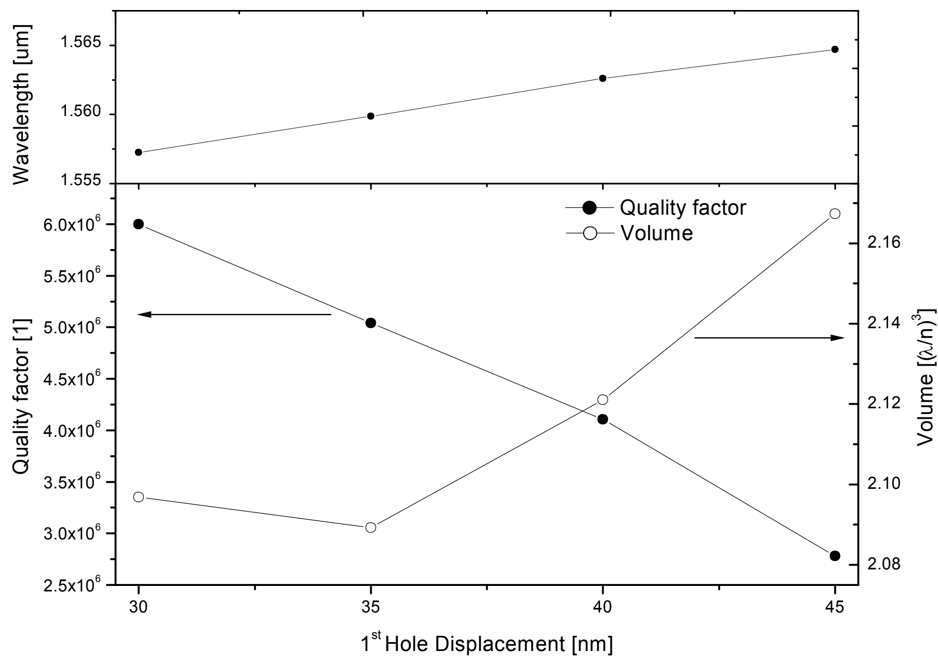

Figure 4.10 First hole displacement scan with fixed parameters: a = 400 nm, r=0.25, h_l = 60 nm, N_{Sec} = 7

[1] Looking at the electrical current flow through the PhC where bigger holes reduce the volume of the material, available for current flow, therefore increasing the electrical resistance. Small holes also have advantages against bigger holes for the complete device.

First hole-displacement

Increasing the hole-shift in the first section leads to an increase in resonant wavelength (Figure 4.10) as expected by the confinement effect discussed previously. Concurrently with the wavelength, the mode volume increases due to mode spreading in lateral direction. This can be related to the increase of the wavelength and diverging from the band-gap into the continuum of Bloch-modes. Increasing the hole-shift mainly increases the volume as expected. The Q-factor decreases with increasing hole-shift, probably due to undesired hole-mode interaction. It could be also due to a different effect like lower coupling to higher bands as shown in Figure 4.8, where saturation of the frequency curve sets in when moving towards high values of hole shifts. Reducing the hole-shift even further below 30 nm will further increase the Q leading to values of the width-modulated line-defect cavity. A value of 40 nm for the first hole-shift will be used because it offers a good compromise between the Q-factor and the absolute value in nanometres.

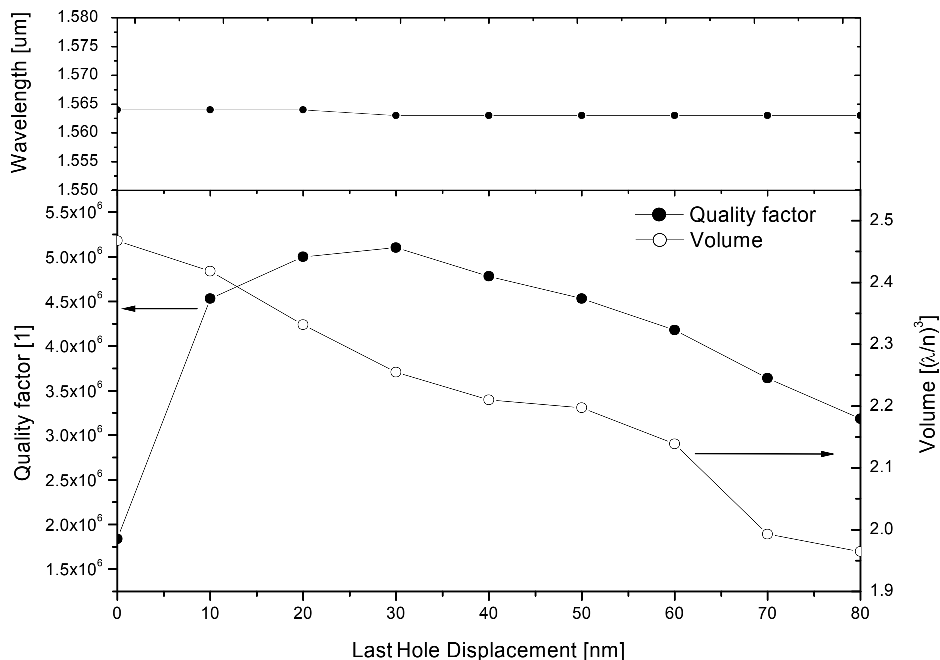

Figure 4.11 Last hole displacement scan with fixed parameters: a = 400nm, r = 0.25, h_0 = 40nm, N_{Sec} = 7

Last hole-displacement

Changing the last hole-shift almost does not affect the wavelength because the wavelength is set trough the first section (Figure 4.11). The volume has an inverse proportional relationship to the last hole-shift. This is probably due to the tighter mode confinement and lower in-plane leakage if larger shift are used. Similar to the volume behaviour, the Q-factor decreases with increasing hole shift, except hole shifts of a couple of 10's nanometres. In that range, the Q-factor increases dramatically before reaching a plateau and decreasing slowly. This can be explained by the fact that the last hole-shift determines the height of the potential well as shown in Figure 4.1 and a minimum shift is needed to avoid the field leaking through the mirrors. Further increase of the hole-shift will increase the hole-mode interaction, therefore disturb the Gaussian profile and introduce more Fourier components in the leaky out-of-plane region. As mentioned in the previous section, about 60 nm of last hole-shift gives a good compromise between Q-factor and the absolute value in nanometres.

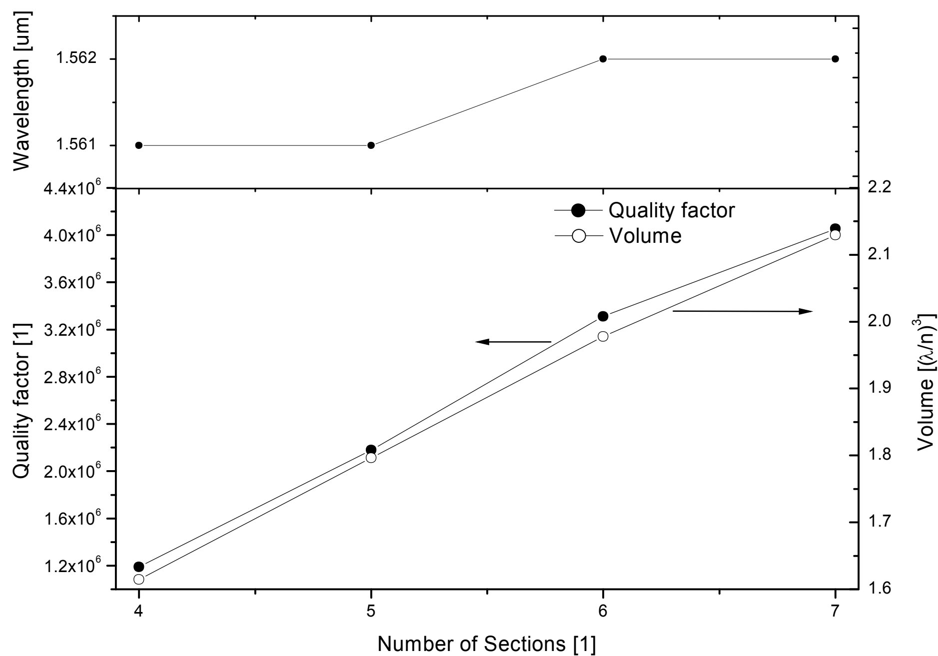

Figure 4.12 Number of sections scan with fixed parameters: a = 400 nm, r = 0.25, h_0 = 40 nm, h_l = 60 nm

Number of sections

Increasing the number of sections increases the size of the cavity and therefore increase the resonant wavelength, however, the increase in wavelength is smaller than expected (Figure 4.12).

A similar proportional relationship between the Q-factor/volume and the number of the sections is observed. Probably the Q-factor follows the change in volume and not the other way round. A low number of sections reduces the size of the cavity and increases the hole-mode interaction at the outer sections, which introduces out-of-plane loss. There might be already a general limitation in Q-factor setting in before other effects can affect the Q-factor. This might also be the reason why this cavity does not reach 100's million of Q-factor in this configuration, although pushing the parameters even further will show these theoretical values.
These simulations show that a Q-factor of several millions can be achieved by using larger hole-shifts than those used by other gentle confinement cavities. Next, the experimental Q-factors of DA cavities fabricated in Si are investigated.

4.5 Experimental Q-factors of DA Cavities in Silicon

The simulated curves are completed for the case of Silicon with a target wavelength of 1550 nm. Si is used because of the reliability in fabrication and ability to measure the cavities.
The cavities are made in a Silicon-On-Isolator (SOI) wafer with a 220 nm thick Si layer. In the first step, the electron-beam sensitive ZEP-520A by ZEON Cooperation is spun at the SOI cleaned and cleaved sample with following pre-bake. The PhC holes are exposed by our 30 kV electron-beam writer ZEISS GEMINI 1530/RAITH ELPHY system and developed in Xylene. After the development, the resist inside the hole is removed and ready for dry-etching. Dry-etching is performed within a parallel plate reactive-ion-etcher with SF_6 and CHF_3

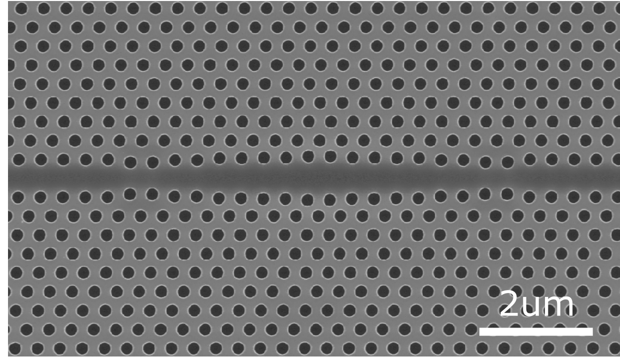

Figure 4.13 Top view of DA cavity fabricated in Si with a period of a = 400 nm and r/a = 0.25. The typical mouth-shape comes from the applied hole-shifts. Here the number of sections is 5 with these individual hole-shifts: h_0 = 40 nm, h_1 = 32 nm, h_2 = 21 nm, h_3 = -6nm and h_4 = -60 nm.

chemistry. Following the dry-etch, the holes are fully transferred into the Si slab reaching the silicon-dioxide. In the last step, the oxide is removed in liquid hydrofluoric acid (HF) to suspend the membrane. The cavity feature is the visible defect region (Figure 4.13) easily recognised by the relatively large shifts of the central holes.

Characterising cavities in Si, where no active medium is available, needs a special method to separate the cavity resonance from the pump beam resulting in a low signal-to-noise ratio. Polarisation is used here as a tool to separate those and dramatically increase the signal-to-noise ratio. Measurements on the cavities are performed by *resonant scattering* (RS) setup by collaborators at the University of Pavia in Italy [Galli09]. This technique has the other big advantage that it does not require access waveguides to the cavity as it is pumped from the top (Figure 4.14). Here, the pump beam is linearly x-polarised and focused on the sample while scanning through the spectrum. Off-resonance, the reflected beam is rejected by the analyser. If the wavelength is on resonance with the cavity, however, the polarisation component of the pump beam that is aligned with the cavity can couple into the cavity and excite the resonance (in xy direction). Equally, the light radiating from the cavity now has a y-component that can pass the analyser and gets detected. The strength of the signal depends on the coupling efficiency, in other words, how much light gets coupled into the cavity and back into the objective. This depends on the far-field distribution of the cavity mode and the numerical aperture of the objective

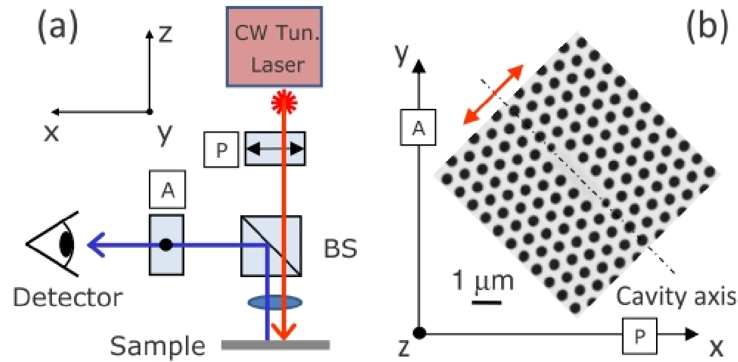

Figure 4.14 Resonant-scattering setup (a) used to characterise the fabricated cavities. The pump beam is linearly polarised (P) and focused on the sample. The beam-splitter (BS) deflects the out-coming beam through an analyser (A) on a detector. The L3 cavity (b) (for illustration purpose) is 45° rotated in respect to the polarisation of the polariser (P) and analyser (A). The red arrow indicates the polarisation of the cavity. [Galli09][8]

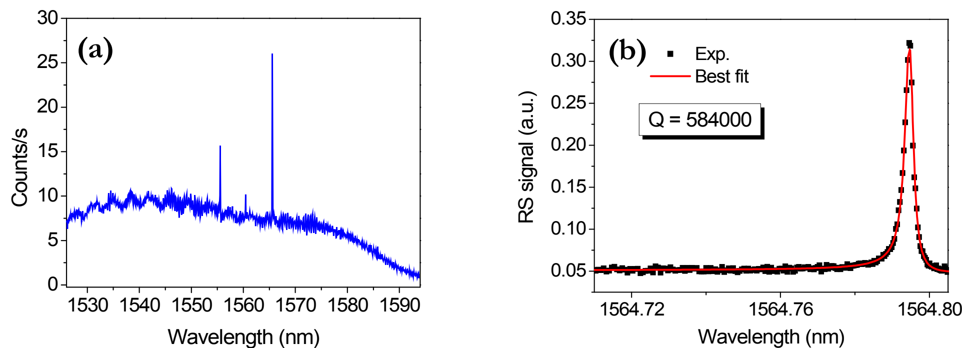

Figure 4.15 Characterisation of DA cavity with a = 400 nm, r/a = 0.25, h_0 = 40 nm and h_l = 0 nm. Spectrum (a) acquired by illumination with broad-band source and scanning with a monochramator. The strong peak at the highest wavelengths is the fundamental mode followed by higher order mode at shorter wavelengths. RS method (b) used to resolve the fundamental peak by scanning a narrow linewidth laser peak trough the wavelength range of interest.

used, which focuses the beam onto the sample. Naturally, this detection method presents a challenge, as the cavities are designed for ultra-high Q-factor operation by reducing leaky out-of-plane components, thus minimizing the collection signal. Hence, the resonant scattering method is essential due to its high signal–to-noise ratio. In the first step of a measurement, a broad-band source illuminates the cavity and a monochromator is used to acquire a broad spectrum as shown in Figure 4.15

(a). Several peaks appear in the spectrum with the fundamental mode at the highest wavelength, which is expected from a relatively long cavity. Resolving the fundamental peak using a narrow linewidth laser beam gives a Q-factor of about 580.000. This is close to the resolution limit of the setup (approx. 700.000). Measurements of cavities with different first hole-shifts, last hole shifts and different numbers of sections always give Q-factors between 500.000 – 600.000 and do not exhibit the behaviour as expected from 4.3 “Parameter Optimisation Scan”, which is likely due to the fact that fabrication imperfections set an upper limit on the measurable Q-factor. This limitation can be described by adding a corresponding Q factor into the equation (Eq.4.7):

$$\frac{1}{Q_{real}} = \frac{1}{Q_{3D_sim}} + \frac{1}{Q_{fab}} \qquad \text{(Eq.4.7)}$$

Here, the real Q-factor (Q_{real}) is determined by the simulated Q-factor (Q_{3D_sim}) using a 3D simulation and a fabrication Q-factor (Q_{fab}), which takes “reality” into account. We see that Q_{real} is dominated by the lowest Q-factor on the right hand side, which is Q_{fab}. Therefore, no strong dependence of the Q_{3D_sim} can be seen unless Q_{fab} is improved. Q_{fab} does not only include disorder due to positioning errors and noise on the e-beam system but also roughness caused by dry-etching. Only the radius seems to have a sufficiently strong influence on Q_{real} as shown in Figure 4.9, where Q_{3D_sim} roughly doubles when reducing the radius from r/a = 0.29 to r/a = 0.25 with a Q-factor of 2.000.000 and 4.000.000 respectively. The measured Q-factor (Q_{real}) with r/a = 0.29 is about 200.000 - 300.000 whereas for r/a = 0.25 the Q-factor increases to 500.000 – 600.000. This can be due to the behaviour shown in Figure 4.9 or and a reduced Q_{fab} because of the increased hole-mode interaction of the bigger holes. This is confirmed by the calculation of Q_{fab} for the small (Q_{fab} = 571.000) and big (Q_{fab} = 220.000) holes, where Q_{fab} is higher for smaller holes. This also confirms that in order to have high Q-factor hole-mode interaction should be minimised.

In summary, the DA cavity offers an alternative to other gentle confinement cavities, by using larger hole-shifts. Larger hole-shifts might be useful in respect to disorder stability when using optical-lithography – where the basic step size is

increased to typically 5 nm – or when using GaAs at lower wavelengths where the period and the defect modifications are decreased even further.

Another advantage of this cavity design is the possibility of *functional mirrors* that can control properties such as mode shape and reflected phase. For example, the far-field of a PhC cavity is given by the Fourier Transform (FT) of the field, which means that by controlling the mode profile the far-field can be modified. This can be done by calculating the shifts for different specific mode profiles or changing the shifts individually. As a result, it should be possible to achieve directional emission or even static beam steering. The mode profile can then be calculated in a reverse engineering method from the requested far-field to determine the required hole-shifts.

Functional mirrors can even shape the spectral emission peak by introducing a bi-stable state so that the cavity field does not decay exponentially, which usually results in a Lorentzian peak. Modifying the reflected phase of the decaying field through arranging the hole-shift in a special way, one could achieve a more flat-top like peak.

Overall, the DA cavity uses a cavity design that is based on a systematic design approach, unlike most other cavities. Unfortunately, the fabrication limitations did not allow us to demonstrate the full potential of this design.

4.6 DA Cavity in GaAs

As a follow up of the defect cavities from chapter 3 "Design and Simulations of ePCL" we now present simulations on the DA cavities for GaAs. New simulations need to be performed because the slab thickness increased that can result in a change of the dispersion properties. In order to assure that the starting parameters for the GaAs DA cavity are correct are we have performed MPB simulations on a membraned 400 nm thick GaAs slab using a period of 270 nm and $r/a = 0.25$ (Figure 4.16). This diagram is similar to that in Si in terms of shape for the band of interest. As a next step, the cut-off frequencies at a wavevector of $k = 0.5$ $(2\pi/a)$ for different hole-shifts are determined and then Eq.4.6 is used to work out the individual hole-shifts for two selected cavities with $h_0 = 20$ nm (30 nm) and 7 sections shown in Table 4.2.

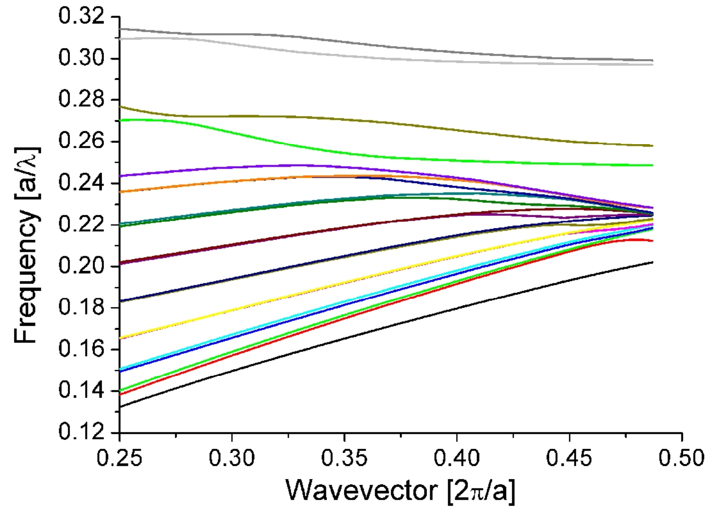

Figure 4.16 MPB band structure simulation with a 400 nm GaAs slab surrounded by air for a period of 270 nm, r/a=0.25 and a hole-shift of 30 nm. The band of interest is shown in green, similar to the case in Si (Figure 4.6).

Table 4.2 Hole-shifts in [nm] of two DA cavities for each of the 7 sections

Type	1	2	3	4	5	6	7
$h_0$20	20	19	16	12	4	-10	-30
$h_0$30	30	27	22	17	8	-8	-30

We only chose two different cavities, because it is known from the Si work that no major changes are likely to occur in the real Q-factor due to fabrication.

FDTD simulations were performed on the membraned GaAs cavities for different hole-radii with the results shown in Figure 4.17. The difference in Q-factor between both cavities is significant, but in both cases the Q-factor at r/a = 0.25 is higher than 1.000.000. For h_0 = 30 nm the Q-factor steadily increases with decreasing hole- radius, while the Q-factor for the h_0=20 nm cavity declines for values smaller

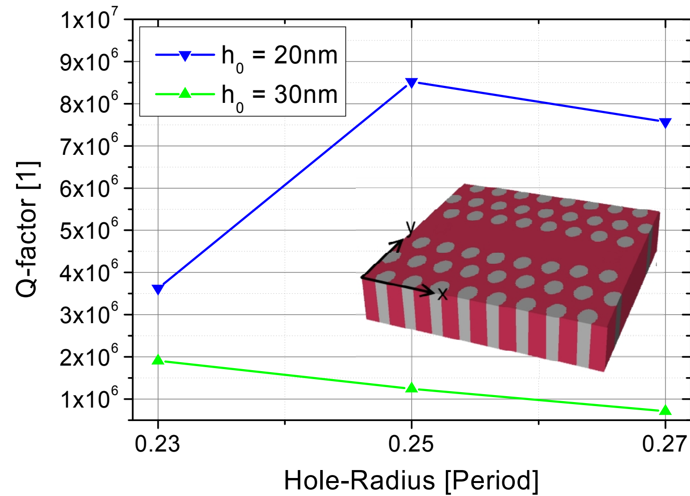

Figure 4.17 Q-factor vs. hole-radius for membraned DA cavities of type h_0=20 nm and h_0=30 nm with a period of 270 nm.

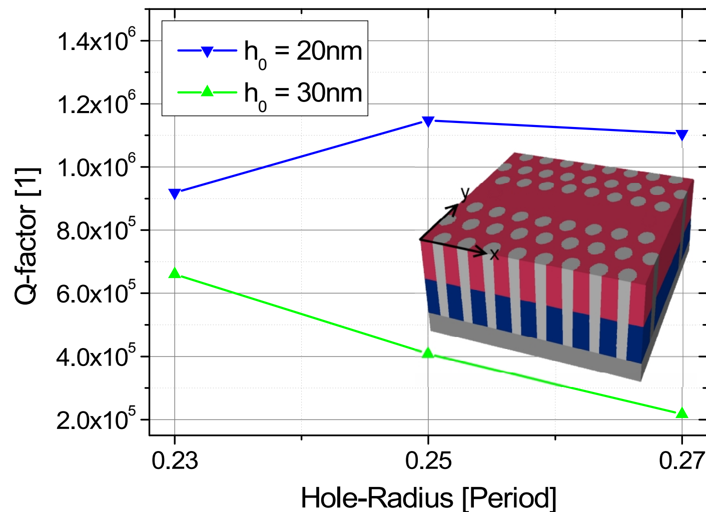

Figure 4.18 Q-factor vs. hole-radius for oxide DA cavities of type h_0 = 20 nm and h_0= 30 nm with a period of 270 nm. The oxide is 500 nm thick and the air-holes fully penetrate the oxide.

than r/a = 0.25, at this radius-step resolution we used. This can probably be attributed to fact that too small hole-shifts do not create a sufficient potential well so that the mode distribution is disturbed. Nevertheless, the values are high enough to justify placing the slab on oxide and investigating the Q-factor in a same way as for the defect-cavities in the design section 3.2.1 "Intrinsic Q-factors for Different Types of Cavities". The oxide is again 500 nm thick and perforated with air-holes. The resulting Q-factors are plotted in Figure 4.18 and exhibit a similar as for the membraned cavities, where the Q-factor for the h_0 = 30 nm cavity steadily increases

while the Q-factor of the $h_0 = 20$ nm cavity drops below r/a = 0.25. Their Q-factors are in the range of several 100k and even hit a remarkable value of more than $1x10^6$ for the $h_0 = 20$ nm type. Comparing these values to the defect cavities investigated in "3.2 Optical Properties", the DA cavities show an outstanding performance in terms of Q-factors, as highlighted in Table 4.3.

Table 4.3 Complete overview of cavities with 500 nm thick bottom oxide and r/a =0.25

Cavity	Q-factor	Volume	FSR
L5	16800	1.4 $(\lambda/n)^3$	23 nm
L7	56700	1.9 $(\lambda/n)^3$	12 nm
L9	70000	2.1 $(\lambda/n)^3$	7 nm
L11	100700	2.8 $(\lambda/n)^3$	5 nm
HS	21300	1.9 $(\lambda/n)^3$	>100 nm
DA ($h_0 = 20$ nm)	$1.14x10^6$	3.10 $(\lambda/n)^3$	6 nm
DA ($h_0 = 30$ nm)	408000	3.11 $(\lambda/n)^3$	8 nm

According to the table, the DA cavities can be seen as an improved version of the line-defect L11 cavity, where, for example, the $h_0 = 20$ nm type has a similar mode volume and FSR yet an order of magnitude higher Q-factor.

In summary, the DA cavities offer ultra-high Q-factors on 500 nm perforated oxide for 400 nm slab thickness that is due to gentle confinement and therefore a high reduction of leaky components.

Chapter 5

Testing of Material Properties

5.1 Introduction

Following up from section 3.5 "Wafer Parameters" where we have shown how the wafer properties were determined, we now test the wafer for *electrical* and *optical* properties. Different methods, applicable with our equipment, were used to confirm characteristics necessary for an ePCL which will be described in the next sections. In addition, we also test the fabrication steps while fabricating the devices.

5.2 Electrical properties

In the case of an injection laser, it is important to have efficient injection and transport of carriers into the active region. Doping concentrations were set according to the design chapter and have now to be confirmed qualitatively. Quantitative determination of the doping concentrations for the *n-GaAs* and *p-GaAs* transport layers are possible using transmission-line-measurements (TLM), but for a layered structure this measurement becomes a complex procedure. On the other hand, qualitative determination can be made by fabricating a device and testing it for diode characteristics. The two wafers that were grown externally will be examined in different ways. For Vn1315, we used a stripe design structure with lateral contacts and for Vn1807 the final ePCL structure with isolated lateral contacts.

5.2.1 Vn1315: Stripe-laser Electrical Device

At first, we present the fabrication procedure of this laterally injection device followed by the electrical measurements.

5.2.1.1 Fabrication of Stripe-laser Electrical Devices

As shown in Figure 2.2, the intrinsic QD region is sandwiched between a hole-conducting p-GaAs layer on top and an electron-conducting n-GaAs layer at the bottom. The fabrication starts[1] with a wet-etch of the unmasked region beside the waveguide, exposing the n-layer (Figure 5.1 a) using a modified mixture of phosphoric-acid, hydrogen-peroxide and deionised-water [Mori78]. This step is crucial because it has to stop within the 120 nm thick n-layer – starting at 200 nm depth – to enable carrier injection. We achieved this by keeping the etch conditions constant and performing short etches that we measured in terms of depth using a profilometer with nanometre resolution. Doing so, a run-to-run accuracy of only about 5nm is achieved[2]. It is important to do this step at the beginning of the process because there should be no metal present when the wet-etch is performed, otherwise the metal leads to a local increase of the etch rate, which can cut the conduction layer, as we will show later in this section. In order to prepare the sample

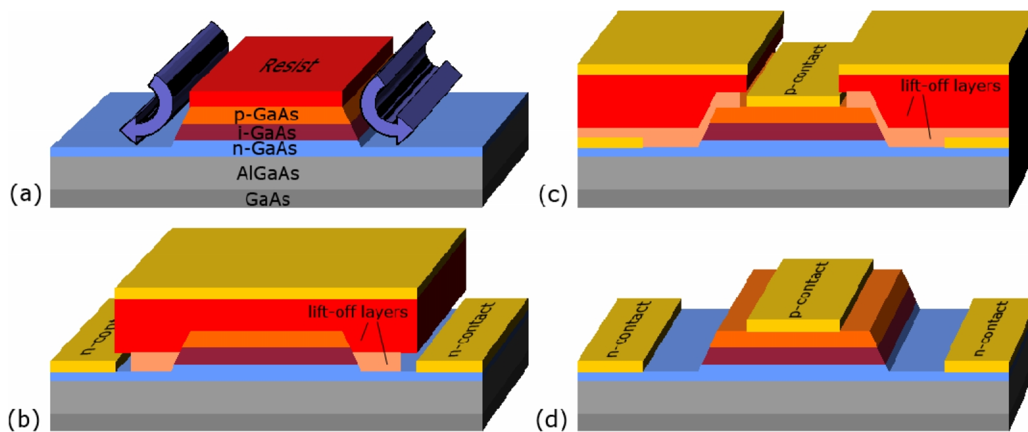

Figure 5.1 Fabrication of electrically pumped stripe waveguide stripe device: Waveguide is defined with a resist and unprotected sites are etched to expose the n-layer (a). In the next step, a first lift-off mask covers the waveguide and opens only windows over the n-GaAs layer where the n-contact is evaporated (b). A second lift-off mask was reapplied and p-contacts on top of the waveguide evaporated (c). After removal of the mask the sample is ready for cleaving and characterisation (d).

---

[1] Please refer the appendix A for a detailed list of all fabrication processes.

[2] The fabrication exposed an issue with the wafer that only about the upper few 10's nanometres of the n-layer were conductive. In this sense, the accuracy of few nanometres was almost necessary to obtain an electrical conductive sample.

for contact evaporation on the etched n-GaAs surface, a bi-layer lift-off structure is used. The bi-layer process consists of two layers with different solubility, therefore require different development times and hence establish an undercut. Due to the undercut, the evaporated metal layer on top of the surface does not form a continuous film and the solvent can pass through it and lift-off both resists. Prior to the loading of the sample into the evaporator, the sample is dipped into ammonium hydroxide to remove native oxide layer. A composition of different metals is thermally evaporated with an electron beam evaporator in the following order: 14 nm Au, 14 nm Ge, 14 nm Au, 11 nm Ni and 200 nm Au [Verlangieri91], thus minimizing the contact-resistance. After evaporation, the lift-off resist is dissolved in a solvent[1] and ready for the annealing. The annealing step at 450ºC reduces the contact-resistance by inter-diffusion of metal atoms into GaAs and creating an intermediate region between the metal contact and GaAs layer. In the last step, the second metal contact composition – 20 nm NiCr and 200 nm Au – needs to be deposited on top of the waveguide, p-GaAs layer, by creating a window for the contact with the bi-layer resists similar to the previous step. The alignment of the latter window to the waveguide has to be accurate within 5 um to avoid overlapping with the wet-etched n-GaAs region and hence electrical shortcuts. In this sense, it is useful to use narrower contacts than the waveguide to avoid this problem. After resist removal the sample is ready for cleaving and testing.

As indicated above, problems appeared when performing the wet-etch step in the presence of a metal, as pictured in Figure 5.2 (a). In this case, the wet-etch was performed after evaporation of the p-contact and led to complication during the wet-etch. Away from the metal-contact the etched n-layer had a uniform thickness; close to the metal-contact, however, a deep trench formed that cut into the conductive channel. The wet-etch solution even crawled under the contact-resulting in a sloped waveguide (Figure 5.2 b). These problems can be avoided by etching down to the n-layer at the beginning of the process, before the metal deposition. A

---

[1] Inappropriate solvent can etch GaAs even if areas are covered by a metal or resist as it will be shown later in this section.

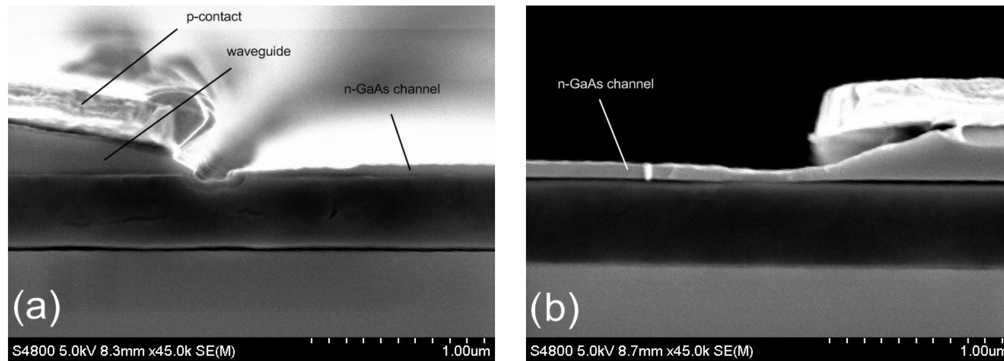

Figure 5.2 Cut through the n-GaAs channel, close to the waveguide edge, during wet-etch with resist covering the p-contact (a). Wet-etched n-GaAs channel with the under-etched contact due to the resist developer (b).

similar problem occurred when the standard developer Shipley MF-319 was used to remove the remaining lift-off resist after contact evaporation. In general, the lower layer of the bi-layer stack is more difficult to remove and needs longer soaking in the solution at higher temperatures. In the past, MF-319 used at higher temperature proved efficient as a remover for some GaAs based devices. The main ingredient Tetramethyl-Ammonium-Hydroxide (TMAH) significantly etches Silicon, Aluminium and GaAs at higher temperatures, however. When fabricating standard laser in GaAs, this removal of few 10's of nanometres in warm MF-319 does not cause a serious problem. In our case, however, the etch depth of the n-layer needs to be controlled with nanometre accuracy, so the MF-319 can case fatal problems by this additional etching. A simple solution was found by replacing MF-319 with an even more efficient remover (Shipley 1165) that is based on pure organic solvents which is safe for most typical semiconductors and metals. Once these problems were addressed, I was able to fabricate a full device, as shown in Figure 5.3. The cross-section shows one side of the waveguide with the wet-etch characteristic slope of the sidewall and the p-contact only a few micrometres away from the edge. The expected carrier flow is as follows: electron are injected though the n-contact into the wet-etched region and drift within the thin n-channel towards the waveguide, where they preferably recombine radiatively with the holes injected through the p-contact.

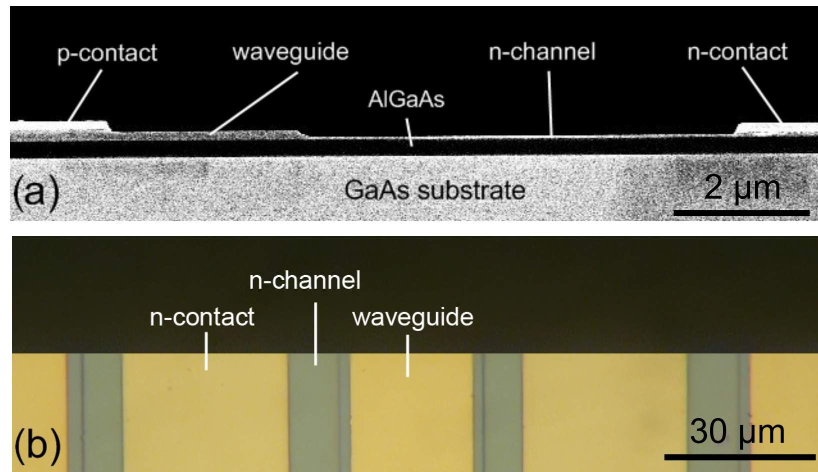

Figure 5.3 SEM image of a cleaved front of the waveguide stripe device (a). The n-contact is connected to the p-contact through the about 90 nm high n-channel on to of the non-oxidised AlGaAs layer. Microscope top-view of cleaved front with a 30 µm wide waveguide in the centre and the n-contacts at the sides (b). Please note that this is a repeating structure with about 20 waveguides.

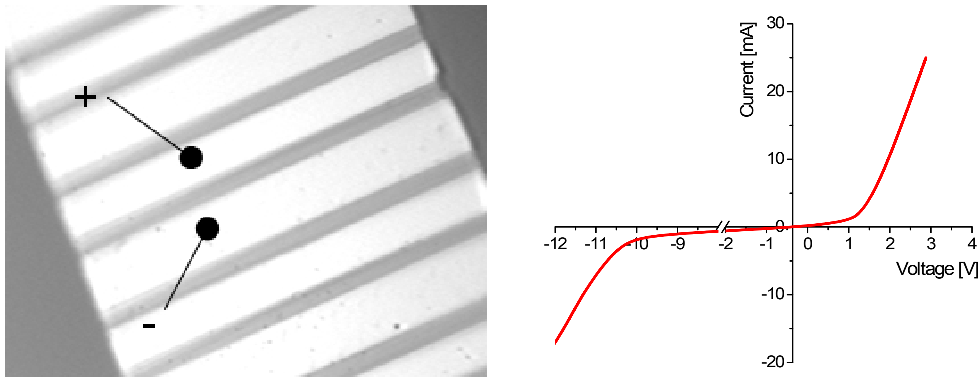

Figure 5.4 Top-view of a 200 µm long device and measured IV curve. Device with p-contact on top of the waveguide ("+" polarity) and the n-contact on the wet-etched area ("-" polarity). The connections indicate the polarity of the carrier injection in forward bias. Measured IV curve with diode behaviour, switch-on voltage in forward bias and high breakdown voltage in reverse bias.

5.2.1.2 Characterisation of Stripe-laser Electrical Devices

Electrical probes are used to inject carriers, into the device as indicated in Figure 5.4. A typical measured current-voltage (IV) characteristic of the device shows a diode behaviour with high breakdown voltage in reverse bias and a switch-on voltage of

about 1 V which corresponds approximately to the energy of the photons at 1200 nm wavelength emitted from the QDs. This confirms that a pn- or pin-junction is present. As mentioned before, it is difficult, if not impossible to obtain the doping concentrations of this multilayered structure, although we can investigate the behaviour when changing the device length. In this way, we gain understanding of the resistance of the ePCL.

We obtain the device resistance by calculating the inverse slope of the forward biased region. Four different devices with lengths of 200 µm, 700 µm, 1300 µm and 2000 µm were measured and their behaviour shown in Figure 5.5. The device resistance of the longest device with a length of 2000 µm is only 15 Ω but increases to 60 Ω for a 200 µm long device.

Deriving the total device resistance R_{total} from the expected current path in Figure 3.2 includes the partial resistances for the n- and p-contacts R_{cn}, R_{cp}, the partial resistances of the paths across the n- and p-material R_n, R_p and an internal junction resistance R_i as shown in Eq.5.1.

$$R_{total} = R_{cn} + R_{cp} + R_n + R_p + R_i \quad \text{(Eq.5.1)}$$

Expanding the terms of Eq.5.1 results in:

$$R_{total} = \frac{r_{cn}}{L_C W_{cn}} + \frac{r_{cp}}{L_C W_{cp}} + \rho_n \frac{L_n}{L_C t_n} + \rho_p \frac{t_p}{L_C W_p} \quad \text{(Eq.5.2)}$$

where r refers to the specific contact-resistances, W to the channel width, L_n to the length of the n-channel, t to the layer thickness, ρ to the sheet resistance and L_C to the length of the device. The main essence of Eq.5.2 is the inverse proportionality of the total device resistance R_{total} on the device length L_C:

$$R_{total} \propto \frac{1}{L_C} \quad \text{(Eq.5.3)}$$

This represents the results in Figure 5.5 with a hyperbolic behaviour. Decreasing the device length even further – several micrometres like in the final device – will increase the resistance to several 1000's Ω as shown in Figure 5.5 (inset). These values lie in the order of magnitude of the theoretical predictions but should be

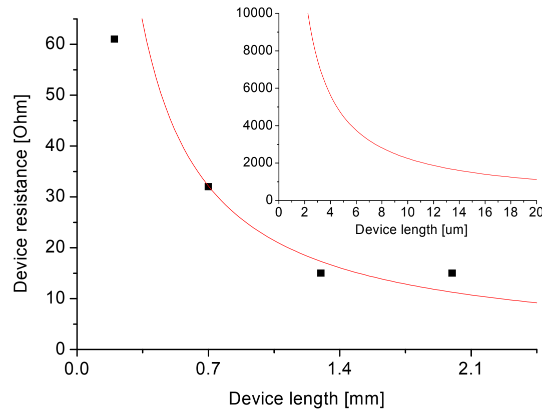

Figure 5.5 Device resistance for different device lengths (dots) calculated from the inverse slope of the forward biased IV curves. Red line shows the best fitted, relative dependency after Eq.5.3. Inset: Zoom of calculated line for device lengths of up to 20 μm.

considered carefully, because in the final device other dimensions such as path length will be decreased as well which reduces the device resistance. On the other hand, attempts to calculate the specific contact-resistance (not shown here) gave relatively high values. Due to the small contact areas, the contribution of the contact-resistance to the total resistance might be high and past experiments with VCSEL showed a few orders of magnitude higher specific contact-resistance than corresponding literature values [Verlangieri91]. Apart from different doping levels, the higher pressure during our evaporation might be a cause for increased contact-resistance.

5.2.2 Vn1807: ePCL Electrical Device

The electrical design of the final ePCL is comparable to a few micrometres short stripe waveguide design. Let us now have a look at the fabrication steps before presenting measurements on the discrete device.

5.2.2.1 Fabrication of ePCL Electrical Devices

The order of the steps is the same as for the stripe waveguide device shown in Figure 5.1, starting with the n-GaAs wet-etched followed by n-contact evaporation and p-contact evaporation. Figure 5.6 shows a single device fabricated for electrical testing without the PhC cavity. The fabrication steps are the same as for the waveguide

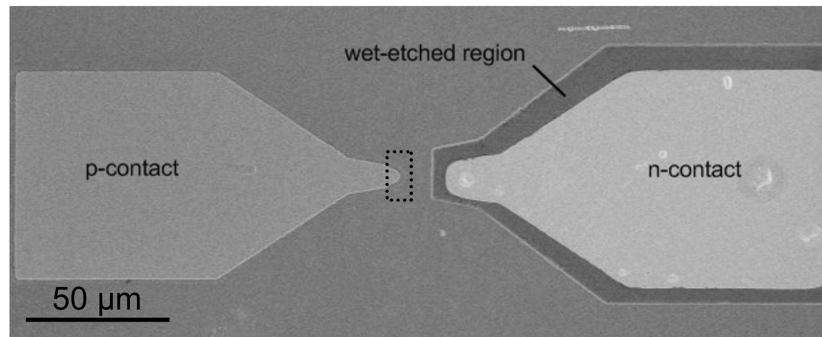

Figure 5.6 SEM image of a single ePCL device without the PhC cavity. This device is one element of a two-dimensional array on one fabricated sample. The dashed box in the centre indicates roughly the position of the PhC cavity. Bubble formation on the n-contact occurs occasionally during annealing, which is not fatal for the device.

devices utilizing only a different set of lithographic masks. Electrons are again injected through the n-contact into n-GaAs and drift towards the p-contact, where they recombine with holes, injected through the p-contact. The main difference to the waveguide structure are the tapered contacts and the short distance between them. As shown in chapter 3 "Design and Simulations of ePCL" the carrier density can be tailored i.e. by tapered contacts, achieving high densities inside the cavity region.

5.2.2.2 Characterisation of ePCL Electrical Devices

The IV curve I obtained is shown in Figure 5.7. Diode behaviour can again be seen, but the slope in forward bias is not straight, which might be caused by the two-dimensional geometry of the device; by increasing the voltage, the current might take slightly different paths and therefore changes the slope of the curve. The turn-on voltage is 1.6 V, i.e. higher than expected, which indicates an additional contact-resistance in this fabricated device. On the other hand, the breakdown voltage is with about 17 V higher than in Vn1315 after Figure 5.4. Calculating the total device resistance from the forward bias slope gives a value of 1600 Ω. This value lies again in the expected range and largely depends on the distance between the p-contact and the n-contact. In the final device this distance will have to be minimised in order to keep the resistance low, given that the perforated nature of the PhC will further increase the total resistance.

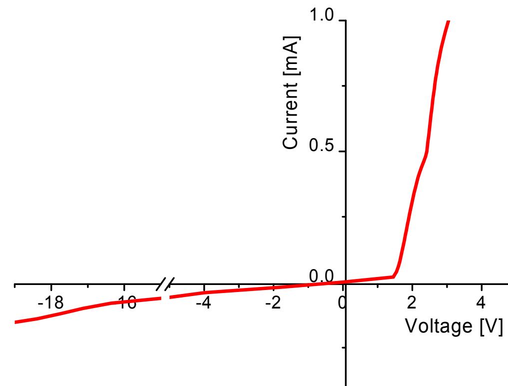

Figure 5.7 IV curve of electrical ePCL structure with the diode behaviour. Turn-on voltage is about 1.6 V in forward bias and the breaktdown voltage is more than 17 V in reverse bias.

The electrical testing showed that current flow with diode behaviour is possible in these wafers. Moreover, the resistance of the early devices are in the range of 1000 - 2000 Ω as predicted by the electrical simulations.

5.3 Optical Properties

Achieving gain in a resonator is necessary for laser operation and this will be the main aspect of the following sections. In the design chapter, the gain of the system was estimated based simulations and on literature values. In this chapter, I first try to determine the gain of both wafers by pumping them optically and electrically and check for lasing.

Photoluminescence (PL) refers to light emission induced by carrier generation due to pumping with light of a wavelength shorter than the band-egde – smaller than 860 nm for GaAs. Direct injection of carriers into the material and observation of light emission is called *electroluminescence (EL)*. PL is more popular because is does not require metallic contact or similar structures for carrier injection, on the other hand it requires a more sophisticated setup than for EL. Pumping with a wavelength below the band-edge creates carriers and heat proportional to the energy difference to the band-edge. In this sense, the efficiency of PL is lower than for EL. Finally, EL is the aim for most devices as it does not require an additional light source.

5.3.1 Fabrication of Stripe-laser Devices

The fabrication of a device for PL does not require metal contacts, so is relatively easy to fabricate. Basically, only one etch-step is needed to create such a waveguide. Due to the small index difference between the guiding layer and the bottom cladding, however, the confinement is weak. Stronger confinement can be achieved by oxidising the bottom cladding, which requires a second etch-step as it will be shown later. From this point of view, we have two different types of devices fabricated and measured:

1. Non-oxidised AlGaAs bottom cladding
2. Oxidised AlGaAs bottom cladding

At first, the waveguide is wet-etched (Figure 5.8 1a). Using wet-etch and the ability to control the etch-depth creates a ridge-type waveguide with a depth just above the bottom cladding. Care has to be taken that the etch stops before reaching the AlGaAs layer, otherwise the AlGaAs would be dissolved very quickly in the wet-etch solution due to its chemistry. Conventionally, the waveguide is etched by dry-etch process where no control over the etch depth is needed. In our case, it would cause problems with the underlying AlGaAs layer if it is exposed to air. Oxidising AlGaAs in air leads to; slow oxidation rate, different phases of oxide layer expansion, causing the facets to break. On the other hand, oxidising at high temperature in a controlled steam atmosphere speeds up the process and creates the desired low refractive index phases. This type of oxidation leads to a contraction and introduces stress to the layer that can peel off the substrate, especially for larger areas. The risk of the layer peeling of is lower if the structure is sideways supported by the non-oxidised layer, opposite to a free-standing mesa. The non-oxidised device is now ready for cleaving and testing (Figure 5.8 2b). Achieving strong light confinement requires oxidation of the bottom AlGaAs layer. First, the AlGaAs layer is exposed by dry etching using Chlorine-Assisted-Ion-Beam-Etching (CAIBE) as shown Figure 5.8 (2a). Wet-oxidation is then used to transform the high index AlGaAs layer into low index Aluminium-Oxide (AlOx) after [Geib97]. Choosing the right conditions for the oxidation such as sample temperature, nitrogen carrier gas flow

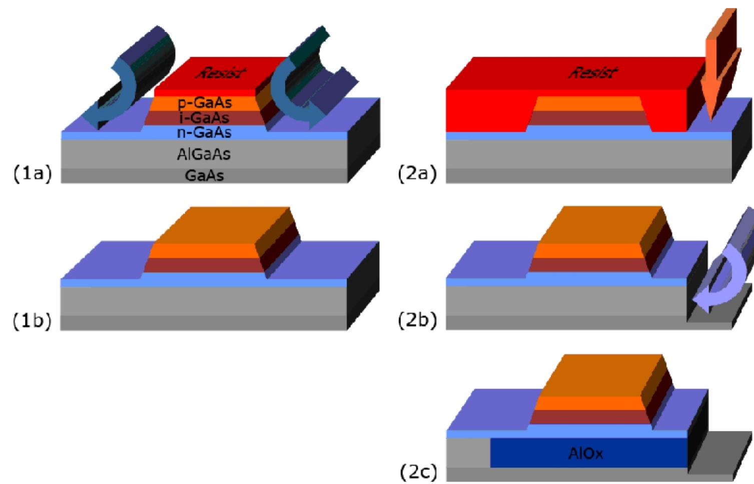

Figure 5.8 Fabrication of optically pumped stripe-waveguide device. Non-oxidised device: Wet-etch of waveguide (1a) trough a mask (top of structure, red) with stop of the tech before reaching the AlGaAs layer and finished device in (1b). Oxidised device: Deep-etch trough AlGaAs layer until reaching GaAs substrate (2a) followed by wet-oxidation (2b) and finished device in (2c).

– transports the steam from the heated water reservoir to the reaction chamber – is important to obtain the proper phases, acceptable rate and a repeatable process. Also structural features such as access areas to the AlGaAs layer, as well as layer thickness and aluminium content determine the rate [Ku03], [Kim96]. The biggest problem besides the repeatability is the timing of the process, which depends on the oxidation rates and hence repeatability again. If the timing is too short the oxide does not reach the important regions and if it is too long, undesired phases develop and the GaAs even starts to oxidise. We found that oxidation performed in a steam atmosphere with a sample temperature of 450 ºC, 80 ºC water reservoir temperature and 400 sccm nitrogen flow gave an oxidation rate of 0.44 µm/min for our structure. At the end, the sample is cleaved to obtain smooth facets that act as mirrors of the 1 mm long Fabry-Perot resonator (Figure 5.9).

The waveguide has a width of 20 µm and the underlying AlGaAs layer is fully oxidised. The oxidation front (Figure 5.9 b) is clearly visible because of the different phases of the material: non-oxidised AlGaAs is crystalline (left from oxidation front) whereas AlOx is amorphous (right from oxidation front). Larger grains can be seen on the oxidised side that result from the oxidation chemistry and different oxidation products of the AlGaAs layer [Twesten96], [Guha96]. These grains are clearly present at the upper GaAs/AlGaAs interface as well and might cause scattering. But,

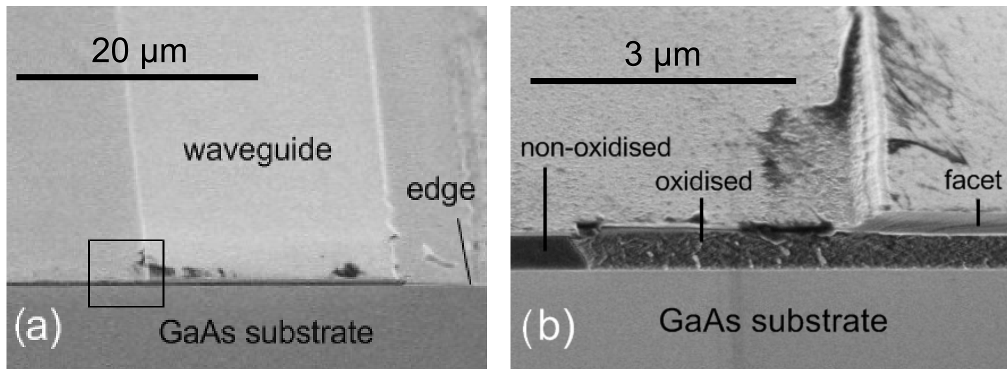

Figure 5.9 SEM images of oxidised waveguide device. Micrograph (a) corresponding to Figure 5.8 (2c) with the waveguide in the centre and a deep-etched trench on the right side. Zoom into (b) dashed box from left image. Oxidised layer under waveguide with stopped oxidation front on the right.

there are three reasons why this might not cause a big problem: (1) These pictures were taken by electrons instead of light, which detects different properties as light would do. Moreover, it is important how homogenous the refractive index of the layer is distributed, because the grains might have similar indices but the electron cannot visualise it. (2) The grains might only be visible after cleaving due to some grains boundary effects so that the layer is homogenous inside. (3) The oxide consists of different types of Gallium-oxide compounds. These compounds might have similar refractive indices around 1.6 and because scattering scales with the index difference, the contribution to the total loss will be small [Ravaro07], [Almuneau11]. We will continue after the measurements with this discussion.

Another feature of the waveguides is the angled sidewall that results from the isotropic wet-etch. This should not interfere too much with the light guiding mechanism because of the larger width of the waveguide. Looking at the facet, the cleaving was successful resulting in straight facets. But, after cleaving, the exposed AlGaAs layer oxidises at room temperature depending of the Al-concentration, which can lead to a layer expansion and breaking off the facets. Therefore, measurements on the non-oxidised samples were performed on the same day, otherwise new samples needed to be cleaved.

Waveguides were fabricated out of both wafers, however, oxidation was only performed with Vn1315. The reason for this is the reduced Al-concentration of the

Vn1807, which improves the QDs quality, but results in a lower oxidation rate. I was therefore not able to fully oxidise the width of the waveguide.

5.3.2 Characterisation of Stripe-laser Devices

Testing of these devices requires the pumping of the entire waveguides from the top and collecting the emitted light from the facets. Lasing can then be identified by the characteristic threshold kink, whereas gain can be measured in a *pump-probe configuration* where a signal beam is passed through the pumped waveguide and transmitted light is then collected as illustrated in Figure 5.10.

The QDs are excited by the pump beam and amplify the incoming signal. Eq.5.4 gives the relationship between the net amplified signal I_A and the following measured output signals: with pumping/signal I_P, without pumping I_{WOP} and without signal I_{PL}. The model gain g_{mod} can then be calculated with knowledge of device length L as shown in Eq.5.5.

$$I_A = I_P - I_{PL} = I_{WOP} e^{g_{\mathrm{mod}} L} \qquad \text{(Eq.5.4)}$$

$$g_{\mathrm{mod}} = \ln\left(\frac{I_P - I_{PL}}{I_{WOP}}\right)\frac{1}{L} \qquad \text{(Eq.5.5)}$$

Only the net modal gain, which contains all losses, can be determined in this configuration, because both beams are passing through the waveguide and are equally affected by the losses. Additional losses induced by free-carriers, which are generated by the pump beam, are estimated by calculating the carrier generation rate and looking up their absorption loss. The carrier generation rate G_C is equal to the

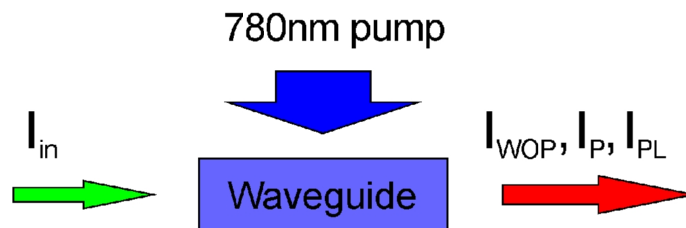

Figure 5.10 Principle of the pump-probe measurement. The signal (green) is coupled into the waveguide and the output is measured. From the ratio of measured output signal between the pumped and unpumped case, considering the QD photoluminescence, we can derive the modal gain.

photon flux Φ, assuming that each photon creates an electron-hole pair. Replacing the photon flux Φ with the pump beam intensity I_P and taking into account the absorption coefficient a and the slab thickness d, we obtain the following expression:

$$G_C = \frac{I_P}{E_{ph} e} \alpha (1 - e^{-\alpha d}) \quad \text{(Eq.5.6)}$$

with e as the elementary charge and E_{ph} the photon energy. Using a pump intensity of $I = 200\ W/cm^2$, a photon energy of $E_{ph} = 1.59\ eV$, an absorption coefficient of $a = 14300\ cm^{-1}$ and $d_1=320\ nm/d_2=420\ nm$ (Vn1315 and Vn1807, respectively) we obtain an estimated carrier generation rate $G_{C1} = 6.1 \times 10^{24}\ cm^{-3}s^{-1}$ and $G_{C2} = 5.1 \times 10^{24}\ cm^{-3}s^{-1}$. Assuming that the radiative lifetime is dominant over non-radiative lifetime, we use 1 ns as a radiative lifetime of the carriers. Therefore, the amount of generated carriers is $c_1 = 6.1 \text{x} 10^{15}\ cm^{-3}$ and $c_2 = 5.1 \text{x} 10^{15} cm^{-3}$ for Vn1315 and Vn1807, respectively[1]. The absorption coefficient for these carrier densities is lower than 0.01 cm^{-1} [Spitzer59] so that we will neglect the effect of free-carrier absorption here. Propagation losses of a waveguide can be determined by a section method [Hakki75], but it is difficult to implement this method with optical pumping and was therefore not performed here.

From the practical point of view, the source of the signal has to be broad enough to scan the full wavelength range of the QDs, which was difficult to establish because 1550 nm is the favourable wavelength range of the measurements done in this laboratory. A pulsed broadband white-light source was used as the probe with an estimated peak power density in the order of 10’s μW/nm, which was measured at the Optical Spectrum Analyser (OSA). The OSA is averaging the pulse resulting in a much lower average power. Because of this averaging, we could not lower the probe power much further otherwise the signal would be undetectable. We therefore attempted to set the OSA to trigger the pulse, with no success so we had to stay with the averaging option. To restrict the wavelength range from 1000 nm to 1300 nm,

---

[1] This is an estimate assuming a homogenously doped material as this is not the case here, however, for ease of calculation we assume this.

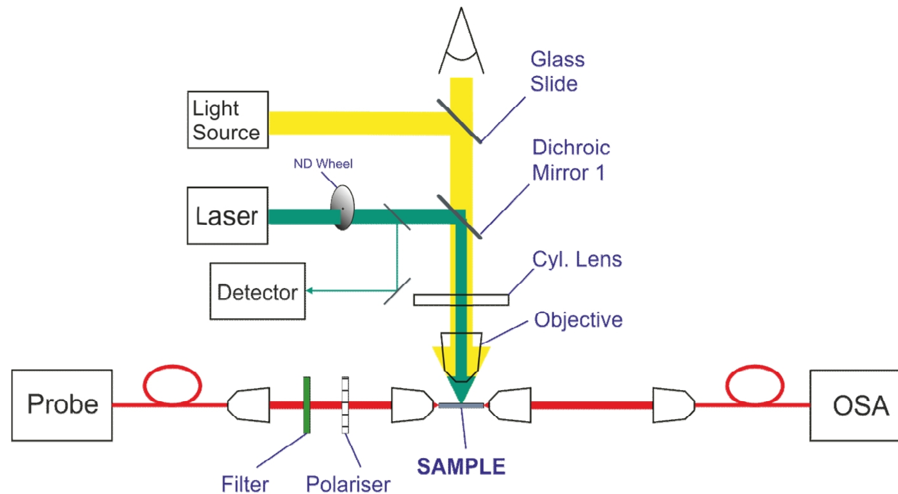

Figure 5.11 Setup for pump-probe measurements. The probe signal is end0fire coupled into the waveguide and the output signal is collected in a similar way. A set of filters and a polariser are used to condition the signal beam. Pumping of the waveguide is performed from top via a objective and a cylindrical lens. The pump intensity can be varied and the waveguide can be inspected through a camera.

overlapping with the QD emission range peaking at about 1210 nm, we used a set of filters. In addition, we also used a TE polariser because the QDs mainly interact with TE – electric field vibrates in-plane – due to the disk-shape geometry of QDs. The schematic of the setup is shown in Figure 5.11. The horizontal signal beam is focused onto the facet of the waveguide for coupling whereas the output beam is coupled into a fibre and analysed by an OSA. Continuous pumping of the waveguide is performed by focussing a 780 nm laser diode onto the waveguide. The output beam of the 780 nm diode is first collimated, then stretched by a cylindrical lens in order to enable homogenous pumping of the high aspect waveguide dimensions of 20 μm x 1000 μm. Finally, the beam is focussed down by a 20X microscope objective down to the required dimensions and to obtain the highest intensity possible.

5.3.2.1 Characterisation of Wafer Vn1315

The modal gain can be calculated by comparing the spectra of the output signals after Eq.5.5 and Figure 5.12 shows an example of the acquired curves. Due to the

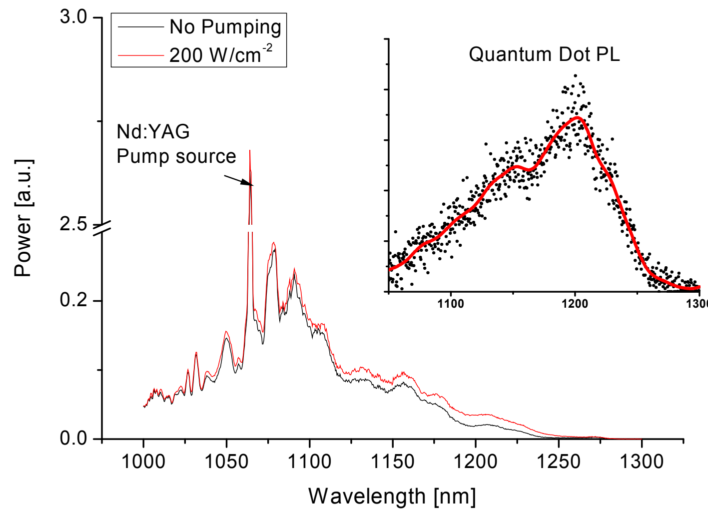

Figure 5.12 Example spectra recorded with the OSA. Pumping the waveguide results in a spectral increase of the power (red curve) in respect to the reference spectrum without pumping (black curve). The strong peak at 1064 nm corresponds to the internal pump source of the white light source. The inset shows the recorded photoluminescence of the QDs.

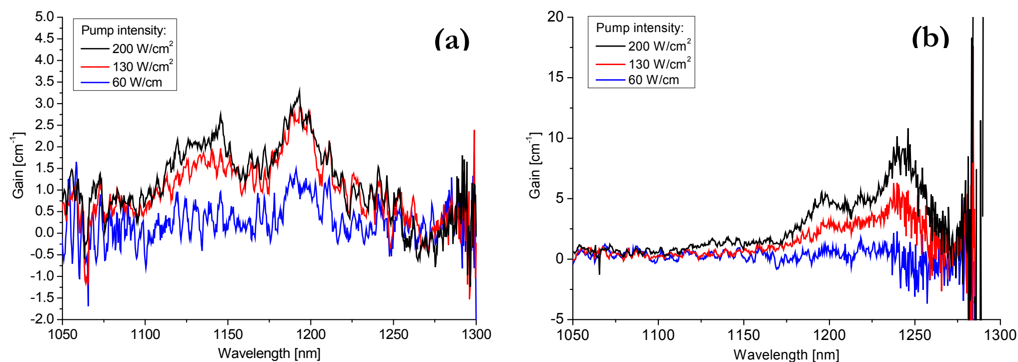

Figure 5.13 Gain-spectra for non-oxidised (a) and oxidised (b) devices of Vn1315. In both cases, the increase in pump power leads to an increase gain.

filter used here, several peaks appear in the spectrum, but do not affect the resulting gain spectrum. Pumping the waveguide increases the power in the spectral range where the QDs emit (Figure 5.12 inset).

The gain spectra are derived using Eq.5.5 and are shown in Figure 5.13 with a significant difference in values between the non-oxidised and the oxidised sample. When increasing the pump intensity, the gain increases as well, as expected. On the other hand, the shapes of the gain curve as well as the maximum values differ, although the same material has been used. At 1200 nm, the gain for the non-

oxidised sample is about 3 cm^{-1} while it reaches 5 cm^{-1} for the oxidised sample. There are some factors that we have to reconsider regarding the guiding properties and losses of the waveguides in order to explain the difference in both curves. First, the propagation loss and radiation loss of the non-oxidised waveguide increases due to the optical field leaking through the 400 nm thin high refractive index AlGaAs layer into the GaAs substrate. Second, scattering losses may arise at the GaAs/oxidised AlGaAs interface. Scattering losses of partially oxidised AlGaAs of a sandwiched GaAs layer were investigated in [Bek98] where the losses for TE polarisation were 0.6 cm^{-1}. Further, the propagation losses of an oxidised high Al-content AlGaAs layer on top of low Al-content AlGaAs layer were measured to be 3.0 cm^{-1} by [Lou99]. On the other hand, different values of the Al-content and oxidation parameters lead to different phases in the oxide so that we can not say if these values are applicable to us. Therefore, we also can not conclude with certainty, if and how high the losses in the waveguides are, but these are not important for the gain analysis. Eq.5.4 does not consider these losses, because the unpumped and pumped signal experience the same propagation losses, if no other losses are induced by the pump beam.

The overlap of the mode with the active region is important because better overlap delivers higher gain. Let us therefore discuss the difference of the non-oxidised and the oxidised waveguide by comparing their theoretical confinement factors. The confinement factor is made up of the confinement in-plane Γ_{xy} and the vertical confinement Γ_z in form of $\Gamma = \Gamma_{xy} * \Gamma_z$. The in-plane confinement is defined as the dot coverage ε that was calculated to $\Gamma_{xy} = \varepsilon = 0.194$ in 3.2.2 “Loss and Gain Evaluation”. The dot coverage is material defined and constant for both samples. When calculating the vertical confinement factor, with a mode solver, we obtain $\Gamma_{zOx} = 0.058$ for the oxidised structure and $\Gamma_{zNOx} = 0.043$ for the non-oxidised structure. Although, the vertical confinement factor for the non-oxidised waveguide is lower, due to a mode shift towards the substrate, the difference does not completely explain the difference in gain after Figure 5.13. The gain spectrum in Figure 5.13 (b) also differs from (a) in the position of the peaks, which are at longer wavelengths in contrast to (a). This is a strong indication that there is a problem

with the guiding properties during pumping. Before we go into the discussion of the results, we now present the result from Vn1807.

5.3.2.2 Characterisation of Wafer Vn1807

Only non-oxidised waveguides were fabricated out of this material because of the low Al-concentration and the slow oxidation rate. All other conditions, such as fabrication process and waveguide width, were kept identical to the Vn1315. When increasing the intensity, the gain increases as expected, but also here the curves are shifted to higher wavelengths as in the previous result. Here, the gain is with about 7 cm^{-1} higher than in the previous wafer for the non-oxidised waveguide (Figure 5.13 a.).

Most likely, the gain curves do not represent the actual values of the material because of the following reasons: (1) The pumping of the waveguide might have actually introduced optical loss due to free-carriers. The amount of generated carriers was earlier calculated, but it was only an estimate. (2) The continuous-wave pumping heats up the waveguide and this can not only influences the QD dynamics and the wave-guiding properties so that the guiding properties are not identical for the pumped and un-pumped case. (3) The probe power needs to be further reduced because of gain depletion [Liu09]. This, however, was not possible because the pulsed probe-signal could not be triggered with the OSA and therefore the detected average signal was low.

Lasing was not observed in both samples, even at the highest level of pumping. This might be due to insufficient gain or high loss. I have tried to obtain the loss by moving the pumping beam along the waveguide direction, but due to the wide Gaussian spot it was not possible to obtain the losses correctly. The pump laser diode used here delivered a nominal power of about 70 mW, which resulted in about 200 W/cm^2. Taking the intensity at the threshold of 600 W/cm^2 for a 10 layer QD stack [Rafailov06] it becomes clear that we did not reach the value for the threshold of 300 W/cm^2 – for our 5 layer stack in Vn1807. Vn1315, on the other hand, should have reached some gain to overcame transparency, but losses were most probably high and inhibited the threshold. Therefore, we can conclude that the pump power was not sufficient to reach maximum gain and to overcome loss.

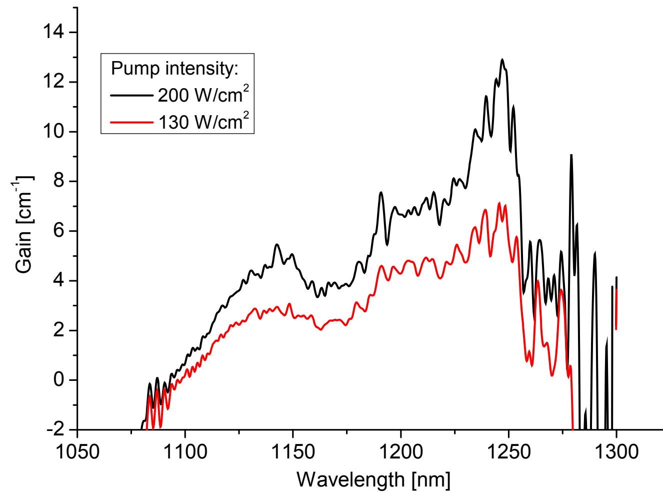

Figure 5.14 Gain-spectra of Vn1807. Pump-probe measurements show an increase in gain with pump intensity.

Electrical pumping can provide higher carrier densities and will therefore be investigated in the final section.

5.3.3 Electrical Pumping of Stripe-laser devices

Here, we use the device from section 5.2.1 "Vn1315: Stripe-laser Electrical Device" in combination with the optical light collection with the OSA. Pumping the device from Figure 5.4 in forward bias, light emission is seen via the top-view camera. The emission is mainly concentrated at the edges close to the contact (Figure 5.15). The line where the emission appears is visible along the whole waveguide a dimming when further away from the pumping spots. This indicates that the current spreading over 200 µm is not optimal and will be worse in longer devices. This was expected because the wafer was designed for smaller device geometries. Moreover, the appearing of just one visible line gives further evidence for the poor current spreading when this material is used for devices with larger dimensions. Ideally, the whole waveguide needs to be pumped, instead strong asymmetry is observed. This can be explained by the low mobility of the p-layer that results in recombination close to the p-contact. Exactly this effect is observed here, where only one side close to the contact emits, namely this one close to the lower n-contact where the electrical probe is connected. Using two probes connected to both n-contacts show

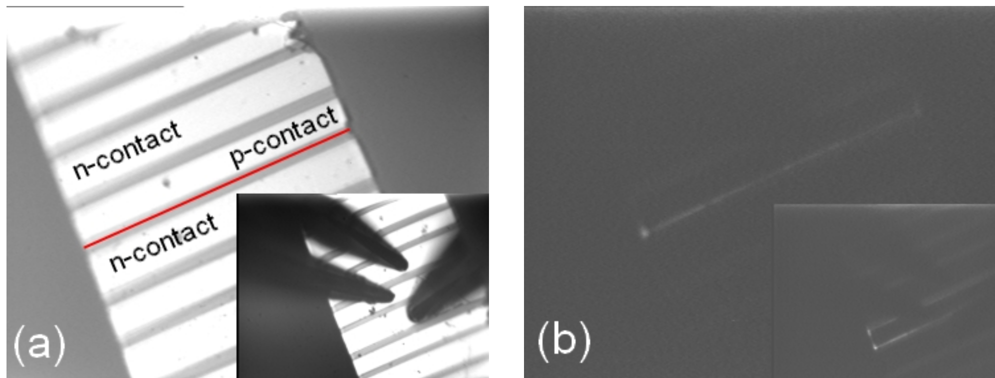

Figure 5.15 Forward biased 200 μm long device. Illuminated top-view, where the two dark spots show the points of pumping (a). Dark top-view (b) of identical area to (a). A halo can be seen around the pumped waveguide with a brighter line in (b) corresponding to the area indicated with the red line in (a). Inset shows pumping of waveguide symmetrical from both sides of the waveguide. Please refer to Figure 5.3 and Figure 5.4 for further device details.

a more symmetric emission (Figure 5.15 (b) inset); however, the centre of the waveguide still appears dark at the facet. There is another reason why the bright spots, at the facets, are only visible at the sides where no metal contact is above them. In conventional stripe waveguide lasers the metal contacts are not in direct contact with the optical field, where losses through increased absorption are present. Simulations made with a Beam-Propagation-Method (BPM) solver of light propagation within the waveguide showing a slight decrease of the optical field travelling along the waveguide (Figure 5.16 a) without the metal contact. This is due to the low refractive index difference between the GaAs slab and the AlGaAs layer, where light is leaking through the AlGaAs in the lower GaAs substrate. Placing a metal on top of the slab introduces additional loss and the field decays faster. On the other hand, in the case of a conventional stripe waveguide device a AlGaAs buffer is used between the slab and the contact, the decay of the optical field is smaller than in the previous case. This can be attributed to the mode being pushed upwards resulting in a reduced leakage in the GaAs substrate. But most important, the field does not have a strong overlap with the metal contact anymore and therefore the absorption loss is reduced. Apart from the carrier recombination close to the p-contact, the proximity of the field to the metal contact might be a reason why there is not light visible at the centre of the facet in Figure 5.15. Attempts

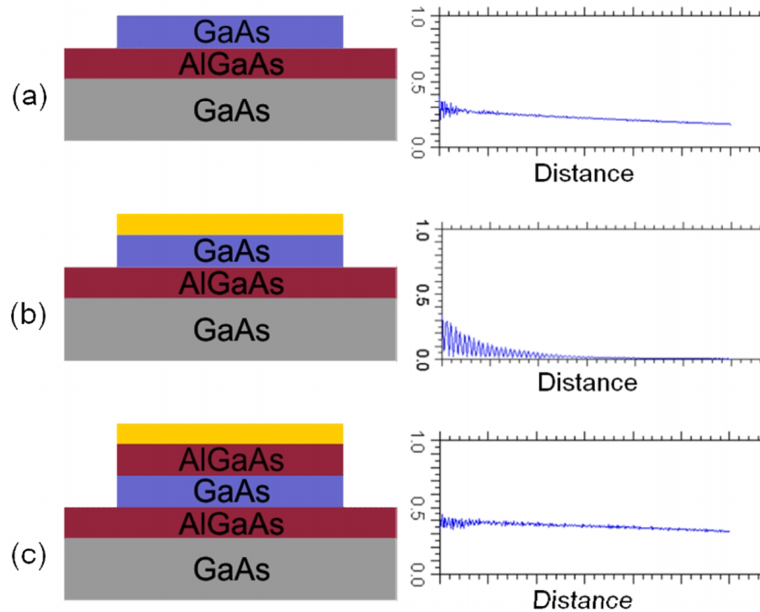

Figure 5.16 BPM simulation of the optical field decay along the direction of the waveguide for three different layer structures. Used structure with AlGaAs below the mode guiding GaAs slab and the GaAs substrate at the bottom (a). Metallic contact placed on top of the structure (b). AlGaAs used as a buffer between the slab and the contact (c).

were made to optically pick up the emission at the facet for spectral analysis either by objectives or tapered fibres with no success. This is due to the inefficient carrier injection for the long device and high absorption of the metal contact so that the amount of light is low as well as the directionality out of the waveguide.

To conclude, the measured gain is lower than expected and is most likely due to a too high probe power, which was limited by the equipment and resulted in a low value of the measured gain because of gain depletion. No lasing via optical pumping was observed due to weak light guiding – wafers are not designed for waveguide devices – and insufficient pump intensity to overcome the loss. Electrical injection showed a limitation of the wafer structure for large dimensional device like waveguides and high light absorption for proximate metal contacts.

In the next chapter, the properties of photonic-crystal cavities are investigated that are more suitable for this wafer design. They will also be tested for lasing, aiming for the ePCL.

Chapter 6

Photonic-Crystal Cavity and Fabrication of ePCL

6.1 Introduction

This chapter is a follow up of the optical material characterisation from the previous chapter. Here, different types of Photonic-Crystal (PhC) Cavities are fabricated and measured to ensure suitable Q-factors can be achieved. Moreover, we also test the cavities for optically pumped lasing to confirm the material properties such as the gain.

In the second part of this chapter, we combine individual fabrications in order to build the ePCL.

6.2 Photonic-Crystal Cavities

6.2.1 Fabrication of Photonic-Crystal Cavities

We fabricate two different geometries: *membrane cavity* and *oxide cavity* as shown in Figure 6.1. The first type is desirable in the case of obtaining the highest possible Q-factors due to the highest index difference in the vertical direction. On the other hand, the cavity with oxidised AlGaAs is more practical when looking at the robustness and improved thermal properties. From the fabrication point of view, the oxide cavity is more difficult to fabricate because it requires deeper holes – the

Q-factor is proportional to the hole-depth – and an additional oxidation step, which can be difficult to control.

Typical fabrication methods for cavities employ soft-/ or hard-masks to transfer the pattern into the material by dry-etching. Electron-beam sensitive soft-masks such as the Poly(methyl methacrylate) (PMMA) or Zep-520A are widely used to directly write the pattern into the resist. Hard-masks, on the other hand, are less sensitive to the dry-etch therefore allow harsher etch conditions and structures with higher aspect-ratio than soft-masks. Silicon-Dioxide (SiO_2), Silicon-Nitride (SiN) or some metals are widely used in addition to the soft-mask and hence require an additional dry-etch step to transfer the pattern from the soft-mask into the hard-mask. Our design requires small holes with a high aspect-ratio in order to obtain high Q-factors and therefore a hard-mask, but there is an issue with their removal. Removal of these hard-masks should be carried out with a wet-etch instead of a dry-etch, because dry-etch damages the surface and the material, both structurally and electrically[1]. This is where the problem with our geometry lies. Hydro-fluoric (HF) acid is used to remove the hard-mask, which does not attack GaAs. AlGaAs, on the other hand, is attacked by HF depending on its Al-content there being high resistance for an Al-content below 40% and decreased resistance with increasing Al-content.

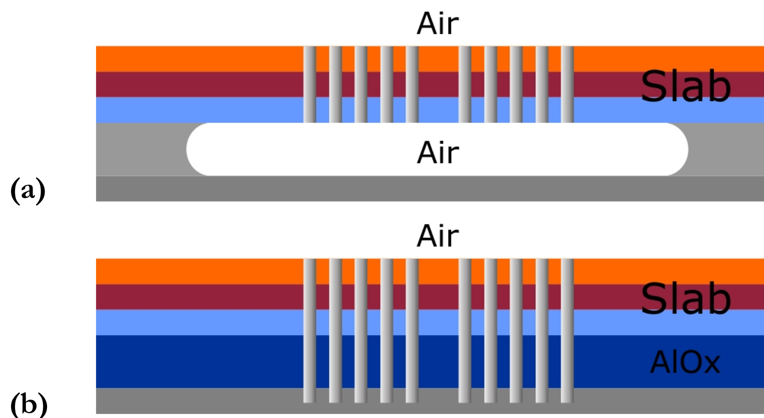

Figure 6.1 Cross-section of cavity geometries: the membraned cavity (a): The slab is fully surrounded by air (above and below the slab including the holes) and oxide cavity (b) where the slab is sitting on oxidised AlGaAs with air above the slab and inside the holes.

---

[1] Electrical damage can be removed by high-temperature annealing, due to the relaxation of damaged bonds. It is not used here because the structural damage does not improve with annealing; furthermore, high-temperature annealing influences the QD emission.

Our Al-content is above 80% and a hard-mask with HF following removal cannot be used without further complications. Therefore, the performance of ZEP-520A as a soft-mask is investigated in the next section.

6.2.1.1 Dry-etch with a Soft-mask

As shown in the waveguide section, the Vn1807 wafer has higher gain than Vn1315 and is therefore more promising to achieve lasing. To use the Vn1807 sparingly, we used Vn1315 for the first etch-test with the soft-mask.

After cleaving and cleaning of the sample, ZEP-520A is spun-on with a resulting thickness of about 380 nm after a 10 min hard-bake at 180 °C. ZEP-520A is a high performance positive electron-sensitive resist, i.e. only the features that have to be removed in the developer are exposed. This is very suitable as we only have to expose the circular holes, which saves exposure time. The exposure is performed with the RAITH ELPHY/LEO GEMINI 1530 hybrid electron beam writer at the maximum electron acceleration of 30 keV to increase the penetration depth and to reduce the electron scattering range of secondary electron that leads to the exposure of the resist. When designing the pattern for the electron beam writer, two real-life considerations have to be made regarding the electron scattering inside the resist and the substrate. Firstly, the electron beam is a few nanometres wide, but inside the resist, it scatters into the forward direction and the average width increases to about 20 - 30 nm. Taking this into account, we reduced the design radius by 20 nm to obtain the desired hole-diameter. Secondly, the backscattering of electrons inside the GaAs also occurs over a distance of a few 100's nanometres and therefore lightly expose a wider range of the resist. It is obvious that central holes – surrounded by other holes – experience higher doses than the outer holes due to the increased scattering range. This effect is called "proximity effect" and needs to be corrected; otherwise the central holes would have a larger diameter than the outer holes due to the increased dose of the central holes. We used the NanoPECS tool to account for this effect with the parameters taken from the experience of other group members. After exposure, the features are developed for 45 s in Xylene at 23 °C. It is more important to consistently develop at the same temperature rather

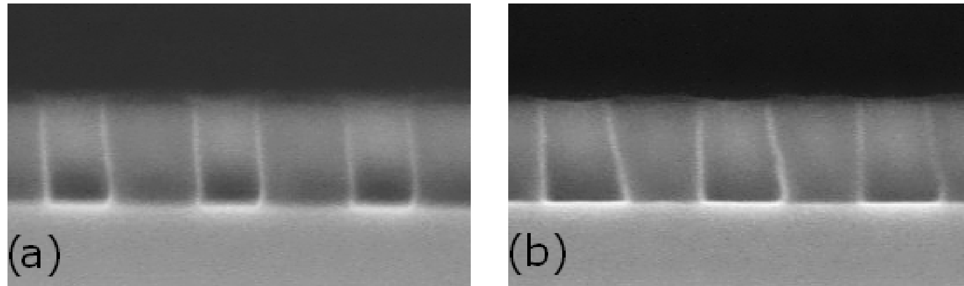

Figure 6.2 Cross-section through electron beam exposed and developed ZEP-520A resist. Holes received the correct dose (a) with near-vertical sidewalls. Higher nominal dose (b) for each hole resulting in sloped sidewalls. The hole-diameter at the top is about 180 nm. Note that the bottom of the holes is shifted to the right. This is an artefact caused by sample drift inside the SEM due to resist charging effects.

than at exactly 23 °C, in order to obtain reproducible hole-diameters, as the development rate depends on the temperature. Cleaving trough a developed PhC sample reveals the profiles of the holes (Figure 6.2). Vertical sidewalls are preferred as they are the precondition for a good vertical etch of holes. The nominal dose – multiplication factor times the design dose times the base dose – of 0.9 resulted in near vertical sidewalls (Figure 6.2 a) in contrast to a nominal dose of 1.1 (Figure 6.2 b).

Pattern transfer from the resist into the substrate is performed by dry-etching with the CAIBE as in shown in section 5.2.1 "Waveguide Pumping" with the difference that the process window is much narrower for PhC than for waveguides. Parameter optimisation of the PhC etch is more crucial than for waveguides in order to obtain high quality PhCs. This is why we explain the dry-etch process in more detail than in the waveguide section. The CAIBE is a special system with a unique feature; it enables the decoupling of the two main etch-mechanisms: *physical* and *chemical etching*. Physical etching is caused by ion bombardment of the material, while chemical etching is based on the chemical reaction with the material, forming volatile compounds that are then removed by the vacuum system. Chemical etching alone leads in most cases to isotropic etching while physical etching is nearly anisotropic. The right balance of both mechanisms and the low vacuum operation (~ $1x10^{4}$ - 10^{3} mbar) makes CAIBE superior to standard Reactive-Ion-Etching (RIE) and allows the fabrication of high aspect-ratio features. As the exact process mechanism is very

complex, we will not try to explain it here; however, we will point out details which are important for the high quality PhC fabrication. Important parameters for the etch are as follows;

- Substrate temperature: determines the chemical etch rate due to thermal activation energy and volatility of the reactants.
- Physical bombardment, gas and flow rate: the noble gas Argon is used here which is ionised and accelerated towards the sample; the flow rate determines the etch rate.
- Chemical etching, gas and flow rate: Chlorine is used here as it reacts well with GaAs, especially at elevated temperatures; the flow rate determines the etch rate.
- Ion beam voltage and current: the electric potential in the ion gun is set to the desired voltage and the beam current sets the ion density; an increase in both parameters leads to an increase in etch rate, but also an increased rate of mask erosion.
- Operating pressure: low pressure leads to a more efficient removal of volatile reaction products and to a better quality of narrow features.

The aim is to obtain 1 μm deep, high quality holes with a small diameter (~ 150 nm), therefore we took an existing recipe and changed the etching time to achieve the highest depth possible. The parameters for these first etches performed were: 100 °C

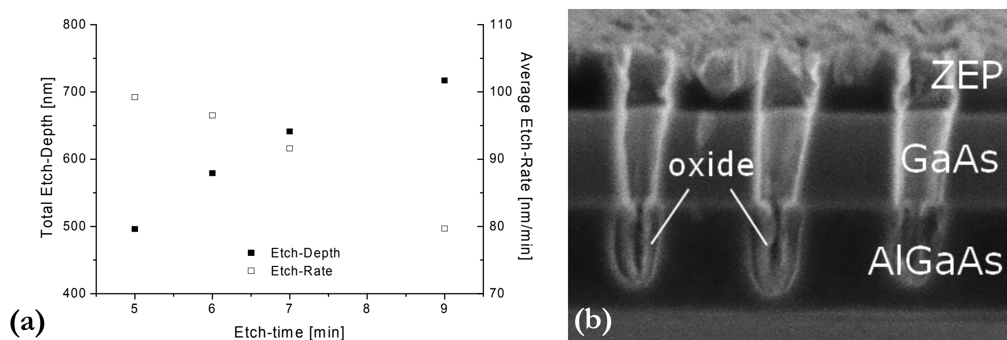

Figure 6.3 Graph displaying etch-depth vs time (a) for standard parameters as listed in the text. Cross-section (b) showing an example etch-profile with different layers for approximately 200 nm wide holes. The exposed AlGaAs inside the holes oxidises when left for a few days a [give example of what “long time“ means] in air-atmosphere.

substrate temperature, 50 sccm Ar, 40 sccm Cl_2, 350 V beam voltage, 10 mA beam current, pressure of $3x10^{-4}$ mbar resulting in example etch profile shown in Figure 6.3 (b). Although the total etch-depth is saturating, it would be possible – when increasing the etch time – to achieve 1 µm deep holes[1] of 200 nm in diameter. The etch-rate of ZEP-520A under these conditions is about 30 nm/min (data not shown here) so that the maximum etch-time is about 12 min (380 nm resist thickness/resist etch rate). Looking at the cross-section in Figure 6.3 (b), we see that the quality is poor and the resist is deformed – from its original shape after Figure 6.2 (b) – and seems to be non-uniformly attacked from the top. This deformation was also observed in [Yoon00] where a hard-mask was used instead. Here, however, we want to investigate whether we can improve the hole-quality by changing the etch-parameters. Doing so, the parameters were modified in numerous tests and the hole quality inspected, with no significant improvement for deep holes. There is always a resist deformation visible as shown in an example in Figure 6.4 (a) with a tendency of stronger deformation with increasing beam voltage or beam current. Here, the deformation is very strong resulting in star-shaped holes that are then transferred into the GaAs. On inspection of the surface of the resist, it seems that the resist contracts and forms an inhomogeneous surface and sharp corners. This is an indication

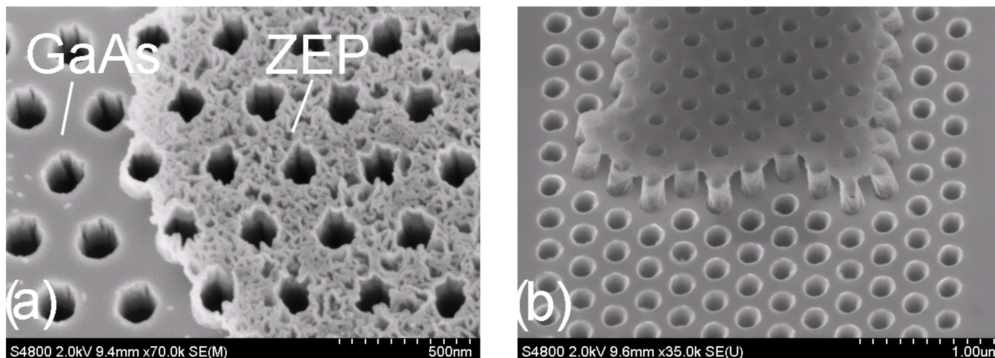

Figure 6.4 Example etch (a) with the bare GaAs on the left and the resist on the right. The edges of the star-shaped holes are transferred into the GaAs during the etching process. Partly removed resist in solvent in (b). It is clear that the inner past of the resist was removed but the surface is more resistant to the solvent.

[1] Please note that the etch rate is an average value because the etch rate of GaAs is about a factor 0.5 higher than the AlGaAs etch rate.

of a physical/chemical reaction of the resist as a consequence of the ion bombardment and/or the chlorine exposure. Removal of the resist with the dedicated "1165" solvent is usually successful, but there are some regions on the sample where the resist is more difficult to remove. One of the random regions is shown in Figure 6.4 (b) where a skeleton of the resist is still standing while the inside has been completely removed. Two distinct structural features are more resistant the solvent: the sidewall-tunnel around the holes and the top-surface. These regions have experienced a direct exposure of the ions, resulting of a hardening of these regions. At this point, we can not distinguish which of the etch mechanisms is responsible for the resist hardening/deformation. Even the combination of both mechanisms may be responsible, as the argon ions may activate the chlorine leading to higher etch-rates than each of the individual etch mechanisms alone. To investigate which of the etch mechanism is responsible, we separated the two mechanisms by performing etches with only the physical bombardment and chlorine exposure. The result is shown in Figure 6.5. With pure physical etching, the GaAs is only slightly etched by ion bombardment/sputtering (Figure 6.5 a). Deformation of the top-surface of ZEP-520A is visible, which is not surprising as this is a soft-mask. On the other hand, deformation also occurs at the sidewalls inside the holes, which is more difficult to explain. A plausible explanation includes backscattered ions from the GaAs surface hitting against the sidewalls and

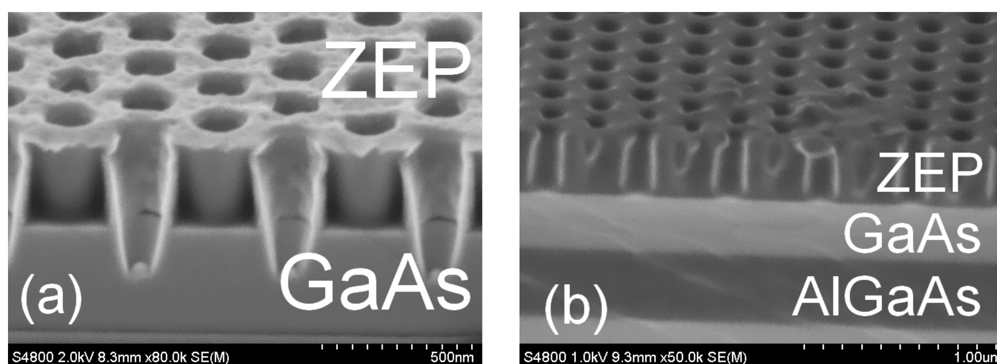

Figure 6.5 Investigation of physical and chemical impact on ZEP-520A.. Ion bombardment (a) at 500 V beam voltage, 10 mA beam current for 5 min with visible sidewall and top-surface deformation. Chlorine exposure (b) for 5 min at 100 °C where partly reflowed top features are visible.

causing deformation as seen on the top-surface[1]. Pure chemical etching alone does not deform the holes in any form, only resist reflow is visible due to the high temperature of 100 °C (Figure 6.5 b). From this point of view, the ion bombardment is mainly responsible for the deformation, although chlorine exposure and the high temperature might increase the deformation. We conclude that ZEP-520A can not be used for our etching requirements – deep holes with small diameter – as it deforms and these deformations are transferred into the GaAs and strongly reduces the hole-quality.

Despite this setback, we would prefer not to give up on the soft-mask because a hard-mask would cause many problems for its removal, therefore we investigate a soft-mask hardening technique to reduce the deformation. This hardening technique involves a combination of a hard-bake and a UV exposure. *Czaplewski et al.* developed the technique and showed a decrease of the ZEP-520A etch-rate during the RIE process [Czaplewski09]. A hard-bake step is always recommended prior to a wet-etch but can also help to harden the resist before a dry-etch. One has to be careful, however, because high temperatures and long baking times can result in a reflow of the resist, and in the worst case, diminish small features. On the other hand, UV exposure can result in significant degradation as is often the case for polymers on exposure to UV. Different heat treatments and exposure times have been explored in order to see any effects on the deformation. Following e-beam writing and resist development, the hole had a round shape with a diameter of about 180 nm. This shape was deformed during the reference etch as shown in Figure 6.6 (a). Testing the parameters for hard-baking gave an optimum time of 5 min at 90 °C prior to the UV exposure as longer baking times and higher temperatures resulted in a reflow of the resist. The UV-exposure was performed with a UV lamp at 254 nm at about the same intensity as in [Czaplewski09]. Exposure-times were changed to investigate the effect of the dose the resist was exposed to. Figure 6.6 (b) shows a representative sample with the treatment, although no reduction in the deformation was observed. The upper limit of the UV exposure was about 20 min where the holes

---

[1] A test not shown here with a low beam voltage of 150 V has shown no penetration into GaAs but widening up of the holes due to backscattered ions, which did not penetrate into GaAs.

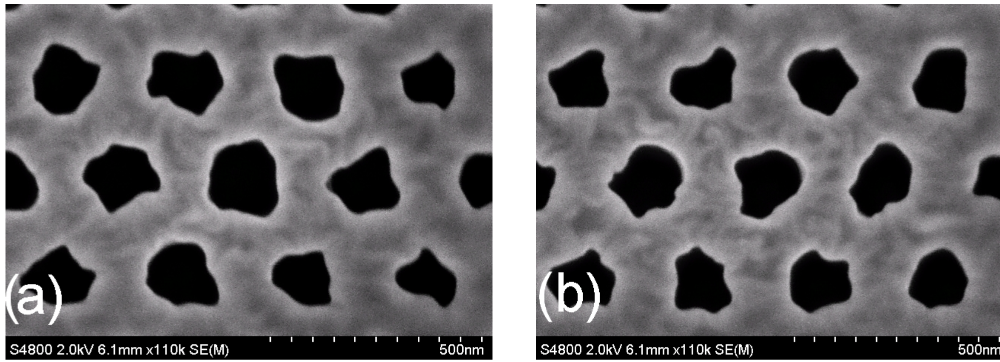

Figure 6.6 Resist hardening through heat treatment and UV exposure. Reference etch (a) without treatment, where the round holes have deformed during the etch. Treatment (b) with 5 min hard-bake at 90 °C and 10 min UV exposure with no difference to the reference.

start to show an even stronger deformation and shrinkage after the etch. After varying the parameters, we could not observe any reduction in deformation of ZEP-520A during the CAIBE etch which would allow us to proceed with the soft-mask. We finally conclude that ZEP-520A is not suitable for masking PhC in a high voltage CAIBE etch due to the strong resist deformation induced by ion bombardment and we have to consider a hard-mask after all.

6.2.1.2 Dry-etch with a Hard-mask

Hard-masks such as SiO_2 and SiN are typically used as masking materials on substrates, which are resistant to HF attack, such that the masks can be easily removed in an HF etch. This is not possible for the high Al-content AlGaAs substrates that we are using. Before we can discuss the hard-mask material itself, we have to think about a removal method following the CAIBE etch. One possibility is to use a dry-etch technique, but this brings some disadvantages, which might be fatal for the device performance. Two consequences can result from the dry-etch, which are both related to the damage created by the ion bombardment: physical and electrical damage. In the case of physical damage, ions hitting the GaAs surface and the hole-sidewalls generally leave a rough surface behind that will decrease the Q-factor of the cavity. Additionally, the ions also create electrical damage by creating structural disorder on the atomic scale, thus degrading the electrical performance of the contacts. Electrical damages can be removed by in-situ Cl_2 treatment [Daleiden99] or lattice relaxation/dopand reactivation at high temperatures

[Collot90], however, physical damage will remain which ultimately affects the Q-factor via increased scattering.

Only a wet-etch is able to remove the hard-mask while leaving the material intact. This is only true if the etch-rate of the material is negligible small as it is the case of GaAs in HF solution. The problem with AlGaAs with an Al-content of > 40 %, however, is that it dissolves very quickly in HF. A possiblity would be to substitute HF with a solution that etches the hard-mask but does not etch AlGaAs. This is a difficult task as the removal of materials – suitable as hard-mask – require strong acids or bases such as HF, sulphuric acid, phosphoric acid or nitric acid. These etchants, besides etching AlGaAs, also etch GaAs at considerable rates and can not be used for the removal of the hard-mask. If we can not find a replacement for HF that does not attack AlGaAs, we have to make sure that the HF does not come into contact with the AlGaAs.

Therefore, I developed an original method to remove the hard-mask without dissolving the AlGaAs. The method is based on a polymer refill of the PhC holes and is illustrated in Figure 6.7. The CAIBE etch process creates deep holes that expose the AlGaAs layer, which is necessary for the oxidation step (Figure 6.7 a). In

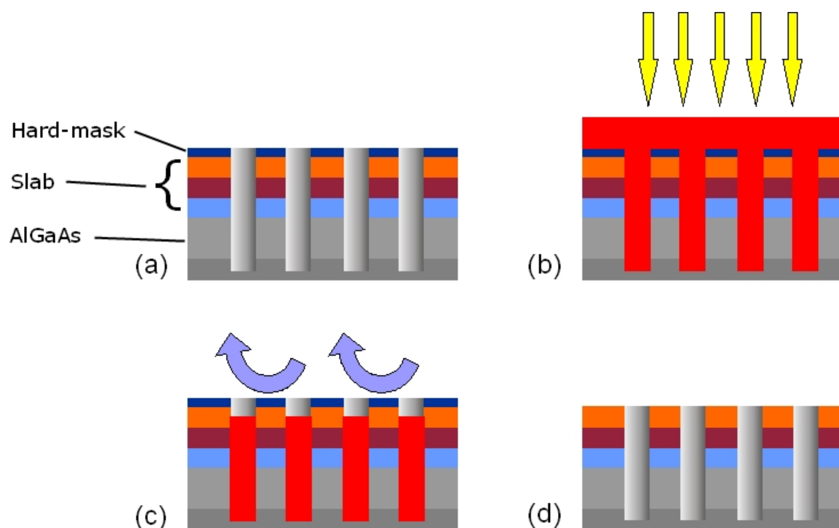

Figure 6.7 PhC refill method following the HF wet-etch of the hard-mask. The AlGaAs layer is exposed after the CAIBE masked by the hard-mask (a). Photoresist is spun on the sample and it infiltrates the holes. After controlled exposure and development, only the top part of the resist is removed. The hard-mask is removed in HF solution (c), thus keeping the AlGaAs layer intact (d).

the subsequent step, the positive resist S1805 is spun on and the sample placed in a vacuum chamber for 3 minutes to drive out any air bubbles remaining in the holes, resulting in a resist thickness of about 500 nm (b). The following UV-exposure[1] is very crucial as only the resist on top of the surface has to receive a dose high enough to be removed in the developer while the resist inside the holes should remain undeveloped. This procedure is very sensitive to environmental conditions and also to sample resting times after the hard-bake and the exposure etc. where some conditions can change from day-to-day. Because of the day-to-day fluctuations a calibration curve (Figure 6.8) has to be performed every time to assure the consistency of this procedure. Measurements of the remaining resist thickness, for different exposure times, result in the calibration curve where an extrapolation of the data points reveals the exposure time necessary for a complete exposure of the resist above the surface. In general, points in the range up to about 100 nm from the surface scatter stronger than points with higher remaining resist thicknesses due to

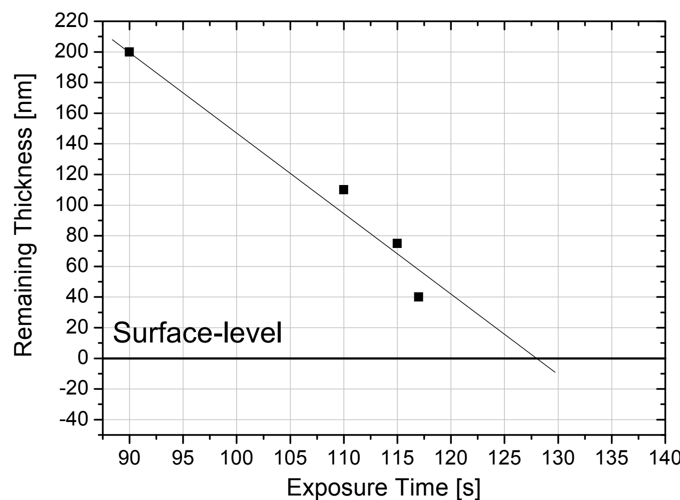

Figure 6.8 Example of calibration curve for every day the procedure is performed. Starting with a short exposure time, the time is increased to obtain enough data points for an extrapolation to the surface level. The remaining thickness after development is obtained with a profilometer. The measurement accuracy is estimated to be about ± 4 nm.

---

[1] Every negative tone resist with a high contrast can be used for this procedure such as the electron-beam sensitive resist ZEP-520A. In fact, using ZEP-520A in combination of an electron-beam writer would allow even higher exposure control as the dose can be set very accurately. On the other hand, electron-beam writing time is precious and the available writing time is limited.

interference effects or resist reaction with the hard-mask[1]. The remaining thickness is measured on a plain surface away from the PhC, but above the PhC, the resist thickness reduces – due to the contraction of the resist during the hard-bake – by about 100 nm. This means that on the extrapolation point, where the surface is fully exposed, the level inside the holes is already about 100 nm lower. Therefore, one has to take care that the exposure time is not far away from the extrapolation point. After exposure and development with the extrapolated time, the real sample is once again measured and inspected, optically and with the SEM. At the end, the sample is descummed in an oxygen plasma asher for a short time to remove residual resist resulting in an back-filled PhC as shown in Figure 6.9 (a). Inspection of the back-filled sample inside the SEM shows that the polymer is clearly infiltrating the holes according to the sketch in Figure 6.7 (c). In the next step, the sample is hard-baked prior to the wet-etch for 1 h at 90 °C to improve the resistance against HF solution. In first tests made with 1:5 (HF:H_2O) solution, the resist was strongly attacked by the HF solution allowing contact to the AlGaAs layer that then dissolved rapidly resulting catastrophic damage to the PhC. Switching to buffered HF (BHF) consisting of 1:6 (HF : Ammonium Fluride) solved this problem, as it dissolved the hard-mask within 10 min while leaving the high-quality PhC intact (Figure 6.9 b). With this method, we are able to remove the hard-mask without dissolving the

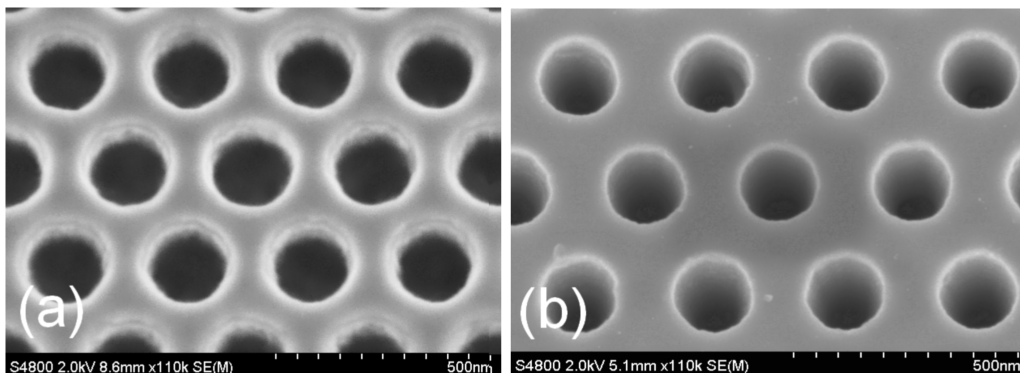

Figure 6.9 PhC holes after refilling and wet-etch. Angled-view SEM micrograph of holes after the CAIBE etch and the refill (a). The holes are clearly infiltrated and the beginning of the hard-mask is visible as a sharp edge wider than the holes. After HF removal of the hard-mask (b), the high quality of the holes is apparent.

[1] As it will be shown in the next section, we are using a special type of hard-mask that tends to modify the properties of the resist resulting in more difficult to control exposure times.

AlGaAs layer, hence we have established that a hard-mask can be used. We can now move on and consider the type of material that we want to use as a hard-mask.

Let us define the requirements for the hard-masks as follows, in order of importance:

1. Low etch-rate in the CAIBE
2. Moderate etch-rate in the RIE system, as the pattern from the ZEP-520A has to be transferred into the hard-mask
3. Ease of application.
4. Availability in the cleanroom.

In order to be considered as a hard-mask, the etch-rate of the material in the CAIBE has to be low, implying that the material is hard enough to endure a harsh etch environment. When using a hard-mask, a soft-mask is still needed for the pattering with the electron beam writer unless the pattern is directly written into SiO_x such as the resist hydrogen-silsesquioxane (HSQ), also known as flowable oxide (FOx) or spin-on glass [Baek05]. We still want to use ZEP-520A for the pattern definition because of its high resolution and low base dose so that the hard-mask has to be etched faster than ZEP-520A in the RIE. The third requirement is the method for applying the film onto the substrate. Deposition via sputtering or evaporation is preferred over spin-coating as our sample size is small – several mm^2 – and spinning might cause problems because of non-uniformity of the film. As the final requirement, we would also like to use our facilities to apply the film because of having control over the film properties and to minimize the lead time.

Materials used as hard-masks can be divided into two groups: dielectrics and metals. An overview over the requirements SiN_x, SiO_x, and TiO_x[1] – for the dielectrics group – and Ni as a representative from the metal group are listed in Table 6.1. SiN_x is considered to be one of the best hard-masks due its low etch-rate in the CAIBE –

[1] The proper stochimetry is not known for the evaporated films due to thermal decomposition of the loaded SiN_2, SiO_2 and TiO_2 substrates. An alternative to sputtering, where thermal decomposition can be counteracted, is reactive evaporation involving O_2 or N_2 gas feed and a heated sample holder.

Table 6.1 Overview over the requirements for typical hard-masks. Measured values, unless stated.

Material	1. CAIBE etch-rate	2. RIE etch-rate	3. Applicableness	4. Availability
SiN_x	<10 nm/min[1]	20 nm/min[2] (Y)	CVD/Sputtering	No
HSQ	10 nm/min (500V)	10 nm/min (Y)	Spin-coating	Yes
TiO_x	5 nm/min (500V)	100 nm/min (Y)	Evaporation	Yes
Ni	2 nm/min (500V)	2 nm/min (N)	Evaporation	Yes

usually less than SiO_x – and high etch-rate in the RIE. The etch rate in the RIE, shown in Table 6.1, is a relative value, depending on various etch conditions. The important aspect is whether the pattern from ZEP-520A can be fully transferred into the hard-mask before ZEP-520A is fully consumed. This is acknowledged by an (Y) for yes and (N) for no as the 2nd requirement inside the table. SiN_x is a very good hard-mask as it can also be deposited onto small samples via various types of Chemical-Vapour-Deposition (CVD) or sputtering, but, we do not have CVD facilities or a sputtering machine available. Tests with evaporated SiN_x resulted in high etch-rates in the CAIBE – comparable to GaAs – suggesting a poor film quality with high Si content. HSQ is similar to SiO_x after high temperature curing – ~400 °C – with a low etch-rate in the CAIBE and a good pattern transfer in the RIE. Only the spin-coating of small samples caused problems due to the non-uniformity of the film. TiO_x is reportedly being used as a hard-mask [Chung00] due to its hardness, but has not previously been used for PhC fabrication. The hardness of the evaporated material was confirmed via its low etch-rate in the CAIBE (5 nm/min at 500 V beam voltage and 10 mA current). On the other hand, the etch rate in the RIE is very high, which makes it an ideal candidate for a hard-mask. The deposition of the film is done with standard electron beam evaporation and therefore suitable for small samples.

Metals are good hard-masks as they can be very difficult to dry etch, which makes the pattern transfer very difficult as the etch-rates in the CAIBE and RIE are similar

[1] Estimated

[2] Taken from very recent fabrication results of SiN_x PhC made by a colleague in our group.

and mostly due to physical etching[1]. Pattern transfer from ZEP-520A into Ni was not possible because ZEP-520A was etched away before a sufficient depth in the hard-mask was reached. This is the reason why the majority of pattern transfers into metals is performed by a lift-off process rather than by etching. A lift-off process of PhC holes with small dimension is extremely difficult if not impossible.

Out of these four hard-mask options, only TiO_x fulfils all requirements as it is very resistant inside the CAIBE, ease of pattern transfer inside the RIE and possibility of evaporation on small samples with our facilities. Initial etch tests of TiO_x were performed with pure SF_6 chemistry [Norasetthekul01] in the RIE. The pattern from the ZEP-520A was successfully transferred into the 120 nm thick hard-mask. The

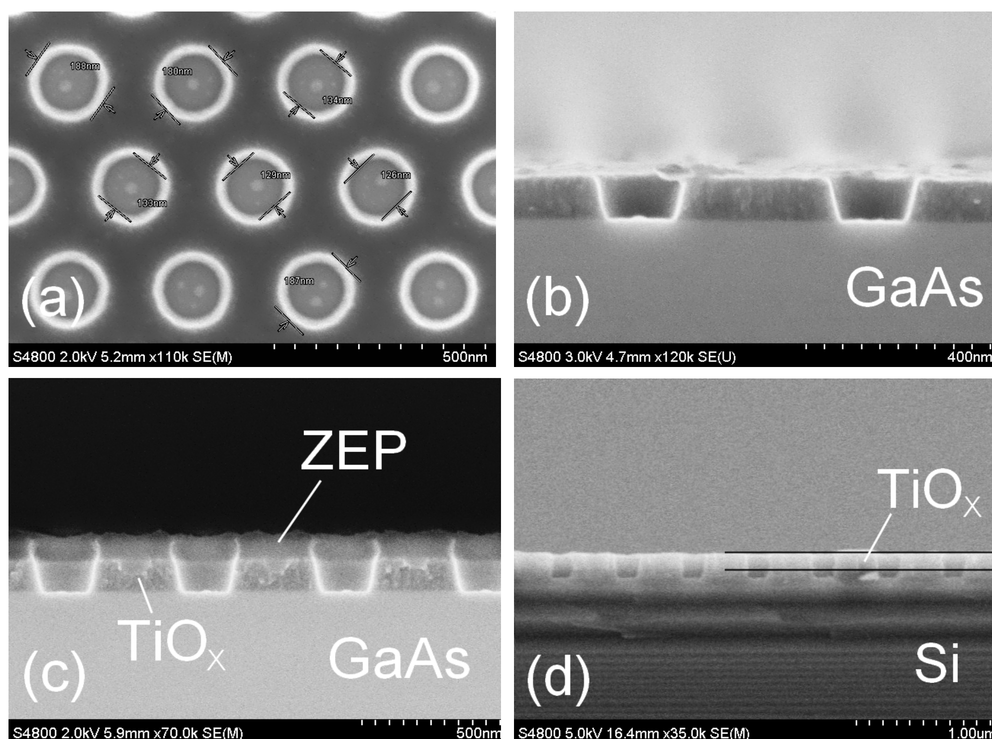

Figure 6.10 RIE etch of 100 nm thick TiO_x hard-mask on GaAs (a) with 10 sccm SF_6 flow, 5.9^10^{-2} mbar pressure, 20 W power for 60 s. Top-view shows a white edge around the holes that corresponds to the sloped sidewalls (17°) in (b). Optimised etch (c) with reduced sidewall angle to 14°: 10 sccm SF_6, 100 sccm CHF_3, 2.5^10^{-2} mbar pressure, 20 W for 120 s. Etch test with TiO_x hard-mask on Si (d) sample with near vertical sidewalls.

[1] In some cases, especially for Al and Ti, an oxide layer can form on the metal surface even lowering the etch-rate. Ar ion bombardment is then used to remove the oxide layer before starting the actual etch.

holes are smooth – despite visible larger grains – and circular (Figure 6.10 a), however, the sidewalls are sloped to about 17° Figure 6.10 (b). In order to reduce the sidewall angle, further etch tests were performed by changing etch conditions such as pressure, power and etching gasses with summarised results:

- Decreasing pressure: reduced sidewall angle due to increased ion voltage and increased directionality at lower pressures.
- Increasing pressure: reduced sidewall angle due to increased scattering inside the holes, but also a strong increase in sidewall roughness.
- Increasing power: No significant change in sidewall angle, but strong increase in sidewall roughness.
- CHF_3 with Ar/O_2: Very strong fluorocarbon passivation resulting in blockage and deformation of the holes. Adding Argon or O_2 balances the fluorocarbon deposition, but no satisfying results were obtained.
- SF_6 with CHF_3: Adding CHF_3 into SF_6 reduces the etch rate due to passivation, also on the ZEP-520A sidewalls.

A reduction of the sidewall angle from about 17° to 14° was achieved by adding 10 sccm CHF_3 into 10 sscm SF_6 and lowering the pressure from 5.9e-2 mbar to 2.5e-2 mbar while keeping the power constant at 20 W with the results shown in Figure 6.10 (c). A further reduction of the sidewall angle was not possible, probably due to backscattered ions on the GaAs surface. The origin of the increased sidewall angle is related to the constant widening of the holes in the soft-mask during the etch: After the development, the sidewalls of the holes in the soft-mask are straight, but at the end of the etch, the holes clearly show a sidewall curvature (Figure 6.10 c). This curvature, or hole widening, is most likely caused by backscattered ions from the resistant GaAs surface. In summary, this means that the widening of the holes – induced i.e. by backscattered ions – is gradually transferred into the top-edge of the hard-mask, thus causing sloped sidewalls. This is the reason why an increase in etch time does not straighten up the sidewalls. Etch tests of TiO_x on Si substrate do not show sloped sidewalls, probably due to the continued etch into Si and therefore a reduction of the backscattered ions causes less resist deformation. Sloped sidewalls of TiO_x holes on GaAs might be minimised in the future by using different gases with improved chemical etching of TiO_x which result in a stronger lateral etch inside

the holes. The true cause of the sloped sidewalls is the increased rate of ions hitting the lower edge of the sidewall during the CAIBE etch, causing mask erosion.

Once the hole-profile of the hard-mask has been optimised, the CAIBE etch can be performed. As a reminder, we have to balance physical and chemical etching because only the balance results in fast etching of highly anisotropic features with low surface roughness. Keeping the pressure low – 4.2^10^{-4} mbar – requires us to reduce the Argon and Chlorine flow to 20 sccm Ar and 18 sccm Cl_2, which also yields a lower etch rate [Avary02]. The beam voltage was kept at 500 V with 125 V acceleration voltage and the current was reduced to 6 mA in order to minimise mask erosion. With a substrate temperature of 100°C, the holes showed high degree of chemical etching with wide hole and rough sidewalls (Figure 6.11 a).

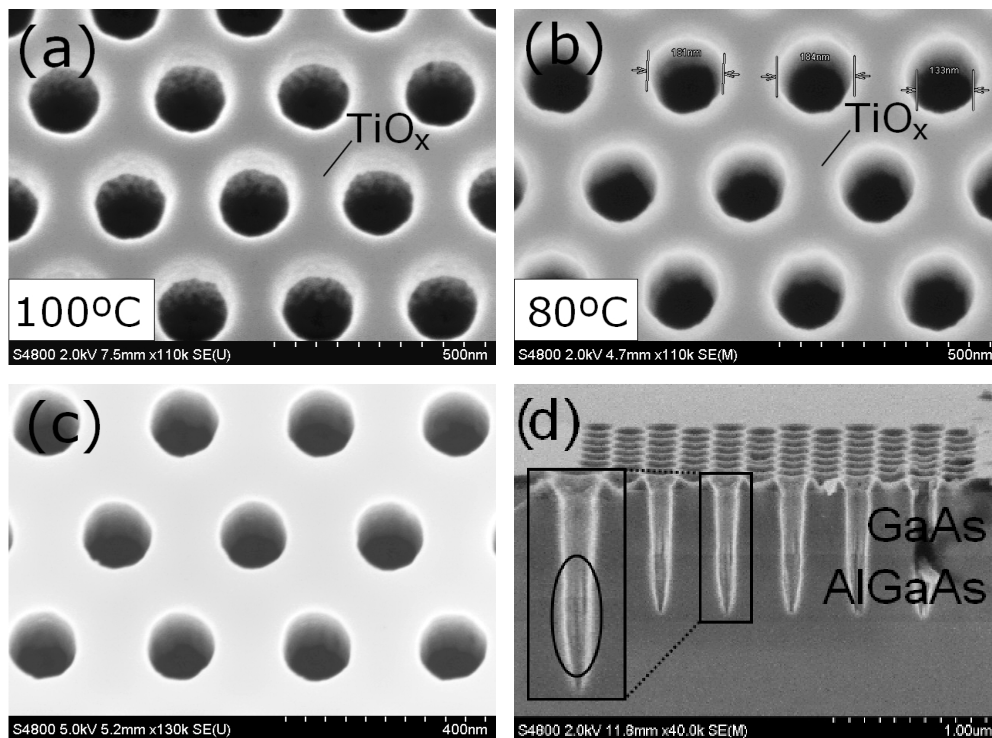

Figure 6.11 CAIBE optimisation with fixed 20 sccm Argon and 18 sccm Cl_2 flow rates, 500 V beam voltage and 6 mA current at 4.3^10^{-4} mbar for 10 min. Reduction of sidewall roughness by lowering the substrate temperature from 100°C in (a) to 80°C in (b). After the hard-mask removal the holes are nearly circular at the top-surface and irregular at the bottom surface (c). Cross-section reveals long trenches along the sidewall (inside the ellipse), mainly concentrated at the GaAs/AlGaAs interface.

Etching at high temperatures of up to 120 °C is mainly used when high etch rates in GaAs are required [Dienelt01]. It was shown, however, that surface roughness, in GaAs PhC, is low when lower temperatures are used [Choi05], [Ikeda07]. This is also observed here by comparing the etch at 100 °C (Figure 6.11 a) with another at 80 °C (Figure 6.11 b), where the latter case shows a significant reduction in surface roughness. This can be explained by the fact that our physical etching at low current requires low chemical etching at only 80 °C.

After the hard-mask removal, nearly circular holes with smaller diameters of 120-150 nm are obtained at conditions after Figure 6.11, but looking down the sidewalls of the holes in Figure 6.11 (c) we can make up irregular shapes at the bottom of the holes. The irregularities look dramatic under the tilted top-view, but cleaving through the holes reveals a high aspect-ratio (Figure 6.11 d). The location of these trenches – indicated in the circle – is mainly at the GaAs/AlGaAs interfaces, apart from a few long trenches that are caused by mask erosion. The short trenches are also observed in a colleagues work [Moore08] that indicates a general problem with the dry-etch system. There is not much we can do against it, but if we consider that the peak of the Gaussian intensity distribution of the optical mode is close to the centre of the GaAs slab, we can accept the trenches because they are only overlapping with the tails of the intensity distribution. The etch in Figure 6.11 (d) was performed for 10 min, resulting in an average etch rate of about 80 nm/min. Increasing the etch time to 12 min extends the depth of the holes while still maintaining a good hard-mask quality, resulting in straight, deep holes with 150 nm in diameter (Figure 6.12 a). In order to create the oxide cavity, the hard-mask needs to be removed first followed by a wet-oxidation step. Repeatability of the oxidation process is very important so that a native oxide removal step in 1:5 (NH_4OH : H_2O) is performed and the oxidation parameters followed strictly resulting in an oxidised AlGaAs layer shown in Figure 6.12 (b). In contrast to a successful oxidation, Figure 6.12 (a) shows a failed oxidation with an oxidised AlGaAs region only around one hole. The oxidation step is only necessary for the oxide cavity, whereas the membraned cavity only requires dissolution of the AlGaAs layer in 1:1 HCl : H_2O for about 70 s. Followed by a hard-mask removal based on the presented back-infiltration where the process parameters are not critical because the AlGaAs is already

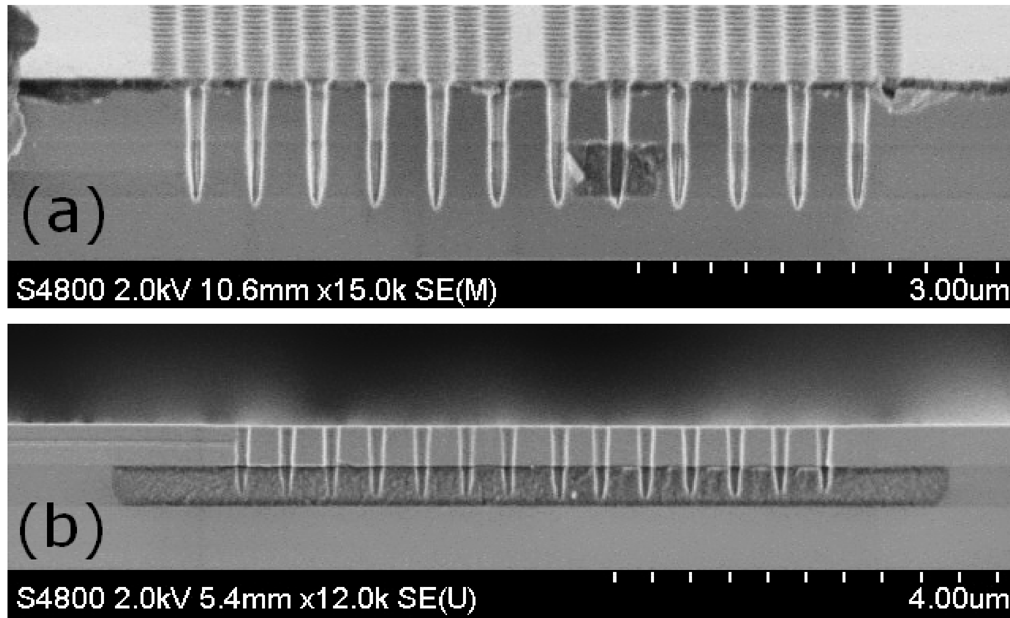

Figure 6.12 PhC holes (a) after 12 min etch time with the hard-mask still on top of the surface. The darker region around one hole shows a sign of failed oxidation. End of fabrication steps with etched PhC holes (b), removed hard-mask and successful oxidation for 20 min, 400 °C sample temperature, 80 °C water reservoir temperature and 300 sccm N_2 gas flow.

removed.

Having successfully fabricated narrow and deep PhC holes for the membraned structure as well as the oxide structure the samples can now be optically characterised.

6.2.2 Optical Characterisation of PhC Cavities

The fabricated cavities are next characterised to assess their Q-factors, the resonance wavelengths and to look for lasing.

Two different types of characterisation techniques can be used to characterise PhC cavities: *in-plane* and *out of-plane coupling*. In-plane measurements are used to obtain Q-factors and resonance positions of cavities peaks for *passive* devices by i.e. coupling a laser into a waveguide that is leading to the cavity. Measurements of *active* devices are usually performed by pumping the cavity and collecting the signal out of-plane by a Micro-Photoluminescence setup (μPL). In the μPL setup, the cavity is pumped with a wavelength shorter than the band-edge; hence carriers are generated and

recombine in the QDs while emitting light. High intensity – or high photon flux – can result in a high amount of carriers being generated, which increases optical absorption loss. Pumping directly the wetting layer of the QDs, above the band-edge, helps to keep the free-carrier concentration low, but this configuration is less flexible in terms of material composition because for different wetting layer materials, different pump wavelengths are needed.

We aim to characterise active device and therefore the μPL setup is most suitable because it separates the pump and emission wavelength by dichroic mirrors, hence increasing the signal-to-noise ratio. There was no setup available to perform this

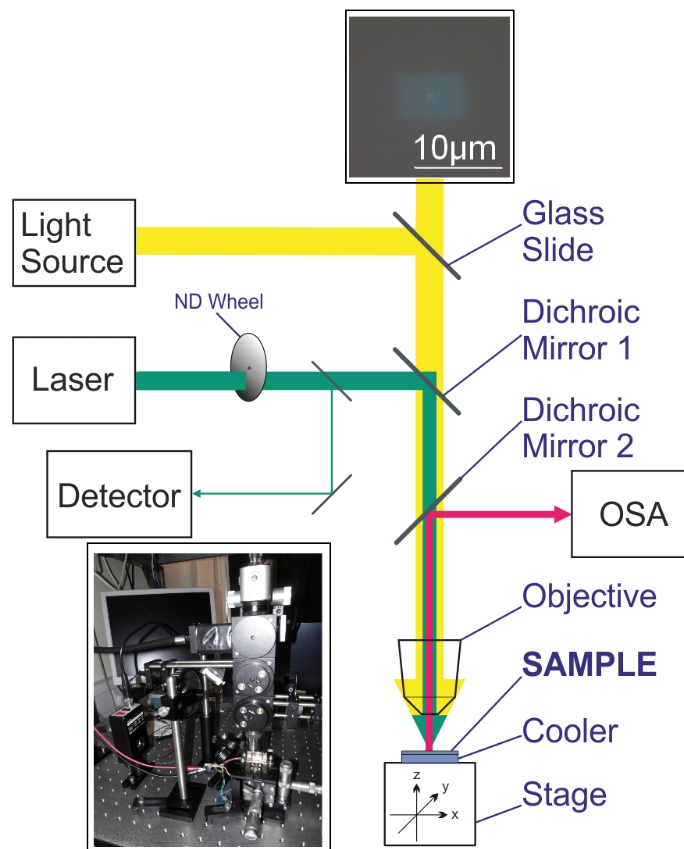

Figure 6.13 μPL setup for PhC cavity characterisation. A red laser [780 nm, 70 mW max.] is focused onto the sample, the emission is collected through the same objective and analysed. The excitation power can be changed via the ND filter wheel and is detected via the reference arm and the self-calibrated detector. The position of the excitation spot, relative to the cavity, can be observed with the camera (top-inset) and adjusted through the x-y-z stage with mounted Peltier cooler and the sample. The compactness of the setup is shown in the photograph (bottom-inset).

kind of measurements so I designed and built this µPL setup shown in Figure 6.13. Here, the excitation laser – 780 nm laser diode with 70 mW power driven by Agilent 8114A pulse generator – is collimated and passed through the 100X objective. The collected emission, is reflected by the second dichroic mirror that has high reflection for the emission wavelength and high transmission for the pump. It is then coupled into a fiber leading to either the optical spectrum analyser or the monochromator with an InGaAs detector. In order to control the power of the excitation pump, an ND filter wheel was inserted into the beam line, which is monitored via a detector.

6.2.2.1 Membraned Ln-type and Gentle Confinement Cavities

The first cavities that were measured with this setup are membraned Ln-type cavities with 5, 7 and 11 missing holes including a Q-optimisation by shifting the two nearest-lateral holes after shown in section 3.2.1 "Intrinsic Q-factors for different Types of Cavities". The cavities were pumped with a duty-cycle (dc) of 30% (1 kHz repetition rate) and a average power of about 1 mW over a pump spot of a few micrometres. The dc and the power had to be this high otherwise no signal was detected with the OSA. Two types of fibers were tested for highest collection signal and lowest resolution: Graded-Index-Fiber (GIF) with 62.5 µm core diameter and NA of 0.275; Multi-Mode-Fiber (MMF) with 400 µm core diameter and NA of 0.37. To maximise the coupling efficiency, the NA of the collecting fibre has to be equal or higher to the NA of the corresponding lens. The fiber collimator has an NA of 0.24 to facilitate coupling. Nevertheless, the signal of the MMF was about 5x higher than the signal out of the GIF. Despite the lower power for the GIF, this type was chosen because of its higher spectral resolution when connected to the OSA, according to the manual of the OSA

The broad spectrum of a L11 cavity is shown in Figure 6.14 (a) with the cavity peaks clearly visible. Reducing the hole-diameter results in a red-shift of the resonance wavelength because the effective mode index increases. The QD emission peaks at about 1210 nm and the best agreement between gain peak and cavity resonance occurs for the cavity with r/a = 0.277. This peak was then scanned with a higher resolution in order to obtain a more accurate value for the Q-factor (Figure 6.14 b and c). The lowest useful resolution was 0.2 nm, which is limited by the noise level.

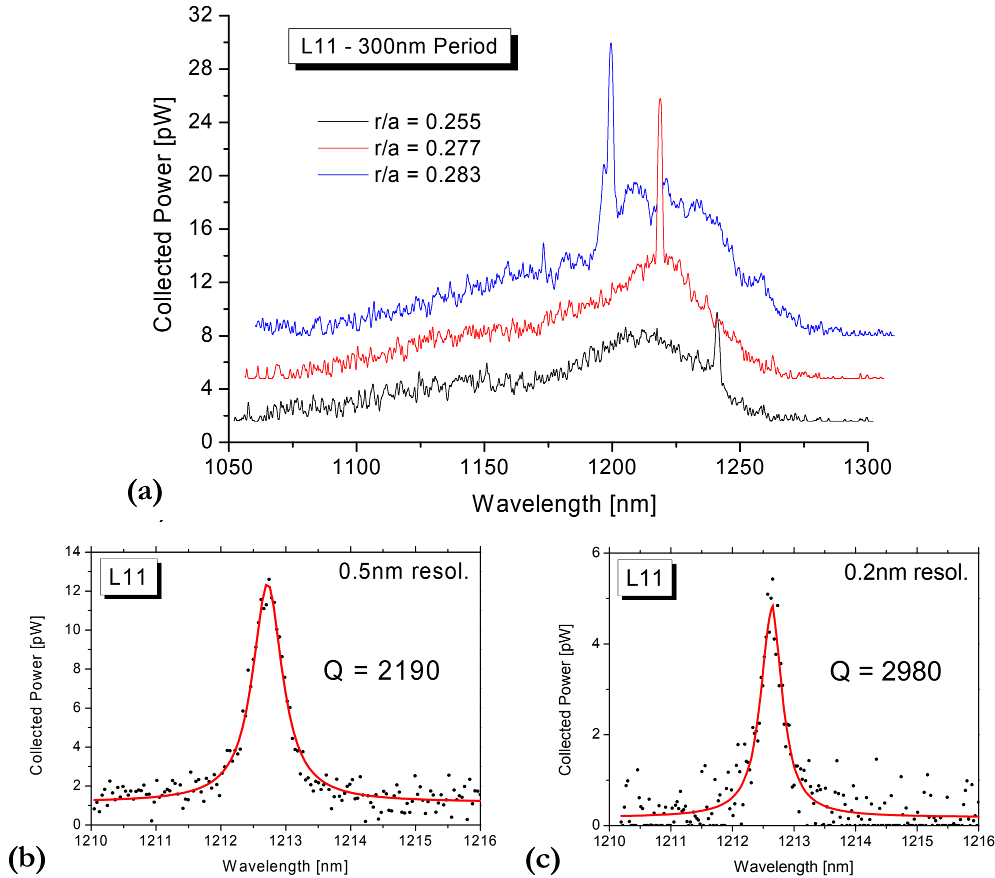

Figure 6.14 Broad spectrum (a) of membraned L11 cavities with strong cavity peak emerging form the QD background. The peak is red-shifted as the hole-diameter is reduced and overlaps with the emission maximum of the QD at r/a = 0.277 (Please note that the background level is zero and it is only shifted for illustration purposes). This peak is further scanned with a resolution of 0.5 nm (set in the OSA) giving a Q-factor of 2190 (b) and with 0.2 nm resolution giving a Q-factor of 2980 (c). The OSA over-samples in order to obtain more fitting points.

The low signal-level limits the measured Q-factor for the L11 cavity to **2980**. This means that the real Q-factor is higher then this value. Q-factors measurements of the fundamental mode of the L7 and L5 cavity gave **1680** and **1540**, respectively – with a coarse resolution of 0.5 nm, again limited by noise. These are respectable values given that the cavity is actively pumped, and free-carrier absorption is present. Here, we use a 5 layer stack of high density InAs QDs that are a source for increased scattering as well as re-absorption of the emitted light [Tawara08]. In general, the higher the QD density, the lower the Q-factor; Q-factors of a few 10.000's can only be obtained by using very low QD densities [Nomura10]. From this point of view the Q-factor we have obtained for the L11 is high, but we will

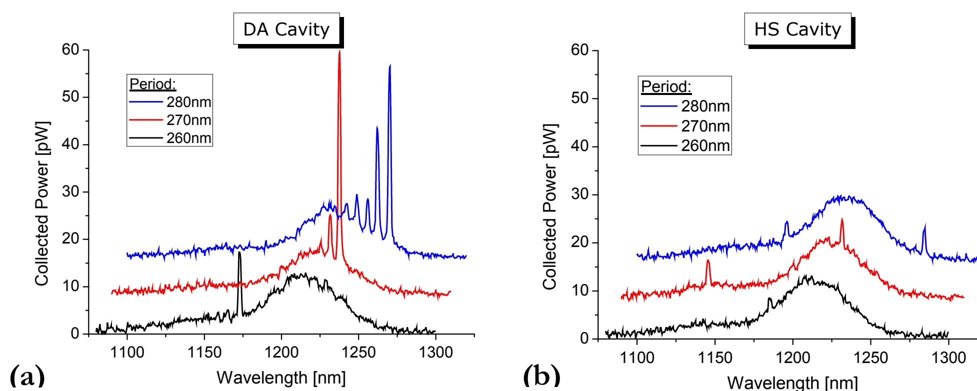

Figure 6.15 Comparison between DA (a) and HS (b) cavity on membrane for three periods of 260 nm, 270 nm and 280 nm. The r/a ratios for the DA and HS 0.223 and 0.234, respectively. Please note that an offset in X an Y was introduced to distinguish between the curves.

investigate whether it is possible to achieve even higher Q's by using a different type of PhC cavity such as a gentle confinement cavity.

Gentle confinement Cavities

For this purpose we have fabricated two types of cavities: *hetero-structure* (HS) and *dispersion adapted cavity* (DA). In the case for the DA cavity we only used the type with the first hole-shift of h_0 = 30 nm. A comparison of the cavity spectra for two different periods is shown in Figure 6.15.

As expected, the peaks shift according to the change in period, which is a feature of the scalability of the PhC properties. The DA cavity has a much smaller free-spectral range of a few nanometre's where the next higher order mode in the HS appears in about 100 nm distance[1]. The most distinct difference between the cavities is the height of the peak, keeping in mind that the pump power is the same in all case as also indicated by the QD background level. The height of the peak – enhancement over the background – is related to several factors [Fujita08], however, with main contribution of the cavity emission coupled to the objective (coupling efficiency)

[1] When the pump power was too high a mode appeared at shorter wavelength only a few nanometres away from the fundamental mode. This was an irreversible effect as this mode could also be seen at low pump power after the high power illumination. Local oxidation of the centre cavity region might be responsible for the additional mode.

and the Q-factor. The enhancement is higher for higher Q-factors due to an external efficiency term and the Purcell enhancement. The low signal of the HS cavity prohibited an accurate measurement so that we measured Q-factor of **3050** for 0.2 nm resolution. For the DA cavity, however, we obtained Q-factor of **3316** with 0.05 nm resolution. Using the DA cavity with the smallest hole-radius of 0.218 at 260 nm period we have measured a maximum Q-factor of **3950.**

Because both cavities have similar Q-factors, the difference in peak height can not be explained by the Q-factor. Therefore, the efficiency of the cavity coupled to the objective might qualitatively explain the peak heights. In general, a gentle confinement cavity can reach high Q-factors by reducing the light emission out of the cavity. This, on the other hand, is in disfavour with the principle of the measurement setup – that is light collection out of the cavity. It is most probably the case that the emission of the HS cavity does not couple to the objective as much as the DC cavity does. We can check this by comparing the far-fields components of both cavities shown in Figure 6.16. The angular distributions show how much radiation is emitted in particular directions with perfect vertical emission at 0, 0. When using an objective, vertical emission is desirable so that, theoretically, more radiation should be collected out of the DA cavity than the HS cavity. This explains the higher signal obtained from the DA in the experiment and is a clear advantage of

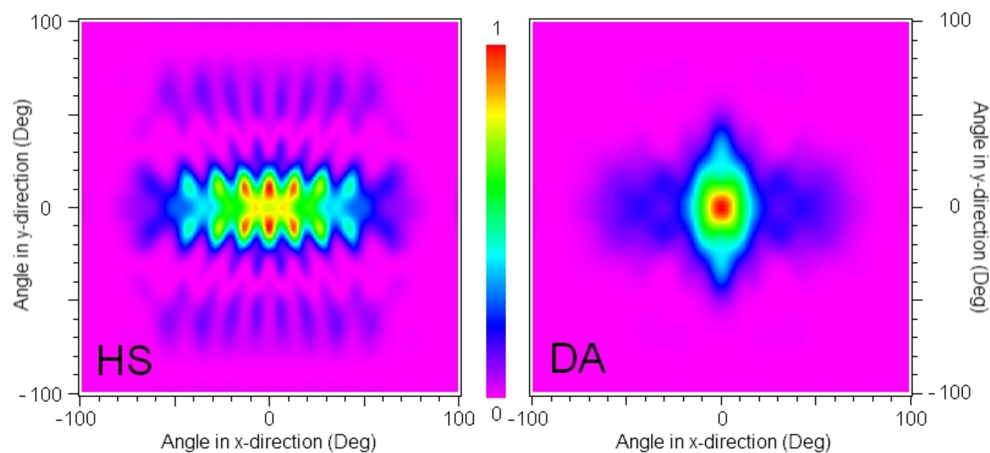

Figure 6.16 Angular distributions of the far-field components obtained via Fourier-transform of the electric-field perpendicular to the cavities. The angular spread of the normalised real part of the Fourier-component is larger for the HS cavity than for the DA cavity.

the DA where high Q-factors and high coupling efficiencies can be obtained simultaneously.

6.2.2.2 Gentle Confinement Cavities on Oxide

The Q-factor for the membraned cavities is very high, so that we now measured the Q-factor for the oxide configuration. This is important because we aim to use the oxide cavity with their improved thermal and mechanical properties in the electrically injected device. Let us now investigate what is the highest Q-factor we can obtain with the DA cavity. We use the DA cavity here because of its higher signal. Measured Q-factors with a resolution of 0.05 nm for two periods are depicted in Figure 6.17. As expected the Q-factor increases with decreasing hole-diameter and reaches values as high a **2200**. When comparing the periods, is seems that both curves are separated by an offset in hole-diameter so we can confirm that for reaching high Q-factors it is important to have small r/a ratio and not only a small hole-diameter. This can be seen for the two points with the highest Q-factors for each period as they peak at different hole-diameters, however, the r/a ratio is the same. Comparing the value of 2200 for the oxide with 3950 for the membraned DA cavity the Q-factor drops to about a half when using oxide underneath the slab. On

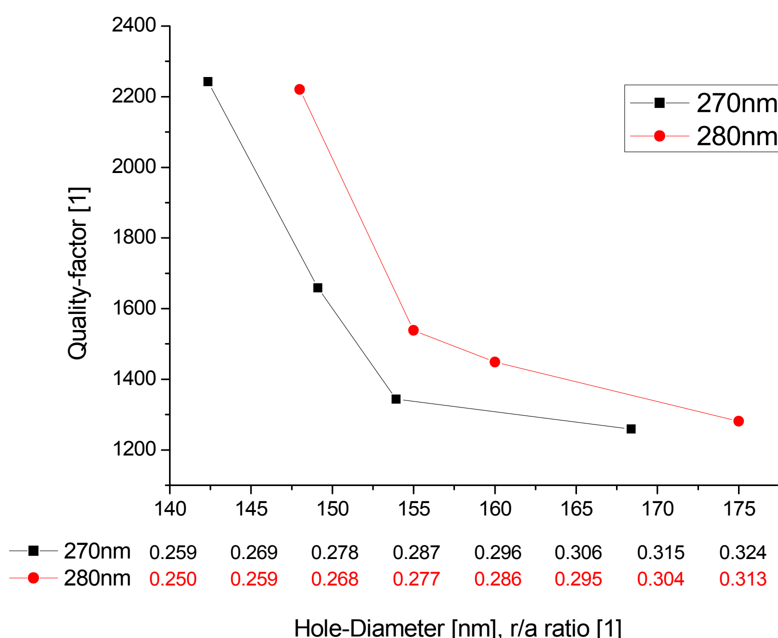

Figure 6.17 Q-factor dependence on hole-diameter for AC cavities (h_0 = 30 nm) with 270 nm and 280 nm period. The lower rows under the x-axis represent the calculated r/a ratio from the hole-diameter for the corresponding period.

the other hand, the r/a ratio of 0.259 used for the oxide is much higher than the 0.218 for the membrane – probably due to unexpected problems during the CAIBE etch – and should increase even further with smaller r/a. Nevertheless, this value of 2200 is remarkable for a PhC with 5 layers of high density QDs with oxidised AlGaAs layer and probably the highest reported so far. This is mostly due to the hard-mask removal technique, because only with this technique we can apply a hard-mask – necessary for deep and narrow high-quality holes with high Q-factors – and remove it without damaging the PhC or dissolving the high Al-content AlGaAs layer. Published cavities on oxidised AlGaAs are rare and Q-factors low as in [Yoshie04] where a L1 cavity with a = 330 nm and r/a = 0.30 reached a Q-factor of 300. There, the holes are 600 nm deep and etched in a CAIBE through a PMMA soft-mask.

Coupling Improvement by Far-Field Optimisation

In the previous measurements the coupled signal from the HS cavity into the objective was low, therefore we now apply a far-field optimisation technique [Tran10], [Portalupi10] that improves the directionality of the cavity emission. Gentle confinement cavities are specialised to reduce the field components within the light-cone, minimising the out-of plane emission and increasing the Q-factor. This far-field optimisation technique, back-folds the k-space peak at the Brillouin zone back into Γ (Figure 6.18 a), increasing the emission and also lowering the Q-factor. Fortunately, this is a sacrificial loss because the emission is vertical unlike the emission out of the unmodified cavity. We use a second periodicity in the second row of holes by enlarging every second hole by a certain amount (Figure 6.18 b). With enlargement of these holes by 3 nm, 6 nm and 9 nm, the peak rises and a slight red-shift is observed for the DA cavity in Figure 6.18 (c). (The cavity with 3 nm enlargement appears to have another fault, hence does not fit into the trend). In this oxide sample, a peak for the HS cavity was not visible without any optimisation (0 nm) and it emerges when the holes are enlarged to 6 nm and 9 nm (Figure 6.18 d). Also this sample confirms that more light can be collected from the DA cavity than the HS cavity and the far-field optimisation helps to improve the collection. This was not sufficient in order to obtain a signal from the HS for a Q-factor measurement.

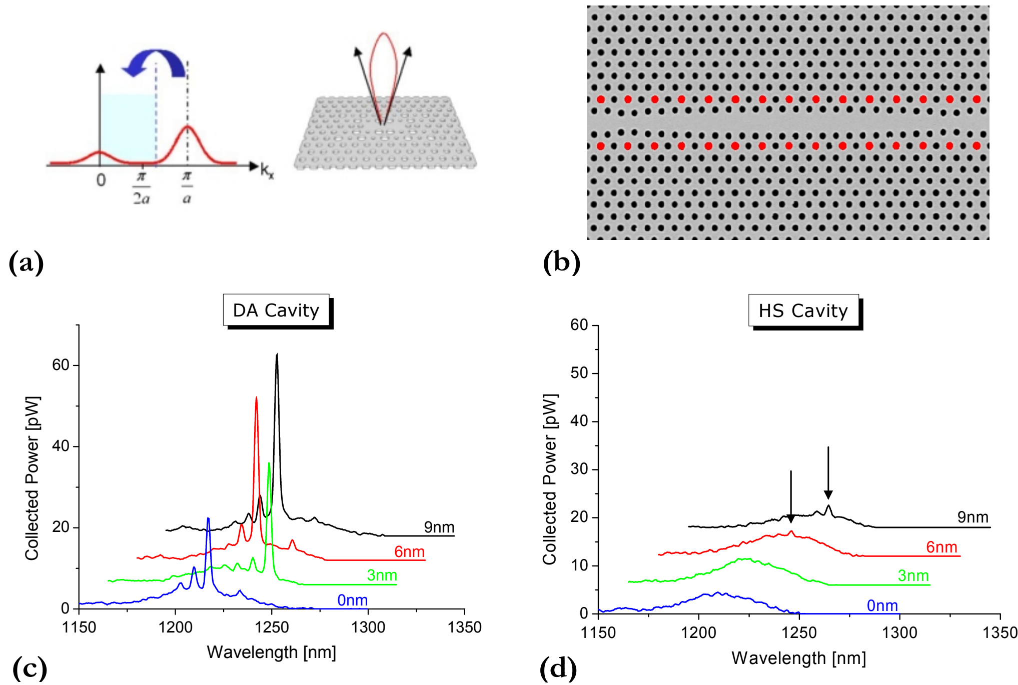

Figure 6.18 Far-field optimisation technique, by folding the peak in k-space back into Γ (a) [Tran10][9] and therefore increasing vertical emission. The back-folding is accomplished by overlaying a second periodicity ((b), red holes are enlarged) in the second row of holes. Spectra for different values for the hole enlargement in the case of the DC (c) and HS (d) cavities with r/a = 0.25.

6.2.2.3 Towards Lasing

The work presented in the previous section was necessary in order to confirm that it is possible to fabricate PhC cavity out of this material and characterise the cavities for the resonance wavelength and the Q-factor. We also confirmed that the spontaneous QD emission was responsible for the visibility of the cavity peak. Now, we will investigate whether *lasing* via optical pumping can be observed. Our Q-factor of **2200** for the oxide cavity is comparable with other 5 layer QD PhC cavities where lasing was achieved [Yoshie04], [Nomura06] and **3950** for the membrane is even higher so that lasing appears to be possible. In order to observe lasing, we use the membraned cavity with the higher Q-factor and therefore we have use short pulses in order to keep the generated inside the slab at a minimum. Heat is a general problem of slabs that are fully surrounded by air and the membraned cavities require the pump pulses to be reduced to a maximum of 100 ns and a maximum

duty-cycle (dc) of about 10% [Giannopoulos10]. The diode laser used for the pumping is fully capable of delivering such short pulses, in fact, we have managed to obtain 10 ns short pulses. For these measurements we use a monochromator with an InGaAs detector that has the ability to set the integration time and therefore allows to measure short pulses with low dc is necessary because we have to use low pump powers in order to determine the lasing threshold in case the devices are lasing. Using the monochromator we can not set the resolution directly, but we can set the width of the exit slit and so restrict the spectral spread with again the draw of having a low signal. Therefore, a slit-width of 400 μm resulting in a resolution in about 0.1 nm was chosen in order to maintain a good signal-to-noise ratio.

We are now looking for the main signature of the lasing process, namely the clear kink in the input-output curve. The pulsed experiments are carried out on the samples already shown in Figure 6.15 with peak at the maximum of the QD ground-state emission of about 1210 nm. The spectral evolutions as a function of pump power are shown in Figure 6.19. Increasing the pump power leads to an increase of the QD background and the cavity peak (Figure 6.19 a, b), however, no rapid increase of the output peak it observed. A close to linear increase of the output power dependent on the input power (Figure 6.19 c, d) is observed confirming the non-lasing behaviour. The slope of the DA cavity is steeper than the HS indicating a higher overall efficiency probably due to a higher Q-factor of the DA cavity. When pumping with powers above about 1 mW, a decrease in efficiency is observed and the curves start to saturate. This is caused by either the increase of free-carrier absorption or a temperature increase and hence a decrease of the QD efficiency. A distinction between both can be made by observing the peak shift because free-carrier blue-shifts and the high temperature red-shifts the peak. Here, however, we did not observe a shift in neither of the directions and therefore it might be a combination of both. Further attempts were made by re-positioning and re-focusing of the spot to ensure that a larger PhC region is pumped so that the PhC mirrors become non-lossy, but again with no signs of lasing. Other cavities with different peak positions and Q-factors were pumped and even the pulse duration and repetition rate were changed with little effect. It was noticed that the peak enhancement over the QD background was the highest with a maximum dc of 10%

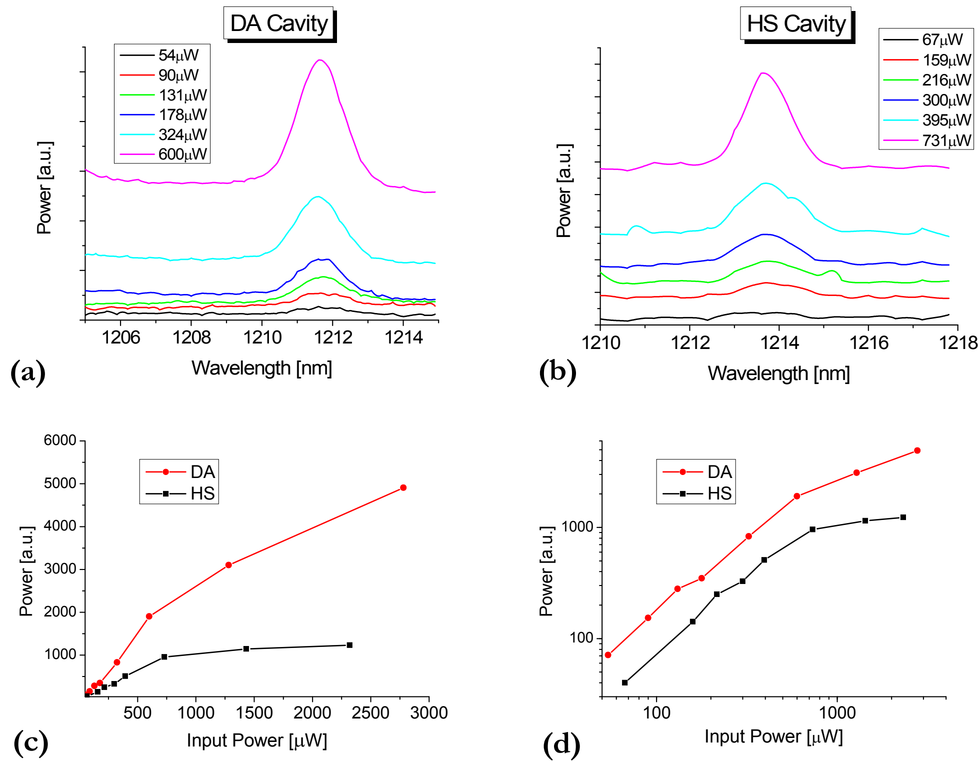

Figure 6.19 Pulsed pump excitation of membraned cavities with 20 ns pulsed at 1 us repetition period – dc ~ 2%. Spectral evolution of DC cavity (a) with 270 nm period, r/a = 0.265, Q ~ 3000 and HS cavity (b) with 270 nm period, r/a = 0.26 and an estimated Q ~ 3000. Output vs. input power in linear (c) and log-log scale (d) of the integrated peaks after (a) and (b).

and pulse duration between 20 ns to 50 ns. The maximum enhancement was with a factor of 2 for both, the DC and HS cavity lower than in the previous Q-factor measurements. No reasonable answer was found for this expect a different data acquisition of the OSA i.e. cw measurement mode with lock-in amplification. A major issue with these devices is the strong *Surface-recombination* which is a real problem especially in GaAs based PhC devices because 1) the surface-recombination velocity in GaAs is about one to two orders of magnitude higher than in InP systems [Coldren95] and 2) PhC have a high surface-area where recombination can occur. Previous work established that the surface-recombination velocity is lower in QDs than in QW's [Moore06] and is usually not a problem in devices with QDs because numerous optically pumped PhC laser are published. The origin of the surface-recombination lies in the dry-etch process that disrupts surface states and leaves dangling bonds behind. Sulphur treatment can produce a

passivation layer and thus reduce the surface-recombination velocity in general GaAs surfaces [Ohno91] and for InGaAs/GaAs quantum-well lasers [Englund07]. We therefore dipped our sample in Ammonium-Sulfide solution and air-dried it, but again no lasing was obtained showing that surface-recombination is not the limiting factor in the recent samples. Although we are using 5 layers of high density QDs the gain might not be sufficient to overcome the losses

Next, we use the first excited state as it provides higher gain. The peak position of the excited-state is obtained by pumping an unprocessed region when the peak arises after the ground-state has saturated shown in Figure 6.20. As expected, the excited-state rose above the level of the ground-state when pumping was sufficiently high. A DA cavity with a Q-factor of about 3000 was found that closely matching the excited-state position (Figure 6.20 b) of the QDs. While increasing the pump

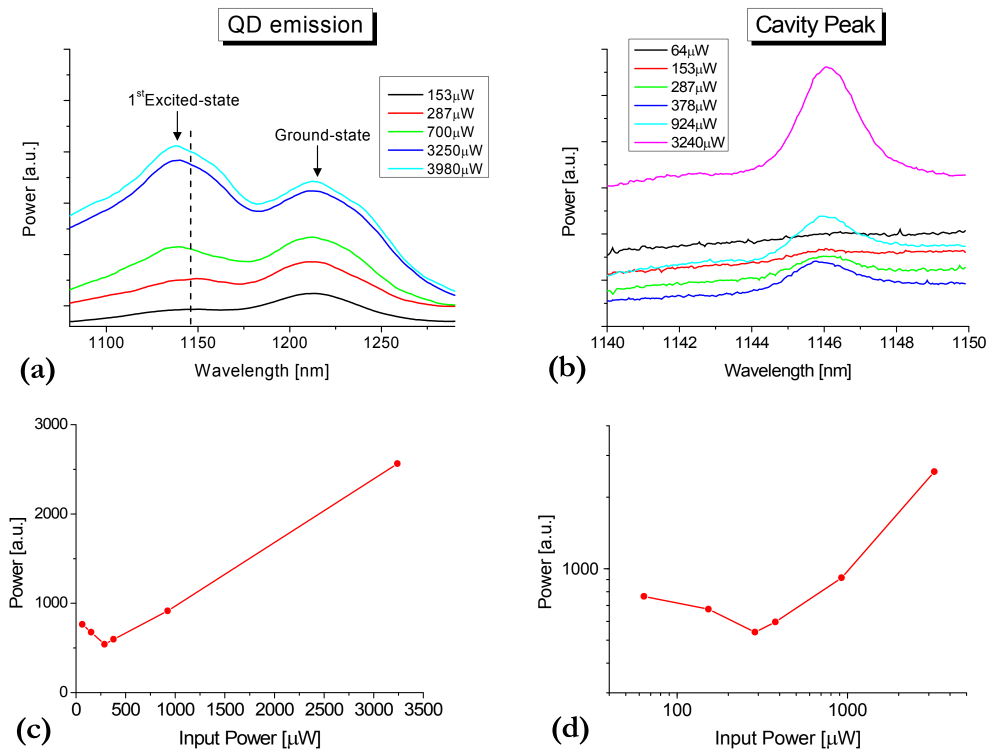

Figure 6.20 Test for 1st excited-state lasing. Emission spectrum of QDs at different pump power with the 1st excited-state (peak at about 1140 nm) rising above the ground-state level (a). The dashed vertical line represents the peak position of cavity used in (b) with a period of 260 nm and r/a ~0.265 giving a Q-factor of about 3000. Pumping conditions in both cases are 20 ns pulse duration, 1us repetition period – dc ~ 2%. Output vs. input power in linear (c) and log-log scale (d) of the integrated peaks after (b).

power, the peak emerged from the background and surprisingly the background emission decreased until about 378 µW it starts to rise again. Comparing this to the case where the cavity peak overlapped with the ground-state, the background increased monotonous with the pump power (Figure 6.19) opposite to the behaviour of the excited-state. This unusual behaviour also reflects in the output-input characteristics (Figure 6.20 c, d) where the output power first declines and then increases linearly with no clear indication of a lasing threshold kink. Furthermore, no saturation of the output power is present in contrast to the ground-state situation in Figure 6.19. Unfortunately, no other cavity had a peak in the region of the excited-state to confirm or dismiss this behaviour. A decrease in emitted power means that less power is either collected or emitted. Modification of the of emission properties of the PhC alone, which affects the collection, is not thought to cause this behaviour and this does not happened for the ground-state. A main difference between the excited-state and the ground-state is the high degree of optical absorption due to re-absorption of the light that is at higher energies than the ground-state of the QDs. As possible explanation might be that in presence of the PhC the absorption is modified so that the signal first decreases and then overtakes the absorption. Nevertheless, the cavity peak is rising at a higher rate than the background but it never becomes dominant as we would expect it for a lasing mode. The maximum gain is higher in the excited-sate than in the ground-state, but probably the high degree of loss due to re-absorption or free-carrier-absorption inhibits lasing.

Oxide cavities at ground-state were pumped as well, but no lasing was observed either. Because they have a lower Q-factor than the membraned cavities it is less likely that the oxide cavities show lasing.

In summary, we have successfully fabricated PhC cavities with Q-factors of up to about 4000 for membrane and 2200 with an oxide layer. Comparable cavities published in literature have reached lasing under similar pulsed excitation, but we did not observe a dominance of the cavity peak over the QD background that is characteristic for lasing. In numerous attempts where we have improved the device conditions, no threshold was reached despite having 5 high density DWELL layers.

Pumping at low temperature might have shown the actual problems of these samples, but a cryogenic realisation of the set-up was not possible. Due to time restrictions, we had to leave the optical pumping behind and concentrate on the fabrication of the electrically pumped device.

6.3 Fabrication of ePCL

In this section we discuss the fabrication steps and present the final device. The device builds on the work of previous chapters such as the design, the fabrication of the stripe-device, and the fabrication of the photonic-crystal cavity including hard-mask removal. The fabrication steps were already developed in these chapters, so that we do not need to go into detail here. Appendix A, however, provides further processing details to the interested reader.

The overview of the fabrication process is shown in Figure 6.21, starting with the PhC cavity. At first, a 120 nm thin TiO_x hard-mask needs to be evaporated on a clean sample (Figure 6.21 a). In order to define the PhC pattern, the electron-beam sensitive resist ZEP-520A is spun on the sample and dried on a hot-plate, resulting in a 375 nm thick layer. The electron-beam writer transfers the PhC design-pattern into ZEP-520A and the sample is then developed in Xylene for 45 s, removing the exposed PhC holes. The first step of the two-step dry-etch process is the PhC transfer from the ZEP-520A into the hard-mask by Reactive-Ion Etching (RIE). Two gases, CHF_3 and SF_6, are used with a ratio of 10 sccm : 10 sccm to etch the hard-mask with 20 W of power at 2.5×10^{-2} mbar for 65 s, resulting in fully etched holes. The remaining ZEP-520A is then removed from the sample by soaking it in 1165 solvent at 60°C for about 1 h. The GaAs etch is performed in the Chemically-assisted Ion-Beam Etcher (CAIBE) with 20 sccm of Argon, 18 sccm of Cl_2, a beam voltage of 500 V, 6 mA of beam current, at a pressure of 4.3×10^{-4} mbar, while the sample temperature is kept around 80 ºC. Etching for 12 min results in an etch-depth of 800 - 900 nm, reaching the bottom of the AlGaAs layer. In the following step, the hard-mask is removed by back-infiltration of the PhC holes and a wet-etch in hydrofluoric-acid, preserving the AlGaAs layer (Figure 6.21 b). Prior to the wet-oxidation, the sample is dipped in ammonium-hydroxide to remove the

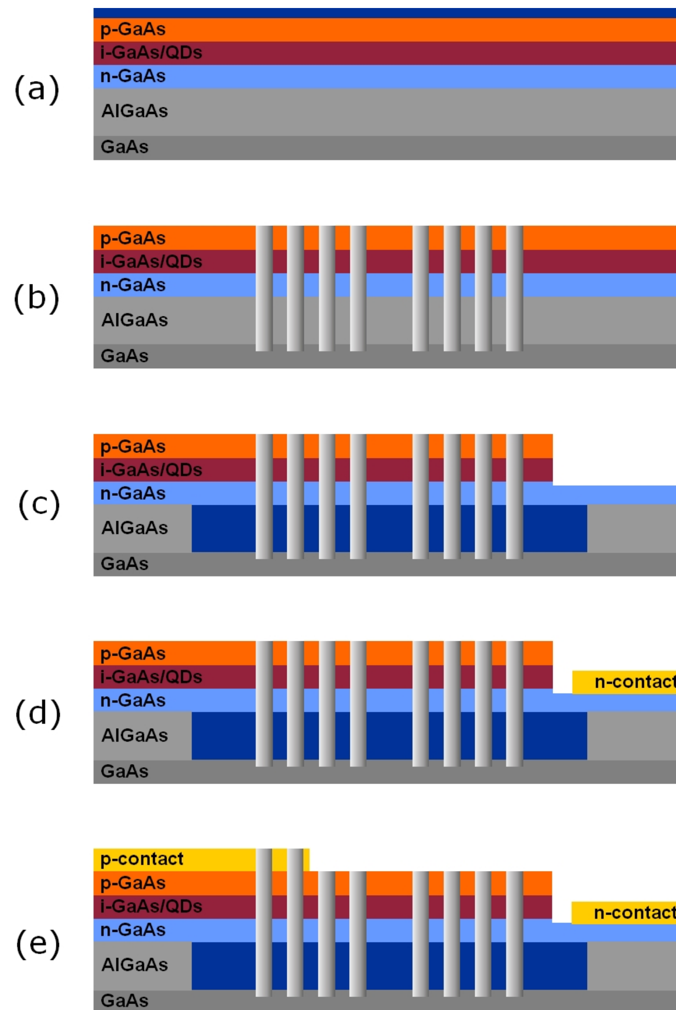

Figure 6.21 Cross-sections of the main fabrication steps of the electrically injected device. The TiO_x (blue layer) evaporation on the sample (a) is followed by the PhC etch and the hard-mask removal (b). The AlGaAs layer is partially oxidised and the wet-etch to the n-GaAs is performed (c). Next, evaporation of the metal-contact on n-GaAs (d), followed by the metal-contact on p-GaAs (e), resulting in the finished device.

native oxide. Wet-oxidation is then performed in a steam atmosphere at 450 °C sample temperature for 20 min. A low index Aluminium-Oxide (AlOx) layer is the created below the cavity. In order to inject electrons into the structure, a wet-etch is used to reach the underlying n-GaAs layer. Controlled wet-etch steps in a phosphoric-acid/hydrogen-peroxide/deionised water solution result in a remaining 80 nm high n-GaAs layer (Figure 6.21 c). Efficient carrier injection into the n-GaAs needs a special ohmic-contact recipe consisting of 14 nm Au, 14 nm Ge, 14 nm Au, 11 nm Ni and 100 nm Au that is evaporated with an electron-beam evaporator (Figure 6.21 d). Thermal annealing of the sample for 60 s at 425 °C results in

reduced contact-resistance. In the final step, the p-contact consisting of 20 nm NiCr and 100 nm Au is evaporated on top of the p-GaAs layer, partially overlapping with the PhC cavity (Figure 6.21 e).

SEM images of the fabricated device are shown in Figure 6.22 a. Here, the p-contact is very close to the centre waveguide, which is advantageous for the electrical properties but may be too close to the optical mode. The wet-etch exposed the n-GaAs layer and the n-contact is within the wet-etched region, about 10 µm away from the cavity centre. A close-up into the cavity centre (Figure 6.22 b) shows that the hard-mask is removed, although the surface has some residues. During the evaporation, the metal went into some of the PhC holes, introducing holes in certain

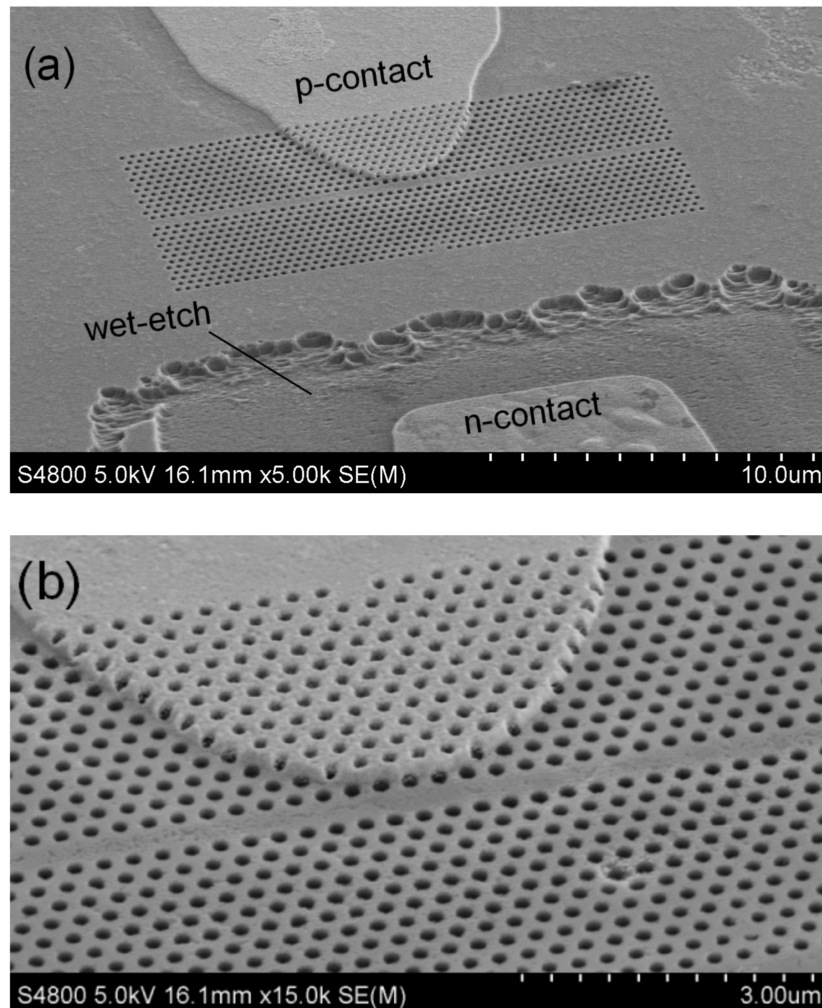

Figure 6.22 SEM images of a fabricated device with the p-contact on top of the PhC hetero-structure cavity and the n-contact on top of the wet-etched n-GaAs layer (a). A close-up into the PhC cavity (b) highlights the proximity of the contact to the waveguide and holes in the contact.

certain regions of the p-contact. A current shortcut might result as a consequence, and needs to be tested. The PhC holes, on the other hand, are circular with a radius of about 80 nm and a period of 280 nm (Figure 6.23 a). The contact has a rounded shape, in acccordance with the design in section 3.2.2, "Loss and Gain Evaluation". In order to perform a test, this sample was dipped into ammonium sulphide solution and then air-dried to passivate the surfaces inside the PhC holes. Under the setup, the gold contacts are clearly distinguished by their colour; in addition, the n-contact shows irregularities on the surface (Figure 6.23 b). These irregularities are thought to be caused by a failed annealing step where bubbles formed and some regions delaminated. As shown already in section 5.2.1, "Wafer Vn1807: ePCL Electrical Design", good contacts can be generally obtained, which, unfortunately, was not the case here. Hence, this sample could not be characterised for diode behaviour and light emission, as the measured resistance was higher than 1 MΩ.

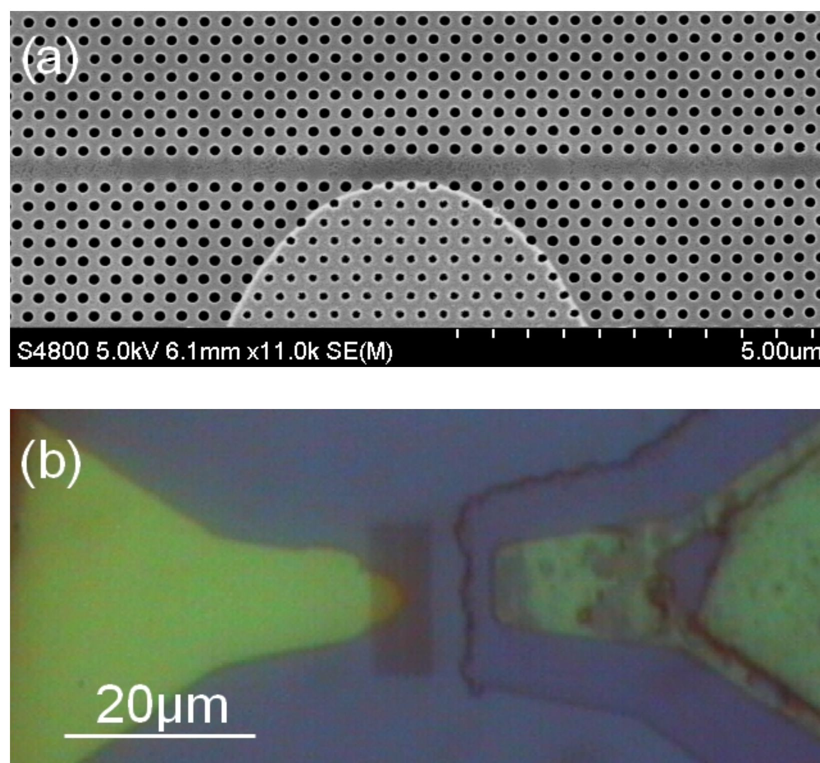

Figure 6.23 Top-view on PhC HS cavity with the round p-contact (a). The hole-radius is approximately 80 nm at a period of 280 nm. Photograph of the device with the p-contact on top of the PhC and the n-contact within the wet-etched region (b).

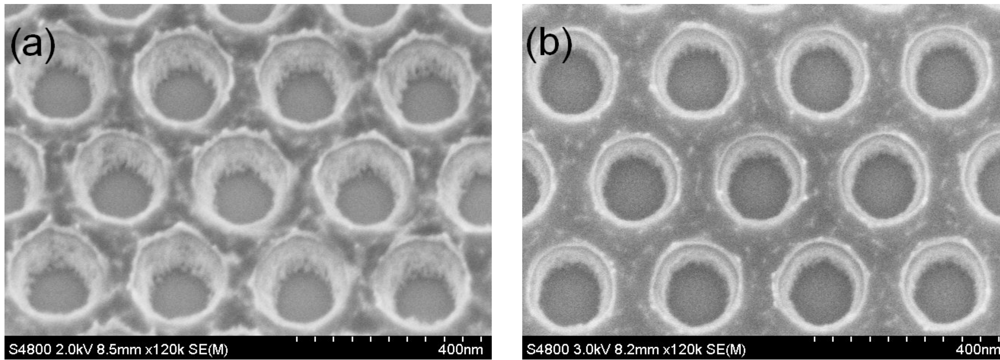

Figure 6.24 Quality difference of TiO_x hard-mask after the RIE etch depending on the evaporation rate. High evaporation rate of 0.06 nm/s (a) and a lower rate of 0.01 nm/s.

Attempts were made to replicate the sample in the last months of this project, but the quality of the TiO_x hard-mask strongly deteriorated. Numerous evaporation tests were performed to investigate the cause and the evaporation rate was identified as a possible reason for the lower quality of TiO_x. A high rate of about 0.06 nm/s shows rough and porous sidewalls (Figure 6.24 a) whereas a lower rate results in less rough sidewalls (Figure 6.24 b). This is related to the deposition process where lower rates result in denser films [Asghar06]. Apart from lower rates, also higher substrate temperatures as well as an oxygen bleed into the chamber result in denser films. Here, however, we only have the possibility to decrease the evaporation rate. This, on the other hand, resulted in an unreliable process so that samples with higher quality films could not be produced again[1] and the PhC etch inside the CAIBE was very unsatisfactory. Given the pressure of time, SiO_2 films based on flowable oxide (FOx) were tested, on increased sample sizes, as a replacement for the TiO_x films. Etch-tests inside the RIE with different FOx thicknesses for optimisation of the etch parameters were started, but could not be completed due to shortage of time.

In summary, it was shown that it is indeed possible to fabricate the complete device as designed, but because of the multiple fabrication steps and complex fabrication protocol overall, any issue such as the unreliability of the TiO_x deposition makes it difficult to fabricate devices reliably. Therefore, it was not possible to demonstrate the successful operation of an electrically injected photonic crystal laser device.

---

[1] High quality TiO_x films were fabricated in the past so that an unknown change in the evaporation system is thought to be the cause for the recent low quality TiO_x films.

Chapter 7

Conclusions

In this project, the concept of an electrically pumped photonic-crystal laser has been investigated. During this journey, the device physics has been explored, a new cavity design was developed and difficult oxide cavities were fabricated as well as measured. In a final step, the complex task of fabricating the entire device was successfully completed.

The electrical, optical and thermal properties of the device have been investigated via FEM and FDTD tools to base the device operation on solid research. It was found that the resistance for the improved contact design is around 1000 Ω and the current densities in the active region can be on the order of 100 - 200 A/cm^2, which is sufficient to pump the quantum-dots. Optical losses as well as the gain were estimated, showing that lasing is possible for 3 layers QDs and a minimum Q-factor of 5000. Five layers of QDs, on the other hand, can reach lasing with even lower Q-factors than 5000. The simulations concerning the thermal behaviour suggest that the ideal device, with a threshold current density of 10's of A/cm^2, can operate in the membrane configuration where the increase in temperature is only a few Kelvin's. Due to the exponential increase of the temperature with the current density, the membrane configuration can reach up to 90 K above RT when 335 A/cm^2 are present at the centre of the PhC cavity. The heat sinking through the oxide layer lowers this temperature by a factor 4 and is therefore preferable.

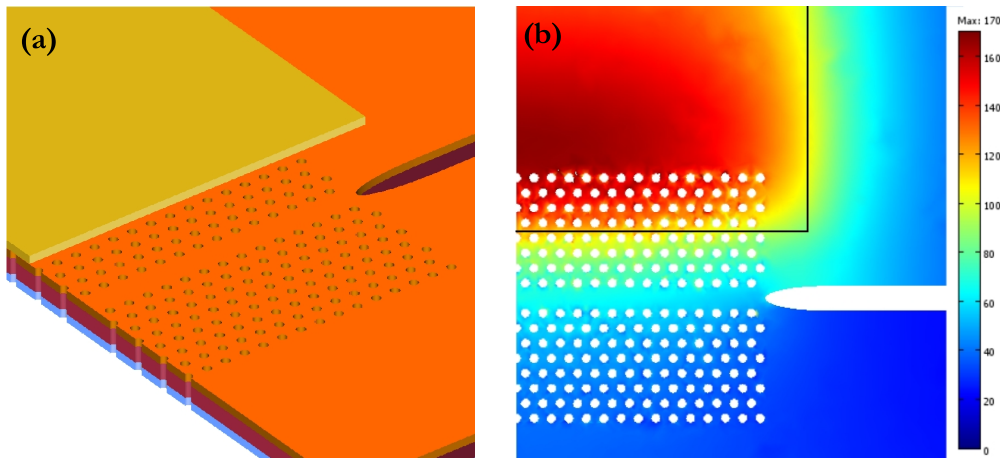

Figure 7.1 Design of the device with the metal-contact on top of the PhC (a). Current density distribution [A/cm²] of the design simulated using FEM (b). The box indicates the position of the p-contact.

A new line-defect cavity design was developed, based on non-arbitrary modifications of the PhC to confine the Gaussian mode distribution. The cavities were first fabricated in Silicon and achieved a maximum experimental Q-factor of ~ 600.000, which is believed to be only limited by fabrication imperfections.

I designed the wafers and tested them for electrical diode behaviour as well as for modal gain with stripe-waveguide devices. The electrical properties were in the region of 1000 to 2000 Ω and close to the predictions, but the gain measurements were lower than expected. For the first wafer (Vn1315), a maximum modal gain for the whole structure of 5 cm^{-1} was measured while for the second wafer (Vn1807) it was slightly higher with 7 cm^{-1}. It is thought that these values do not represent the actual values, but they are caused by misguiding effects in the waveguide and pump depletion. I also developed a PhC etch with a titanium-oxide hard-mask and a unique hard-mask removal technique that allows us to use the cavity on oxidised AlGaAs. The fabricated membrane and oxide cavities were measured on a micro-photoluminescence test-bed that I set up. Maximum Q-factors reach about 4000 for the membrane and a remarkable 2200 for the oxide cavity, which is mostly due to the hard-mask removal technique. Higher Q-factors are possible by reducing the hole-diameter down to about 100 nm as it was observed during the measurements.

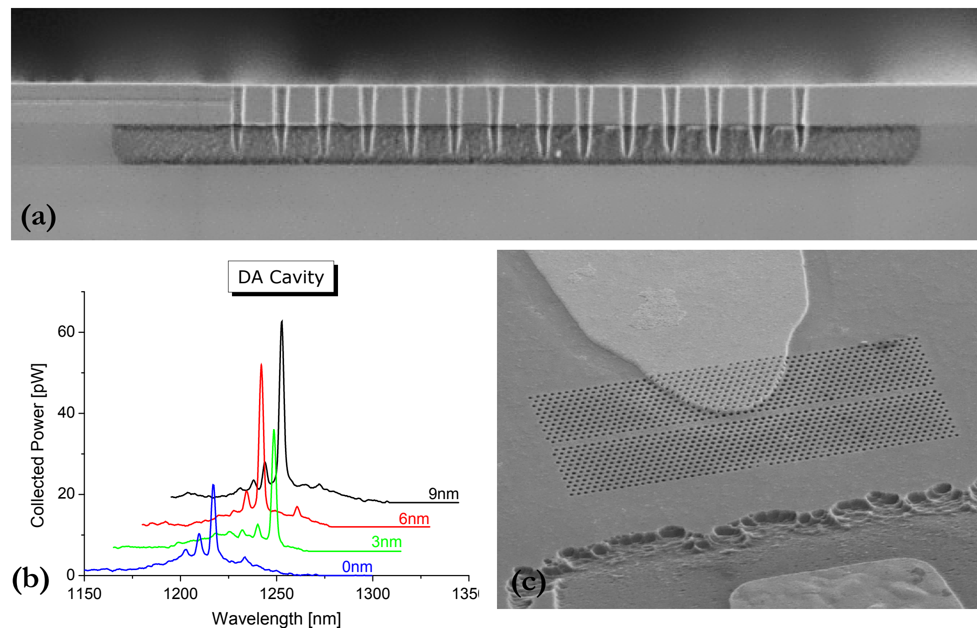

Figure 7.2 Selection of obtained results. Cross-section through oxide cavity (a), uPL measurements for far-field optimised DA cavity on oxide (b) and fabricated final device (c).

The individual fabrication steps, necessary for the full device, were combined and it was shown that the final device can be fabricated in accordance to our design specifications.

Dividing the properties of the device into optical, electrical and thermal tasks proved to be an efficient way to estimate its overall performance. Moreover, some interesting points arose from this investigation which I would to like emphasise in the following. Placing the metal-contact on top of the PhC cavity is beneficial because it increases of current density inside the cavity and even improves the heat dissipation out of the cavity due to the highly conductive metal-contact. It is even possible to place the metal-contact very close (500 nm…750 nm) to the centre of the cavity while still maintaining Q-factors of a few 1000's. The fabrication of this arrangement was possible, although no measurements were performed to investigate its real-life behaviour. There is a very interesting outcome from the simulations and measurements concerning the hole-diameter of the PhC cavity. As it turns out, not only the electrical and thermal, but also the optical performance improves when smaller holes are used, but only for a gentle confinement cavity. One should therefore strive for small holes, as far the fabrication method allows. The

simulations performed on the thermal properties revealed that a membrane configuration is indeed capable of handling the heat generated heat inside the cavity. However the current density has to be low, in the order of 10's of A/cm^2, which requires a highly efficient carrier injection into the cavity. From this point of view the oxide is not even needed, but it seems that the Q-factor does not suffer too much in presence of the oxide. This, however, depends strongly on the fabrication, which turned out to be more difficult than expected. An alternative design will be presented in 7.1 "Future Work".

During this project, I gained deeper understanding of opto-electronic devices, not only by reading about them, but also by simulating, fabricating and characterising them. Novel cavity designs emerged from this project as well as unique fabrication methods such as the hard-mask removal, which might find other purposes as well. I still believe that the electrically pumped photonic-crystal laser (ePCL) presented here is feasible, however modifications can be made to improve performance and simplify the fabrication, as shown next.

7.1 Future Work

Looking at the current injection, there is room for improvement in order to achieve higher densities and less leaky currents. It was shown that moving the contact closer to the cavity increases the current density but also introduces a high amount of loss. Therefore, it should be investigated whether a transparent conductive oxide (TCO) can be placed on top of the cavity in order to concentrate all current flow through the centre of the cavity. The losses of the TCO should also be investigated and the performance analysed through simulations, but the TCO approach is promising.
The oxide below the cavity is in my opinion a must when practical and reliable devices are concerned. Oxidised AlGaAs, however, turned out to be more difficult to form and to work with. A back-infiltration with flowable oxide (FOx) can prove an easy alternative providing a heat sink and a mechanical support. A modification of the newly developed back-infiltration method can help with the removal of FOx

from the top-surface in order to allow electrical contacts. Moreover, using the FOx layer stabilises the sulphide passivation and strongly improves the device's lifespan. The fabricated electrical contacts to the GaAs seemed to have high specific contact-resistance. Therefore, it is useful to investigate and further optimise the evaporation process, because small devices have a higher contact resistance than larger ones. Improvement on the PhC cavities can also be made. This addresses less the types of cavities but more their fabrication. The CAIBE is a good tool to create high-aspect ratio holes, but it is less mature than i.e. the RIE. A passivation feature, which is standard in the RIE, is missing in our CABIE process. Further development on this side should highly improve the hole-quality and the Q-factors.
With the fabrication process working well, the device should be further optimised using the here described simulation tools. With their help, the current flow can be even more directed, leading to higher efficiencies. Finally, regarding ultra-low threshold, this can be achieved by finely balancing the optical losses and the gain so that in future the ePCL might even operate with only one layer of QDs and threshold of only a few nanoamperes.

There is still a need for practical mirco-emitters and the work presented here is a step towards making this a realistic possibility.

Appendix A

Fabrication Details

Device: Electrically Pumped Stripe-laser

Waveguide wet-etch

- Clean the cleaved sample in acetone and IPA using low lower ultra-sonic bath
- Spin S1805 at 7000 rpm and bake for 2 min at 100 ºC on hot-plate
- Expose for 10 s on old mask-aligner (mask: 1803 Brown 2)
- Develop for 20 s in MF-319
- Hard-bake for 10 min at 100ºC on hot-plate
- Wet-etch in H_3PO_4 :H_2O_2 : DI (3ml:1ml:30ml) using multiple steps (etch-rate ~ 100 nm/min) and verify with profilometer, stop on n-GaAs
- Remove resist in 1165

Lift-off n-contact

- Spin LOR at 4000 rpm and bake for 5 min at 180ºC on hot-plate
- Spin S1805 at 5000 rpm and bake for 2 min at 100ºC on hot-plate
- Expose for 10 s on old mask-aligner (mask: 1803 Brown 2)
- Develop for > 20 s in MF-319
- Glue sample on cover-slip with PMMA
- Native oxide removal in 30% NH_4OH for 30 s
- Immediate load into electron-beam evaporator
- Evaporate: 14 nm Au, 14nm Ge, 14 nm Au, 11nm Ni, 100nm Au
- For lift-off: 30 min soak in 65 ºC 1165, then ultra-sonic a low power
- Annealing for 1 min at 450 ºC

Lift-off p-contact

- Spin LOR at 4000 rpm and bake for 5 min at 180ºC on hot-plate
- Spin S1805 at 5000 rpm and bake for 2 min at 100ºC on hot-plate
- Edge-bead removal at high-intensities
- Expose for 10 s on old mask-aligner (mask: 1803 Brown 2)
- Develop for > 20 s in MF-319
- Glue sample on cover-slip with PMMA
- Native oxide removal in 30% NH_4OH for 30 s
- Immediate load into electron-beam evaporator
- Evaporate: 20 nm Ni, 100 nm Au
- For lift-off: 30 min soak in 65 ºC 1165, then ultra-sonic a low power

- Cleave sample to desired length

Device: Optically Pumped Stripe-laser

Waveguide wet-etch

- Clean the cleaved sample in acetone and IPA using low lower ultra-sonic bath
- Spin S1805 at 7000 rpm and bake for 2 min at 100ºC on hot-plate
- Expose for 10 s on old mask-aligner (mask: 1803 Brown 2)
- Develop for 20 s in MF-319
- Hard-bake for 10 min at 100ºC on hot-plate
- Wet-etch in H_3PO_4 :H_2O_2 : DI (3ml:1ml:30ml) using multiple steps (etch-rate ~ 100 nm/min) and verify with profilometer, stop on n-GaAs
- Remove resist in 1165

Prepare for wet-oxidation

- Clean the cleaved sample in acetone and IPA using low lower ultra-sonic bath
- Spin S1818 at 5000 rpm and bake for 2 min at 100ºC on hot-plate

- Expose for 30 s on old mask-aligner (mask: 1803 Brown 2)
- Develop for 45 s in MF-319
- CAIBE etch: 5 min, 100ºC, 10 mA, 1000 V, 50 sccm Ar, 50 sccm Cl_2,
- Remove resist in 1165

Wet-oxidation

- Native oxide removal in 30% NH_4OH for 30 s
- Immediate load into oxidation-chamber
- 45 min wet-oxidation, 450ºC sample temperature, 80ºC water bubbler temperature, 400 sccm N_2 flow

- Cleave sample to desired length

ePCL

Photonic-crystal Cavity

- Clean the cleaved sample in acetone and IPA using low lower ultra-sonic bath
- Load in electron-beam evaporator and deposit 120 nm TiO_x
- Spin ZEP-520A at 3750 rpm and bake for 10 min at 180ºC on hot-plate
- Expose with e-beam writer desired PhC pattern with 45 $\mu C/cm^2$ base dose
- Develop for 45 s in Xylene at 23ºC
- Dry-etch of TiO_x in RIE: 10 sccm SF_6, 10 sccm CHF_3, 2.5^10^{-2} mbar pressure, 20 W for 120 s
- Remove resist in 1165 for 1h at 60 ºC
- Dry-etch of GaAs in CAIBE: 20 sccm Ar and 18 sccm Cl_2, 4.2^10^{-4} mbar pressure, 500 V, 6 mA, 80 ºC, 12 min

Hard-mask removal

- Native oxide removal in 30% NH_4OH for 30 s

- Drop S1805 onto sample, place sample in desiccator for 3 min and spin sample at 5000 rpm
- Bake for 2 min at 100°C on hot-plate
- Expose with UV lamp for ~ 120 s (multiple steps)
- Develop for 45 s in MF-319
- Hard-bake for 30 min at 90°C on hot-plate
- Remove TiO_x in buffered HF (1:6, hydrofluoric-acid : ammonium-fluoride) for 10 min
- Remove resist in 1165 for 1h at 60 °C

- For membrane cavity: wet-etch of AlGaAs in hydrochloric-acid:DI water (1:1, HCl : H_2O)for 70 s

Wet-oxidation

- Native oxide removal in 30% NH_4OH for 30 s
- Immediate load into oxidation-chamber
- 20 min wet-oxidation, 450°C sample temperature, 80°C water bubbler temperature, 300 sccm N_2 flow

Wet-etch to n-contact

- Spin S1805 at 7000 rpm and bake for 2 min at 100°C on hot-plate
- Expose for 10 s on old mask-aligner (mask: ePCL wet-etch)
- Develop for 20 s in MF-319
- Hard-bake for 10 min at 100°C on hot-plate
- Wet-etch in H_3PO_4 :H_2O_2 : DI (3ml:1ml:30ml) using multiple steps (etch-rate ~ 100 nm/min) and verify with profilometer, stop on n-GaAs
- Remove resist in 1165

Lift-off n-contact

- Spin LOR at 4000 rpm and bake for 5 min at 180°C on hot-plate

- Spin S1805 at 5000 rpm and bake for 2 min at 100ºC on hot-plate
- Edge-bead removal at high-intensities
- Expose for 15 s on old mask-aligner (mask: ePCL n-contact)
- Develop for > 20 s in MF-319
- Glue sample on cover-slip with PMMA
- Native oxide removal in 30% NH_4OH for 30 s
- Immediate load into electron-beam evaporator
- Evaporate: 14 nm Au, 14nm Ge, 14 nm Au, 11 nm Ni, 100 nm Au
- For lift-off: 30 min soak in 65 ºC 1165, then ultra-sonic a low power
- Annealing for 1 min at 450ºC

Lift-off p-contact

- Spin LOR at 4000 rpm and bake for 5 min at 180ºC on hot-plate
- Spin S1805 at 5000 rpm and bake for 2 min at 100ºC on hot-plate
- Edge-bead removal at high-intensities
- Expose for 2 s on new mask-aligner (mask: ePCL p-contact)
- Develop for > 20 s in MF-319
- Glue sample on cover-slip with PMMA
- Native oxide removal in 30% NH_4OH for 30 s
- Immediate load into electron-beam evaporator
- Evaporate: 20nm Ni, 100 nm Au
- For lift-off: 30 min soak in 65 ºC 1165, then ultra-sonic a low power

Appendix B

Further Analysis on the Threshold Formulation

In section 3.3.2.3 "Necessary Material Gain for Lasing" we used the general formula (Eq.3.14) in order to describe the gain:

$$\frac{2\pi n_{eff}}{\lambda}\frac{1}{Q} = g_g \Gamma_g \qquad \text{(Eq.B.1)}$$

where no internal losses are present and the main photon loss is represented by Q. In stripe-laser, a different formulation is used considering the reflectivities of the factes [Coldren95]:

$$\frac{1}{L}\ln\left(\frac{1}{R}\right) = g_g \Gamma_g \qquad \text{(Eq.B.2)}$$

where L is the length of the resonator and R being its reflectivity. R can also be written in terms of Q-factor:

$$Q = \frac{m\pi}{R-1} \rightarrow \frac{1}{L}\ln\left(\frac{1}{(1-\frac{m\pi}{Q})}\right) = g_g \Gamma_g \qquad \text{(Eq.B.3)}$$

with m as the mode number. The mode number is usually defined by the means of how many half-wavelengths fit inside the resonator with an optical path length of $L*n_{eff}$.

We can calculate the right-hand side of Eq.B1, which is for the general case, and compare it for the formulation for stripe-lasers in Eq.B.3.

General Case

Let n_{eff} be 3.2, $\lambda = 1200\ nm$ and $Q = 10000$ so that Eq.B.1 results in $1.68 \times 10^{-3}\ cm^{-1}$.

Stripe-laser Case

Using an effective cavity length $L = 2000\ nm$, determined by the 1/e decay of the mode within the PhC cavity we obtain a mode number of $m = 10$. The right-hand side of Eq.B.3 then result in $1.57 \times 10^{-3}\ cm^{-1}$.

We conclude that both cases give similar results so that the stripe-laser formulation can also be used with PhC cavities, however, with a larger error when the cavity length is in similar to the value of the wavelength.

Bibliography

Akahane03 Akahane, Y; Asano, T; Song, B-S *et al.*; "High-Q photonic nanocavity in a two-dimensional photonic crystal"; Nature, Vol. 425, 944-947; (2003)

Almuneau11 Almuneau, G; Conde, M; Gauthier-Lafaye, O *et al.*; "High reflectivity monolithic sub-wavelength diffraction grating with GaAs/AlOx stack"; Journal of Optics, Vol. 13, 012205; (2011)

Altug06 Altug, H; Englund, D; Vuckovic, J; "Ultrafast photonic crystal nanocavity laser"; Nature Physics, Vol. 2, 484; (2006)

Asano06 Asano, T; Song, B-S; Akahane, Y *et al.*; "Ultrahigh-Q Nanocavities in Two-Dimensional Photonic Crystal Slabs"; Journal of Selected Topis in Quantum Electronics, Vol. 12; (2006)

Asghar06 Asghar, M.H; Placido, F; Naseem, S *et al.*; "Characterization of reactively evaporated TiO2 thin films as high and medium index layers for optical applications"; The European Physical Journal Applied Physics, Vol. 35, 177; (2006)

Avary02 Avary, K; Reithmaier, J.P, Klopf, F *et al.*; "Deeply etched two-dimensional photonic crystals fabricated on GaAs/AlGaAs slab waveguides by using chemically assisted ion beam etching"; Microelectronic Engineering, Vol. 61, 875; (2002)

Baca05 Baca, A.G; Ashby, C.I.H; "Fabrication of GaAs Devices"; The Institution of Electrical Engineers, London; (2005)

Baek05 Baek, I-B; Yang, J-H; Cho, W-J *et al.*; "Electron beam lithography patterning of sub-10 nm line using hydrogen silsesquioxane for nanoscale device applications"; Journal of Vacuum Science & Technology B, Vol. 23, 3120; (2005)

Berrier07 Berrier, A; Mulot, M; Malm, G *et al.*; "Carrier Transport Through a dry-etched InP-based two-dimensional photonic crystal"; Journal of Applied Physics, Vol. 101, 123101-1; (2008)

Bessolov97 Bessolov, V.N; Lebedev, M.V; Zahn, D.R.T *et al.*; "Raman scattering study of surface barriers in GaAs passivated in alcoholic sulphide

solutions"; Journal of Applied Physics, Vol. 82, 2640; (1997)

Brozel96 Brozel, M.R; Stillman, G.E; "Properties of Gallium Arsenide"; Institution of Engineering and Technology; (1996)

Choi05 Choi, Y.S; Kim, S.K; Kim, S.H *et al.*; "Lithographic tuning of photonic-crystal unit-cell resonators with InGaAs/GaAs quantum dots emitting at 1.2 mm"; Journal of Vacuum Science & Technology B, Vol. 23, 252; (2005)

Cardile11 Cardile, P; Franzo, G; Lo Savio, R *et al.*; "Electrical conduction and optical properties of doped silicon-on-insulator photonic crystals"; Applied Physics Letter, Vol, 98, 203506; (2011)

Chakravarty07 Chakravarty, S; Bhattacharya, P; Topolancik, J. *et al.* "Electrically injected quantum dot photonic crystal microcavity light emitters and microcavity arrays"; Journal Physics D: Applied Physics, Vol. 40, 2690; (2007)

Chung00 Chung, C. W; Chung, I; "Platinum etching using a TiO2 hard mask in an O2/Cl2/Ar plasma"; Journal of Vacuum Science & Technology A, Vol. 18, 835; (2000)

Coldren95 Coldren, L; Corzine, S; "Diode Lasers and Photonic Integrated Circuits"; John Wiley & Sons Inc, New York; (1995)

Collot90 Collot, P; Gaonach, C; "Electrical damage in n-GaAs due to methane-hydrogen RIE"; Semiconductor Science and Technology, Vol. 5, 237; (1990)

Daleiden99 Daleiden, J; Kiefer, R; Klussmann, S *et al.*; "Chemically-assisted ion-beam etching of (AlGa)As/GaAs: lattice damage and removal by in-situ Cl_2 treatment"; Microelectronic Engineering, Vol. 45, 9; (1999)

Dienelt01 Dienelt, J; Zimmer, K; Rauschenbach, B *et al.*; "Etching behaviour of GaAs with chlorine chemically assisted ion beam etching depending on the surface temperature"; Conference Paper, Gaas 2001; London.

Einstein17 Einstin, A; "On the Quantum Theory of Radiation"; Physikalische Zeitschrift, Vol. 18, 121; (1917)

Ellis11 Ellis, B; Mayer, M.A; Shambat, G *et al.*; "Ultralow-threshold electrically pumped quantum-dot photonic-crystal nanocavity laser"; Nature Photonics, Vol. 24, 297; (2011)

[4]Reprinted by permission from Macmillan Publishers Ltd: [Nature

Photonics] (doi:10.1038/nphoton.2011.51), copyright (2011)

Englund07 Englund, D; Altug, H; Vuckovic, J *et al.*; " Low-threshold surface-passivated photonic crystal nanocavity laser"; Applied Phyics Letters, Vol. 91, 071124; (2007)

Errico07 Errico, V; Stomeo, T; Salhi, A. *et al.* "Quantum dot nano-cavity emission tuned by a circular photonic crystal lattice"; Microelectronic Engineering, Vol. 84, 1570; (2007)

Francardi09 Francardi, M; Gerardino, A; Balet, L *et al.*; "Cavity-enhanced photonic crystal light-emitting diode at 1300 nm"; Microelectronic Engineering, Vol. 86, 1093; (2009)

[3] Reprinted with permission from Elsevier.

Fujita08 Fujita, M; Tanaka, Y; Noda, S *et al.*; "Light Emission From Silicon in Photonic Crystal Nanocavity"; IEEE Journal of selected Topics in Quantum Electronics, Vol. 14, 1090; (2008)

Galli09 Galli, M; Portalupi, S.L; Belotti, M *et al.*; "Light scattering and Fano resonances in high-Q photonic crystal nanocavities"; Applied Physics Letters, Vol. 94, 071101; (2009)

[8] Reprinted with permission. Copyright 2009, American Institute of Physics.

Geib97 Geib, K.M; Choquette, K.D; Hou, H.Q *et al.*; "Fabrication issues of oxide-confined VCSELs"; SPIE, Vol. 3003, 69; (1997)

Giannopoulos10 Giannopoulos, A.V; Long, C.M; Choquette, K.D *et al.*; "Decimated Photonic Crystal Membrane Defect Cavity Lasers"; IEEE International Semiconductor Laser Conference, 22, 187; (2010)

Grine07 Grine, Alejandro; "The Design and Fabrication of an Electrically Activated Photonic Crystal Microcavity Laser"; Thesis submitted for Master of Science in Electrical Engineering; Massachusetts Institute of Technology; (2007)

Guha96 Guha, S; Agahi, F; Pezeshki, B *et al.*; "Microstructure of AlGaAs-oxide heterolayers formed by wet oxidation"; Applied Physics Letters, Vol. 68, 906; (1996)

Hakki75 Hakki, B. W; Paoli, T. L; "Gain spectra in GaAs double-heterstructure injection lasers"; Journal of Applied Physics, Vol. 46, 1299; (1975)

Hall62 Hall, R.N; Fenner, G.E; Kingsley, J.D *et al.*; "Coherent Light Emission

from GaAs Junctions"; Physical Review Letter, Vol. 9, 366; (1962)

Holonyak87 Holonyak, N; "Semiconductor Alloy Lasers - 1962"; IEEE Journal of Quantum Electronics, Vol. 23, 684; (1987)

Ikeda07 Ikeda, N; Sugimoto, Y; Watanabe, Y *et al.*; "Precise control of dry etching for nanometer scale air-hole arrays in two-dimensional GaAs/AlGaAs photonic crystal slabs"; Optics Communications, Vol. 275, 257; (2007)

Jiang00 Jiang, W.H; Xu, H.Z; Xu, B *et al.*; "Annealing effect on the surface morphology and photoluminescence of InGaAs/GaAs quantum dots grown by molecular beam epitaxy"; Journal of Crystal Growth, Vol. 212, 356; (2000)

Kim96 Kim, J-H; Lim, D. H; Kim, K. S *et al.*; "Lateral wet oxidation of $Al_xGa_{1-x}As$-GaAs depending on its structure"; Applied Physics Letters, Vol. 69, 3357; (1996)

Ku03 Ku, P-C; Chang-Hasnain, C.J; "Thermal Oxidation of AlGaAs: Modeling and Process Control"; IEEE Journal of Quantum Electronics, Vol. 39, 577; (2003)

Kuramochi06 Kuramochi, E; Notomi, M; Mitsugi, S *et al.*; "Ultrahigh-Q photonic crystal nanocavities realized by the local width modulation of a line defect"; Applied Physics Letters, Vol. 88, 041112; (2006)

[7]Reprinted with permission. Copyright 2006, American Institute of Physics.

Kwon08 Kwon, S-H; Suenner, T; Kamp, M *et al.*; "Ultrahigh-Q photonic crystal cavity created by modulating air hole radius of a waveguide"; Optics Express, Vol. 16, 4605-4614; (2008)

[6] With permission of Optical Society of America

Li07 Li, C.Y; Yoon, S.F; Cao, Q *et al.*; "Low transparency current density and high temperature operation from ten-layer p-doped 1.3 um InAs/InGaAs/ GaAs quantum dot lasers"; Applied Physics Letters, Vol. 90, 041103; (2007)

Ledenstov00 Ledenstov, N.N; Grundmann, M; Heinrichsdorff, F *et al.*; "Quantum-Dot Heterostructure Lasers"; IEEE Journal of Selected Topics in Quantum Electronics, Vol. 6, 439, (2000)

LeDu06 LeDu, M; Massoubre, D; Harman, J-C *et al.*; "Thermal conductance of

laterally-wet-oxidised GaAs/Al_xO_y Bragg reflectors"; Electronic Letters, Vol. 42, 192; (2006)

Liu09 Liu, N; Ruseckas, A; Montgomery, N.A *et al.*; "Semiconducting polymer waveguides for end-fired ultra-fast optical amplifiers"; Optics Express, Vol. 17, 21452; (2009)

Loncar04 Loncar, M; Yoshie, T; Okamoto, K; *et al.* "Planar Photonic Crystal Nanolaser(I): Porous Cavity Laser"; IEICE Trans Electron, Vol. 87, 291; (2004)

Long09 Long, C.M; Giannopoulos, A.V; Choquette, K.D *et al.*; "Modified Spontaneous Emission from a Laterally Injected Photonic Crystal Emitter"; Electronics Letters, Vol. 45, 227; (2009)

Lu08 Lu, T-W; Lee, P-T; Tseng, C-C *et al.*; "Modal properties and thermal behaviors of high quality factor quasi-photonic crystal microcavity"; Optics Express, Vol. 16, 12591; (2008)

Mao11 Mao, M-H; Chien, H-C; Hong, J-Z *et al.*; "Room-temperature low-threshold current-injection InGaAs quantum-dot microdisk lasers with single-mode emission"; Optics Express, Vol. 19, 14145; (2011)

Marko05 Marko, P; Adams, A.R; Sweeney, S.J *et al.*; "Recombination and Loss Mechanisms in Low-Threshold InAs–GaAs 1.3-μm Quantum-Dot Lasers"; IEEE Journal on Selected Topic in Quantum Electronic, Vol. 11, 1041; (2005)

Marko05b Marko, P; Masse, N; Sweeney, S.J *et al.*; "Effect of gain saturation and nonradiative recombination on the thermal characteristics of InAs/GaAs 1.3 μm quantum dot lasers"; 18th LEOS, Piscataway, USA; (2005)

Mock10 Mock, Adam; "First principles derivation of microcavity semiconductor laser threshold condition and its application to FDTD active cavity modelling"; Journal of the Optical Society of America B, Vol. 27, 2262; (2010)

Moore06 Moore, S.A; O'Faolain, L; Cataluna, M. A *et al.*.; "Reduced Surface Sidewall Recombination and Diffusion in Quantum-Dot Lasers"; IEEE Photonics Technology Letters, Vol. 18, 1861; (2006)

Moore08 Moore, S.A; "Photonic crystals as functional mirrors for semiconductor lasers"; PhD Thesis, University of St Andrews, St Andrews, Scotland;

(2008)

MPB01 Johnson, S.G; Joannopoulos, J.D; “Block-iterative frequency-domain methods for Maxwell’s equations in a planewave basis”; Optics Express, Vol. 8, 173; (2001)

Mori78 Mori, Y; Watanabe, N; “A New Etching Solution System, Phosphoric Acid-Hydrogen Peroxide-Water, for GaAs and Its Kinetics”; Journal of the Electrochemical Society, Vol. 125, 1510; (1978)

Nomura06 Nomura, M; Iwamoto, S; Watanabe, K *et al.*; “Room temperature continuous-wave lasing in photonic crystal nanocavity”; Optics Express, Vol. 14, 6308; (2006)

Nomura09 Nomura, M; Kumagai, N; Iwamoto, S. *et al.* ” Photonic crystal nanocavity laser with a single quantum dot gain”; Optics Express, Vol. 17, 15975; (2009)

Nomura10 Nomura, M; Ota, Y; Kumagai, Naoto *et al.*; “Zero-cell photonic crystal nanocavity laser with quantum dot gain”; Applied Physics Letter, Vol. 97, 19110; (2010)

Norasetthekul01 Norasetthekul, A; Park, P.Y; Baik, K.H *et al.*; “dry etch chemistries for TiO_2 thin films”; Applied Surface Science, Vol. 185, 27; (2001)

Nozaki05 Nozaki, K; Baba, T; “Carrier and Photon Analyses of Photonic Microlasers by Two-Dimensional Rate-Equations ”; IEEE Journal on Selected Areas in Communication, Vol. 23, 1411; (2005)

Nozaki07 Nozaki, K; Kita, S; Baba, T; “Room temperature continuous wave operation and controlled spontaneous emission in ultrasmall photonic crystal nanolaser”; Optics Express, Vol. 15, 7506; (2007)

O’Brien07 O’Brien, J; Kuang, W; Cao, J-R; *et al.* “Photonic crystal microcavity lasers”; Journal of Physics D: Applied Physics, Vol. 40, 2671; (2007)

O’Faolain06 O’Faolain, L; Kotlyar, M.V; Tripathi, N *et al.*; “Fabrication of photonic crystals using a spin-coated hydrogen silsesquioxane hard mask”; Journal of Vacuum Science & Technology B, Vol. 24, 335; (2006)

Ohno91 Ohno, T; “Sulfur passivation of GaAs surfaces”; Physical Review B, Vol. 44, 6306; (1991)

Painter99 Painter, O; Lee, R-K; Scherer, A; *et al.* “Two-Dimensional Photonic Band-Gap Defect Mode Laser”; Science, Vol. 284, 1819; (1999)

[1] Reprinted with permission from AAAS

Park04 Park, H-G; Kim, S-H; Kwon, S-H, *et al.* "Electrically Driven Single-Cell Photonic Crystal Laser"; Science, Vol. 305, 1444; (2004)

[2] Reprinted with permission from AAAS

Portalupi10 Portalupi, S.L; Galli, M; Reardon, C *et al.*; "Planar photonic crystal cavities with far-field optimization for high coupling efficiency and quality factor"; Optics Express, Vol. 18, 16064; (2010)

Rattier02 Rattier, M; Benisty, H; Stanley, R.P *et al.*; "Toward Ultrahigh-Efficiency Aluminum Oxide Microcavity Light-Emitting Diodes: Guided Mode Extraction by Photonic Crystals"; IEEE Journal on Selected Topic in Quantum Electronic, Vol. 8, 238; (2002)

Ravaro07 Ravaro, M; Le Du, M; Likforman, J.-P *et al.*; "Estimation of parametric gain in GaAs/AlOx waveguides by fluorescence and second harmonic generation measurements"; Applied Physics Letter, Vol. 91, 191110; (2007)

Sandroff89 Sandroff. C.J; Hegde. M.S; Farrow, L.A *et al.*; "Electronic passivation of GaAs surfaces through the formation of arsenic sulphur bonds"; Applied Physics Letters, Vol. 54, 362; (1989)

Rostami11 Rostami, A; Baghban, H; Maram, R *et al.*; "Nanostructure Semiconductor Optical Amplifiers: Building Blocks for All-Optical Processing"; Springer-Verlag, Berlin; (2011)

Schubert07 Schubert, F; "Light-Emitting Diodes"; Cambridge University Press, Cambridge, 2nd Edition; (2008)

Sellin01 Sellin, R.L; Ribbat, Ch; Grundmann, M *et al.*; "Close-to-ideal device characteristics of high-power InGaAs/GaAs quantum dot lasers"; Applied Physics Letters, Vol. 78, 1207; (2001)

Shi04 Shi, G.X; Jin, P; Xu, B *et al.*; "Thermal annealing effect on InAs/InGaAs quantum dots grown by atomic layer molecular beam epitaxy"; Journal of Crystal Growth, Vol. 269, 181; (2004)

Seo07 Seo, M-K; Jeong, K-Y; Yang, J-K; *et al.* "Low threshold current single-cell hexapole mode photonic crystal laser"; Applied Physics Letters, Vol. 90, 171122; (2007)

Smowton04 Smowton, P.M; Pearce, E.J; Lutti, J *et al.*; "Novel in-plane semiconductor lasers III"; Proceedings Society Photo-Optical Instrumentation Engineers, Vol. 5365, 86; (2004)

Song05 Song, B-S; Noda, S; Asano, T *et al.*; "Ultra-high-Q photonic double-heterostructure nanocavity"; Nature Materials Vol. 4, 207-210; (2005)

Song11 Song, B-S; Jeon, S-W; Noda, S *et al.*; "Symmetrically glass-clad photonic crystal nanocavities with ultrahigh quality factors"; Optics Letters, Vol. 36, 91-93; (2011)

Spitzer59 Spitzer, W.G; Whelan, J.M; "Infrared Absorption and Electron Effective Mass in n-Type Gallium Arsenide"; Physical Review Letters, Vol. 114, 59; (1959)

Stranski38 Stranski, I. N; Krastanow, L; "Abhandlungen der Mathematisch-Naturwissenschaftlichen Klasse IIb"; Akademie der Wissenschaften Wien, 146, 797; (1938)

Ryu02 Ryu, H-Y; Park, H-G; Lee, Y-H; "Two-Dimensional Photonic Crystal Semiconductor Lasers: Computational Design, Fabrication, and Characterization"; IEEE Journal of Selected Topics in Quantum Electronics, Vol. 8, 891; (2002)

Takahasi07 Takahashi, Y; Hagino, H; Tanaka, Y *et al.*; "High-Q nanocavity with a 2-ns photon lifetime"; Optics Express, Vol. 15, 17206-17213; (2007)

Tanaka08 Tanaka, Y; Asano, T; Noda, S *et al.*; "Design Photonic Crystal Nanocavity with Q factor of one billion"; Journal of Technology, Vol. 26, 1532-1539; (2008)
[5] Copyright © 2008, IEEE

Tawara08 Tawara, T; Kamada, H; Zhang, Y-H *et al.*; "Quality factor control and lasing characteristics of InAs/InGaAs quantum dots embedded in photonic-crystal nanocavities"; Optics Express, Vol.16, 5199; (2008)

Tran10 Tran, N-V-Q; Combrie, S; Colman, P *et al.*; "Vertical high emission in photonic crystal nanocavities by band-folding design"; Physical Review B, Vol. 82, 075120; (2010)
[9]Reprinted with permission. Copyright (2010) by the American Physical Society
http://prb.aps.org/abstract/PRB/v82/i7/e075120

Twesten96 Twesten, R. D; Follstaedt, D. M; Choquette, K. D *et al.*; "Microstructure of laterally oxidized AlxGa12xAs layers in vertical-cavity lasers"; Applied Physics Letters, Vol. 69, 19; (1996)

Ustinov07 Ustinov, V.M; Zhukov A.E; Egorov, A,Y *et al.*; "Quantum Dots

Lasers"; Oxford Science Publication, Oxford, (2007)

Verlangieri91 Verlangieri, P.A; Kuznetsov, M; Schneider, M.V *et al.*; "Low-Resistance Ohmic Contacts for Microwave and Lightwave Devices"; IEEE Microwave and Guided Wave Letters, Vol. 1, 1051; (1991)

Yoon00 Yoon, S.F; Ng, T.K; Zheng, H.Q *et al.*; "Optimization of GaAs ECR etching in chemically assisted ion beam process using Cl2/Ar plasma"; Materials Science in Semiconductor Processing, Vol. 3, 207; (2000)

Yoshie04 Yoshie, T; "Planar Photonic Crystal Nanocavities with Active Quantum Nanostructures"; PhD Thesis, California Institute of Technology, Pasadena, California; (2004)

Yu99 Yu, Y.P; Cardona, M; "Fundamentals of Semiconductors: Physics and Material Properties"; Springer-Verlag, Berlin, 2nd edition; (1999)